Sixth DELTA
User- meeting

Dortmund
25. November 2010

Dear reader,

The last Wednesday of November is DELTA User-Meeting's day. It is since 2005 and we will continue this tradition in the next years.

A first enlargement of the building is finished, a new beamline is under construction and classes, lectures and education around the machine are available at the 'Chair of Accelerator Physics' (Prof. S. Khan) at TU-Dortmund. This offers a quite promising education for the students of the TU-Dortmund and of the 'NRW Forschungsschule – *Forschung mit Synchrotronstrahlung*' (Prof. M. Tolan). First results of their research are included in this annual report.

The results presented in this report could only be obtained by big efforts, hard work, and services provided to maintain or even improve the performance and the operation of DELTA. Thanks to the crew.

Alex von Bohlen

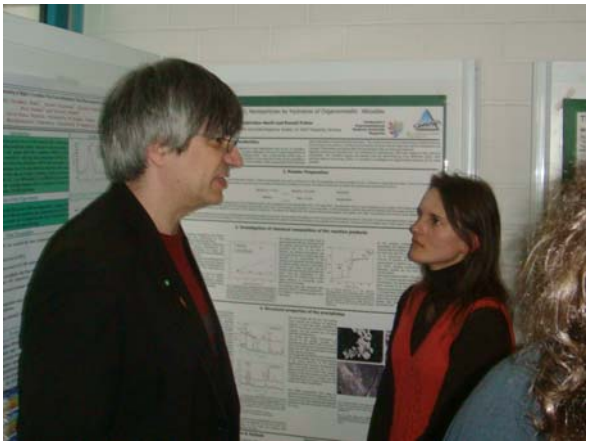


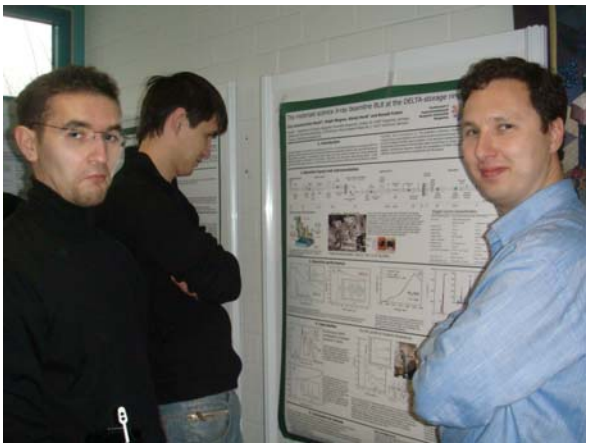
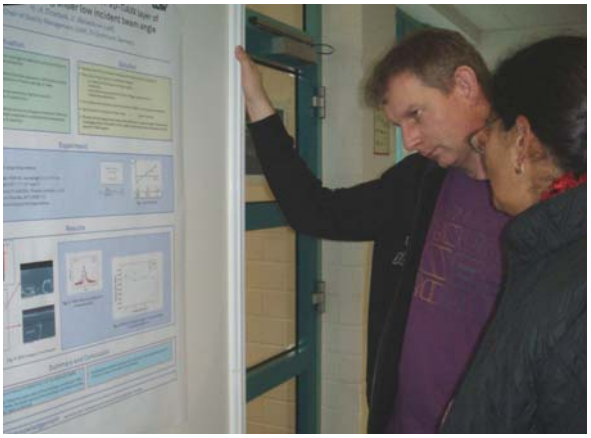


Some impressions from the DELTA User-Meeting
captured during the Poster Session 2009.

Beamline overview:

BL 0 not in use
- Technische Universität Dortmund
- White beam at DELTA bending magnet, critical energy 2.2 keV
- Infrared

BL 1
- Technische Universität Dortmund
- White beam at DELTA bending magnet, critical energy 2.2 keV
- Lithography

BL 2 modification in progress
- ISAS Dortmund
- White beam at DELTA bending magnet, critical energy 2.2 keV
- Energy and wavelength dispersive x-ray fluorescence spectroscopy

BL 3 and BL 4 modification in progress
- Technische Universität Dortmund
- FEL

BL 5
- Forschungszentrum Jülich
- U250 electromagnetic undulator
- Energy range: 5 - 400 eV
- Photoemission, coincidence measurements, spectroscopy

BL 8
- Universität Wuppertal
- Superconducting asymmetric wiggler (SAW), critical energy 7.9 keV
- Energy range: 1 - 30 keV
- Focus on material science, EXAFS, QEXAFS, ReflEXAFS, XRD

BL 9
- Technische Universität Dortmund
- Superconducting asymmetric wiggler (SAW), critical energy 7.9 keV
- Energy range: 4 - 30 keV
- X-ray reflectivity, (surface) x-ray diffraction, SAXS, XSW, inelastic x-ray scattering

BL 10 in preparation
- Universität Siegen/Universität Wuppertal
- Superconducting asymmetric wiggler (SAW), critical energy 7.9 keV
- Energy range: 4.5 - 16 keV
- X-ray diffraction, absorption spectroscopy (EXAFS)

BL 11
- Technische Universität Dortmund
- U55 permanent magnet undulator
- Energy range: 55-1500 eV
- Photoemission spectroscopy, photoelectron diffraction

BL 12
- Technische Universität Dortmund
- White beam at DELTA bending magnet, critical energy 2.2 keV
- Energy range: 5 - 220 eV
- Photoemission spectroscopy

Synchrotronstrahlung: Startschuss zur NRW-Forschungsschule

Mit DELTA, der Dortmunder Elektronen Speicherring Anlage, verfügt die TU Dortmund weltweit als einzige Hochschule über eine eigene Synchrotronstrahlenquelle. Jetzt wird bis zu 30 Doktorandinnen und Doktoranden die Möglichkeit gegeben, in der neuen NRW-Forschungsschule, die Anfang Juli eröffnet wurde, strukturiert auf dem Gebiet der Forschung mit Synchrotronstrahlung in den Nano- und Biowissenschaften zu forschen und zu promovieren. Damit ist DELTA weltweit die Strahlenquelle, an der die meisten Doktorandinnen und Doktoranden im Rahmen eines speziellen Programms ausgebildet werden.

Der Teilchenbeschleuniger DELTA auf dem Campus der TU Dortmund - Kernstück der NRW-Forschungsschule - erzeugt hochintensive Röntgenstrahlung. Mit dieser „Synchrotronstrahlung“ untersuchen die 30 Doktoranden grundlegende und angewandte Probleme aus der Physik, Chemie, Biochemie und der Medizin, die sich alle nur mit dem Einsatz dieser Strahlung lösen lassen. Beispiel hierfür sind nanostrukturierte Materialien wie Halbleiter oder biologische Komponenten wie Fetthüllen und Eiweißschichten. Da diese Messmethoden für die Industrie immer interessanter werden, kooperiert die Forschungsschule auch mit Unternehmen, darunter RWE. Beteiligt sind neben der TU Dortmund noch die Ruhr-Universität Bochum, die Bergische Universität Wuppertal und die Universität Siegen sowie das ISAS – Institute for Analytical Sciences in Dortmund und das Forschungszentrum Jülich. Die Forschungsschule bietet den Doktoranden ein Stipendium sowie ein umfassendes Studien- und Forschungsprogramm inklusive Auslandsaufenthalt.

Im Bild (von links): Feierten zusammen den Startschuss zur NRW-Forschungsschule „Forschung mit Synchrotronstrahlung in den Nano- und Biowissenschaften“: Prof. Bernhard Spaan (Dekan Fakultät Physik), Prof. Ullrich Pietsch (Vorsitzender des „Komitees Forschung mit Synchrotronstrahlung“), Prof. Ursula Gather (Rektorin TU Dortmund), Dr. Beate Wieland (Abteilungsleiterin Ministerium für Innovation, Wirtschaft, Forschung und Technologie), Prof. Metin Tolan (Sprecher der NRW-Forschungsschule) und Prof. Roland Frahm (Festredner von der Bergischen Universität Wuppertal).

TU-Dortmund, Infobrief Juli 2009

The new beamline BL-1 at DELTA

Thorsten Brenner*, Daniela Lietz, Michael Paulus, Ulf Berges, Christian Sternemann, and Metin Tolan.
Fakultät Physik/DELTA, TU Dortmund, D-44221 Dortmund, Germany.
*email: thorsten.brenner@tu-dortmund.de

Deep x-ray lithography (DXRL) is a method to produce various microstructures with a height up to several millimeters. Microstructures are applied in optics, micro mechanics, fluidic, or medical devices. Structures with a lateral resolution up to 2 µm and a high aspect ratio of about 100 can be produced using DXRL [1].
A well-established process for production of microstructures using lithography is the LIGA process [2]. It includes the process steps (x-ray) lithography, electroplating, and molding. A wafer covered with a photo sensitive material (positive or negative resist) is exposed through a mask. This mask consists of an x-ray transparent material, e. g. carbon or titanium, and an absorber material, e. g. gold. The lateral shape of the absorber layer is transferred into the photoresist by shadow projection. Solely the exposed resist areas experience a chemical change regarding the molecular weight. After chemical development the exposed (positive resist) or unexposed (negative resist) material is removed. Afterwards, the micromechanical components can be produced by electroplating and molding.

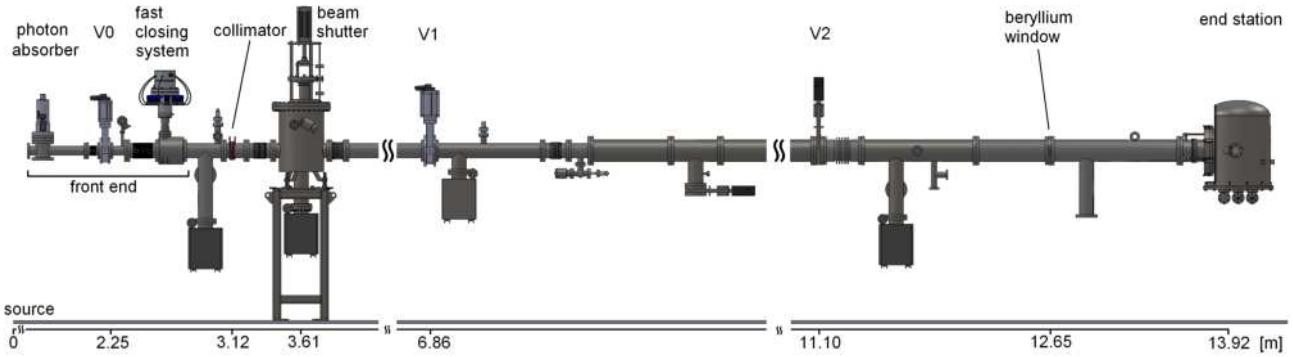

Figure 1: Scheme of the new beamline BL-1 at DELTA.

In 2010 the construction of beamline BL-1 has been finished. This beamline uses white radiation generated by a 1.5 T bending magnet with a critical energy of 2.2 keV. BL-1 consists of three main valves, a photon absorber, a fast closing valve system, a collimator, a beamshutter, and a water cooled beryllium window with a Be-thickness of 127 µm. A scheme of BL-1 is shown in Figure 1. The end station contains a servo motor with a wafer-mask-mounting system enabling a vertical movement of 4-inch wafers across the photon beam. This so called exposure chamber operates under high vacuum conditions. Because of the beam width of approximately 12 cm at the end station it is suitable for full wafer exposure. Four ion getter pumps generate stable vacuum conditions of 10^{-9} mbar in the section connected to the storage ring, which is seperated from the end station by the beryllium window. The safety installations (interlock system for the hutch, warning signs, etc.) and the control of beamshutter and photon absorber have been wired with a programmable logic controller (PLC), which has been programmed for BL-1. All software and hardware components have been tested successfully.
First tests concerning the beam position, which were performed by an exposure of photo sensitive paper, show

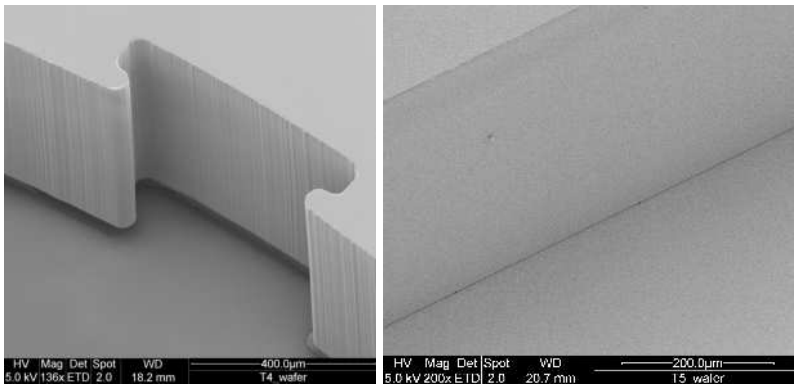

Figure 2: SEM images of the developed wafers exposed at BL-1.

an intensity maximum inside the beryllium window aperture. The beam characterisation indicates a centered Gaussian profile in vertical direction. Thus, the essential requirements for deep x-ray lithography at BL-1 are established.
First lithography exposures of SU-8 (negative resist) covered silicon wafers at BL-1 were performed successfully. The exposure times have been between five and ten minutes yielding a deposited bottom dose of 15 to 25 J/cm^3. The top to bottom dose ratios were about 5. SEM images of the developed wafers show high quality structures (see Figure 2). The shape of the mask absorber structure has been transferred exactly into the photo sensitive resist. The aspect ratio was determined to 100. The adhesion between photoresist and silicon substrate is quite good. Moreover the roughness of the perpendicular walls can be reduced by using a titanium mask instead of a graphite mask. The experimental results at BL-1 agree with similar experiments [3, 4].
Consequently BL-1 is ready to produce high quality microstructures in compliance with industrial requirements. Systematic studies to find optimal exposure parameters are planned for 2011. It will be necessary to optimise the exposure time and the deposited dose as well as the top to bottom ratio of the deposited dose. Moreover there is a need to build up a new end station for exposing more wafers in a beamtime.

Acknowledgement
We would like to thank Dr. Alex von Bohlen (Leibniz-Institut für Analytische Wissenschaften - ISAS - e.V.) for taking the SEM images. We also would like to thank the DELTA machine group for providing synchrotron radiation and for technical support. T. Brenner thanks the NRW Forschungsschule 'Forschung mit Synchrotronstrahlung in den Nano- und Biowissenschaften' for financial support.

References

[1] V. Saile, U. Wallrabe, O. Tabata, J.G. Korvink, O. Brand, G.K. Fedder, C. Hierold (Eds.), *LIGA and its applications*, Wiley-VCH (2009).

[2] *http://www.imt.kit.edu/liga.php*

[3] P. Cohan, R. Giasolli, S. Ledger, K. Lian, Z. Ling, J. Göttert: *Microsystem Technologies* **6** (2000), 94 - 98.

[4] G. Aigeldinger, C.-Y. P. Yang, D. M. Skala, D. H. Morse, A. A. Talin, S. K. Griffiths, J. T. Hachman, J. T. Ceremuga: *Microsystem Technologies* **14** (2008), 277 - 286.

Spin-polarized electron energy loss spectroscopic studies of ultrathin films

J. Rajeswari [1] , L. Baumgarten [1] , B. Kuepper [1] , H. Ibach [2] , C.M. Schneider [1]
[1] Institute of Solid State Research, IFF-9, Forschungszentrum Juelich, Germany
[2] Institute of Bio- and nanosystems, IBN-3, Forschungszentrum Juelich, Germany

The elementary excitations at crystalline surfaces are studied extensively using Electron Energy Loss Spectroscopy (EELS). The spin-polarized version of EELS (SPEELS) is a unique method to study the large wavevector spin waves and their dispersion in ultrathin magnetic films [1]. The understanding of such magnetic excitations reveals microscopic spin dynamics in the magnetic systems.

In my thesis work, the spin wave excitations of ultrathin ferromagnetic films and molecules adsorbed on those films will be investigated extensively using SPEELS and polarized synchrotron radiation. For this, during the last year an EELS spectrometer as well as a separate sample preparation chamber has been setup, tested and characterized. This will be described below in some detail.

Setup and Characterization of SPEELS spectrometer

A new EELS spectrometer has been designed for the study of spin waves and built at Forschungszentrum Jülich, Germany. The design permits the study of both in plane and perpendicularly polarized thin films. A detailed description of the spectrometer is given in Ref. [2, 3]. A schematic of our spectrometer is shown in Fig. 1.

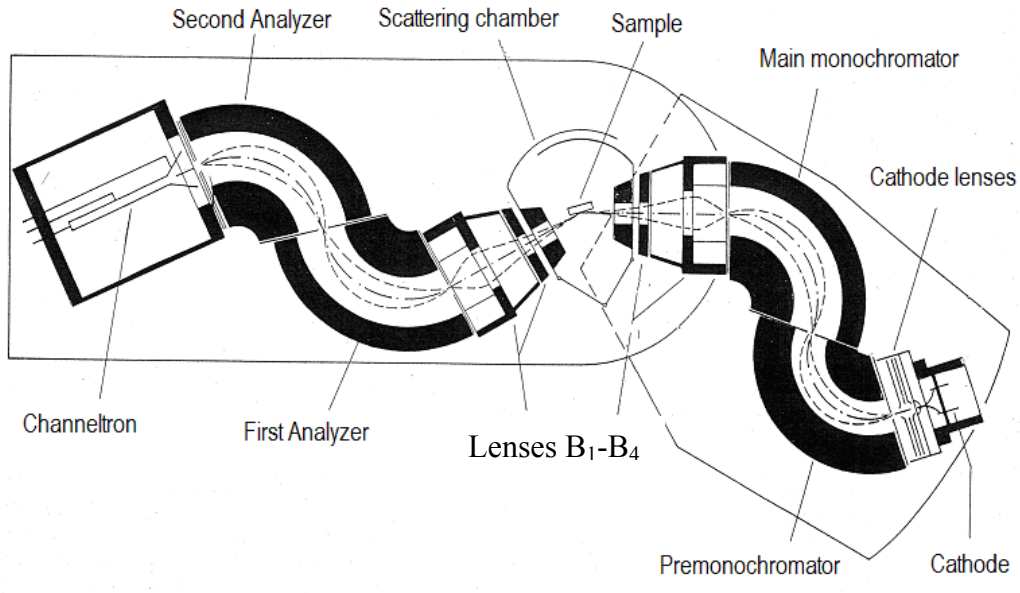

Figure 1: EELS spectrometer designed by Ibach

The SPEELS spectrometer has been setup in a separate UHV chamber and its functionality has been tested. Tuning the spectrometer demands carefully optimizing the potentials applied to all the elements of the spectrometer shown above (about 40 different potentials). This huge parameter setting together with the rotational position

of the analyzer provides a room for multidimensional parameter room for optimization.

A routine has been developed which automatically optimizes all the potentials applied to the spectrometer in order to achieve high monochromatic current at the detector for a fixed resolution. Also the routine allows for a complete automatic adjustment to a pre determined high final resolution starting from a moderate resolution.

At this point of time we have achieved an energy resolution of $\Delta E = 11$ meV with a high monochromatic current of 2 nA at the detector which is shown in Fig. 2. This is very reasonable for the study of magnon excitations. Also as test, we took an energy loss spectrum from an impure Cu (100) sample. As can be seen from Fig. 3, vibrational losses are observed due to some hydrocarbons adsorbed on the surface.

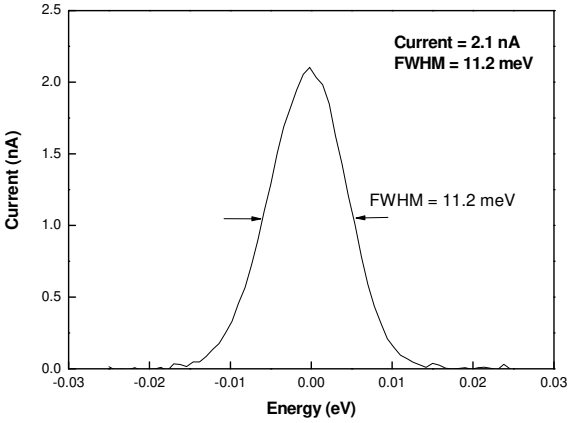

Figure 2: Elastic peak showing energy resolution of the spectrometer

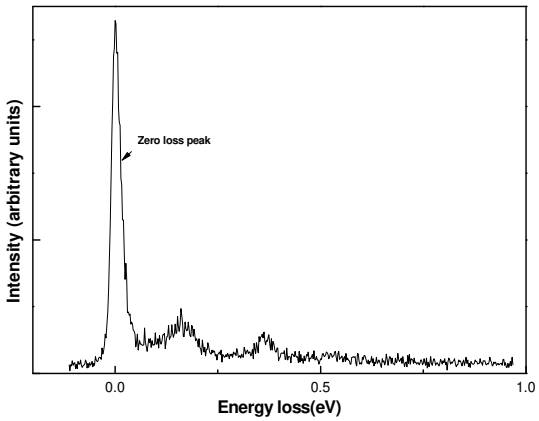

Figure 3: Electron energy loss spectrum of impure Cu surface

Setup and test of preparation chamber

To achieve good control of surface properties and its cleanliness the experiments will be performed in ultrahigh vacuum in an apparatus especially designed for this purpose.

Recently, we have built a preparation chamber for the preparation of good quality ultrathin films. The chamber is equipped with an MBE evaporator for the preparation of ultrathin epitaxial films. The samples will be characterized using the surface analysis techniques, such as Auger Electron Spectroscopy (AES) and Low Energy Electron diffraction (LEED) which are built in the chamber. The sample can be heated by resistive heating to about 900K. The chamber is also equipped with a quadrupole mass spectrometer (QMS) for measuring the relative amounts of different residual gases inside the chamber. The atomic layer-by-layer growth of epitaxial films is controlled by monitoring oscillations in the intensity of the diffracted beams in the MEED pattern.

The prepared samples can be transferred between the preparation chamber and the SPEELS chamber by a linear magnetic transfer.

The first system of investigation is Co on Cu (100) and we are able to prepare good quality Co films of required thickness as confirmed by MEED and AES (Fig. 4, 5) and transfer it to the SPEELS chamber.

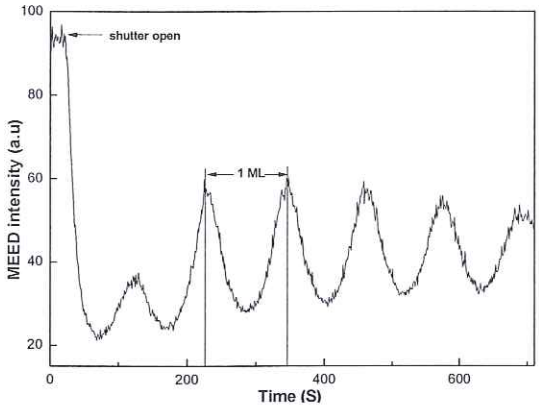

Figure 4: Intensity of specularly reflected MEED spot Vs time during Co deposition

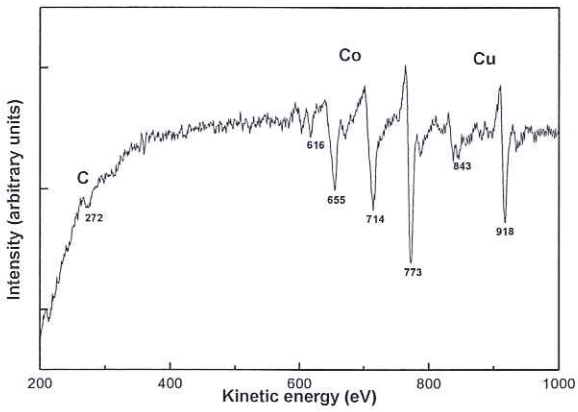

Figure 5: AES spectrum of Co on Cu (100)

Future work

A chamber for the preparation of GaAs photocathode, source of spin-polarized electrons for the experiment will be built up and connected directly with the main chamber.

Spin waves with high energy and momentum will be studied by our classical SPEELS spectrometer for both in-plane and perpendicularly polarized thin films. The samples which will be investigated are pure ultrathin magnetic films, their alloys and molecules (eg., Fe-phthalocyanine) adsorbed on ferromagnetic thin films. The prepared films will also be investigated using polarized synchrotron radiation for the element specific magnetization of ferromagnetic alloys as well as magnetic moments and coupling of molecular layers.

References

1. R. Vollmer, M. Etzkorn, P.S. Anil Kumar, H. Ibach, and J. Kirschner Phys. Rev. Lett. **91**, 147201(2003).
2. H. Ibach, D. Bruchmann, R. Vollmer, M. Etzkorn, P.S. Anil Kumar and J. Kirschner Rev. Sci. Instrum. **74**, 4089(2003).
3. H. Ibach, M. Etzkorn, and J. Kirschner Surface and Interface analysis **38**, 1615(2006).

J. Rajeswari

Ambient air photoelectron nano ionisation detector

C. Zimmer[1,2], J. Schubert[3], U. Kunze[1], T. Doll[2,4]

[1]Werkstoffe und Nanoelektronik, Ruhr-Universität Bochum, Bochum, Germany
[2]adlantis Dortmund GmbH, Dortmund, Germany
[3]Institute of bio- and nanosystems, Forschungszentrum Juelich, Juelich, Germany
[4]Institute of physics, Johannes-Gutenberg-University, Mainz, Germany

Abstract

A nano ioniser suitable for ambient conditions is presented, which exceeds the actual physical limits and parameterisation of conventional photo ionisation detectors. Lanthanum hexaboride (LaB_6) thin films exposed to air show reasonable work function values (accompanied by a moderate surface reoxidation of the films) that make them suitable for photoelectron applications, which finally may employ LEDs instead of discharge lamps. Thus electrical control of molecular ionisation limits is reached.

Introduction

The fundamental concept of many analytical instruments is based on the influx of analytes into the instrument, their ionisation, the acceleration of these molecules through an electric field, the detection and the analysis of the ions. Conventional techniques for charging are corona discharge, atmospheric pressure photo ionisation (APPI), electron impact ionisation (EI) or a radioactive beta particle source, eg. a small piece of ^{63}Ni [1]. However, the risk of molecule fragmentation due to highly accelerated electrons at these ionisation systems is disadvantageous for final substance analysis. If it is possible to sharpen the energies of electrons towards fine adjustment as in two-photon ionisation [2], an alternative gas ioniser for variable pressure might be developed.

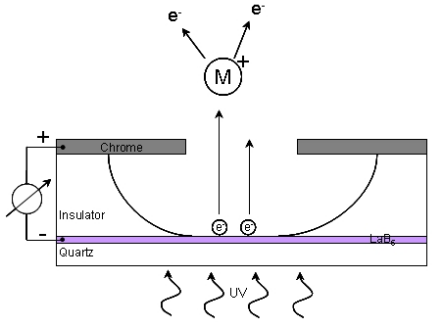

Fig. 1: Lanthanum hexaboride thin film ioniser with a nano-acceleration path for adjusting exact energies using for molecule ionisation without fragmentation.

In this work a nanoscale ioniser (fig. 1) is presented, whose functionality is based on the photoelectric effect. Ultraviolet irradiation will discharge electrons from the thin solid LaB_6 layer, which is deposited on an UV-transmissive substrate like fused silica. The speciality of the configuration is that generated photoelectrons are brought up to energies of 7 to 18 eV within a nano-electrode arrangement, which does not exceed the mean free path of molecules at 10^5 Pa (70 to 110nm). With precisely defined energies several classes of molecular compounds such as hydrocarbons, solvents, organic and inorganic substances will be brought into ionisation without the risk of molecule fragmentation.

Photoemission of LaB_6

For the perfect emission of LaB_6-electrons challenges come up concerning surface oxides, as surface reactions with adsorbates [3] and, of course, orientations or facets of the material influencing the work function of LaB_6 [4]. The only solution to get photoelectrons out of an untouched LaB_6 film without pre-treatments is matching of UV-LED (available commercially) with the measured work function of thin LaB_6 films, which is in the energy range up to 5 eV depending on substrates [5]. Hence a sintered multifaceted LaB_6 sample was investigated by x-ray photoelectron spectroscopy (XPS) for determining the work function (fig. 2). Due to contaminations including oxygen forming a surface oxide (see fig. 3) the work function of untreated LaB_6 achieved 7.39 eV, which is extremely high contrary to in-situ cleaned LaB_6 [6] samples by either annealing process at 1700K or sputtering process with argon ions under vacuum conditions. In order to evaluate technically processed lanthanum hexaboride thin films for ambient use, the work function of a 100 nm thick layer deposited on different substrates (silicon, sapphire) was analysed by ultraviolet photoelectron spectroscopy (UPS). The calculated work function of the investigated samples is indeed found to be within the range

of 3 ¯ 4 eV (≅=413 nm ŭ 310 nm) with the exception of the results yield from the ceramic and the sapphire sample (฿=4.58eV).

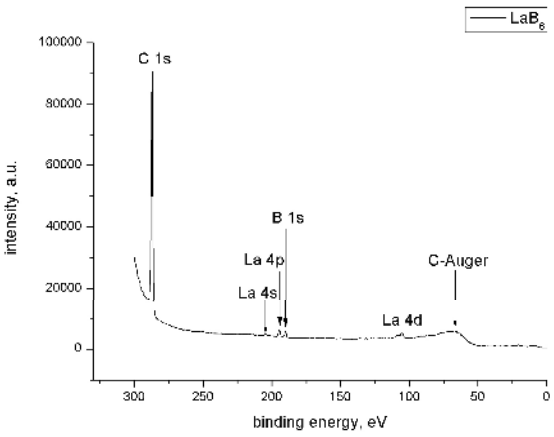

Fig. 2: Overview of the x-ray photoelectron spectrum of sintered LaB_6.

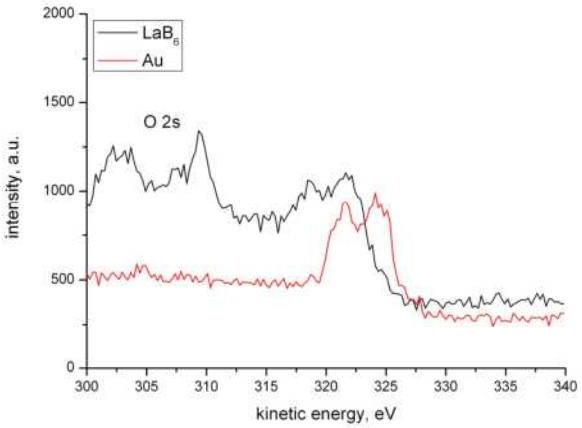

Fig. 3: Spectra of Au and LaB_6 with oxygen peaks near the Fermi edge.

Ionisation measurements

The nanoscale ioniser based on LaB_6 was fabricated into a small electron accelerating element (see fig. 1), which was electrically characterised in an evacuated chamber afterwards. Ionisation measurements with different gaseous solvents were performed additionally under moderate vacuum conditions. Here, the suitability of lanthanum hexaboride as an electron generator and ioniser of incoming solvents such as methanol, nitrogen, air and IPA was proven (see fig. 4). Actually, measurements at ambient conditions follow, whereby a proper adjustment of the nanoscale acceleration path allowing the transfer to the atmosphere needs further corrections.

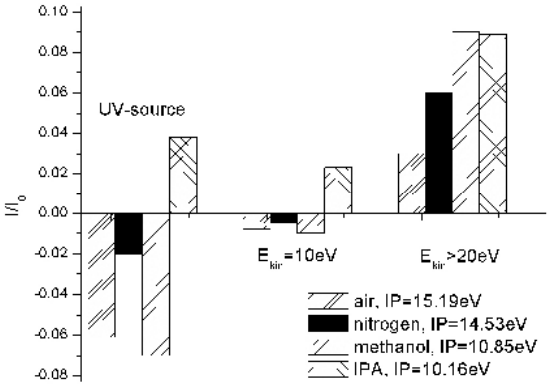

Fig. 4: Ionisation of different gases using the energy of pure UV light and the kinetic energy of nano-accelerated LaB_6 photoelectrons matching the compounds ionisation levels. By exceeding of the UV-source energy (10.6eV) other solvents can be ionised in addition to isopropyl alcohol (IPA).

References

[1] Kienitz H., *Massenspektrometrie*, Verlag Chemie GmbH (1968), Weinheim
[2] Deng Z., Eberly J., *J. Opt. Soc. Am. B*, 2 (1985), p. 486-493
[3] Goldstein B. and Szostak D., *J. Surface Science*, 74 (1978), p. 461-478
[4] Gesley M. and Swanson L.W., *Surface Science*, 146 (1984), p. 583-599
[5] Zimmer C., Medyanyk K., *Procedia Chemistry*, 1 (2009), p. 1119-1122
[6] Lafferty J. M., *Journal of Applied Physics*, Vol. 22, No. 3 (1951), p. 299-309

Characterization of poly(organosiloxane) nanocapsules with iron oxide core by SAXS

Johannes Möller*,[a], Martin A. Schroer[a], Patrick Degen[b], Melek Cebi[b], Michael Paulus[a], Christoph J. Sahle[a], Alexander Nyrow[a], Heinz Rehage[b] and Metin Tolan[a]

[a] *Fakultät Physik/DELTA, TU Dortmund, Maria-Goeppert-Mayer-Str. 2, D-44227 Dortmund, Germany;*
[b] *Fakultät Chemie/ Physikalische Chemie II, TU Dortmund, Otto-Hahn-Str.6 , D-44227 Dortmund, Germany*

*email: johannes.moeller@tu-dortmund.de

In this report we describe recent results of our small angle x-ray scattering (SAXS) experiments to study the internal structure and the formation process of poly(organosiloxane) nanocapsules filled with an iron oxide core of different size.

Iron oxide nanoparticles offer different important applications in magnetic recording, solar energy transformation, electronics and chemical catalysis [1]. Concerning nanocapsules with solid cores most work has been focused on the synthesis of these materials. Very little attention has been directed towards the interaction between the shell and the core or to the modification of the core within the capsule [2]. The possibility of removing partially or completely the magnetic core of the capsule by chemical etching processes offers the opportunity of assembling hollow poly(organosiloxane) nanocapsules, which can be used to produce new types of microreactors [3, 4, 5] or for the therapeutic delivery of drugs, genes or radionuclides [6]. However for this purpose the knowledge of the structural assembly of these capsules is essential for the development of reliable drug containers. The synthesis approach of the nanoparticles has two essential features: (A) the synthesis of iron oxide nanoparticles induced by a chemical precipitation process in reverse micellar cavities [7]; (B) preparation of the thin poly(organosiloxane) shell around the aqueous ferrofluid droplet [8]. The organic shell around the droplet surface was formed through the hydrolysis and polycondensation of octadecyl-trichlorosilane (OTS) [9]. During the polymerization process the original stabilizing surfactant shell was replaced by the very thin coherent OTS-layer. Because of the release of HCl during the polymerization the magnetic core was dissolved as seen in a colour change of the samples. Due to the polymerization, the nanocapsules are extreme stable and can be purified by subsequent washing cycles with water without being damaged. The cleaned nanocapsules (with or without cores) can be dried in vacuum and redispersed in various organic liquids. While dynamic light scattering and UV-Vis measurements were already applied, there is a lack of information concerning the size and the structure of the iron oxide core inside the capsule. Here, small angle X-ray scattering experiments can give valuable information as this technique is excellently suited to probe colloidal particles of a size of several Angstroms up to a few nanometers in solution.

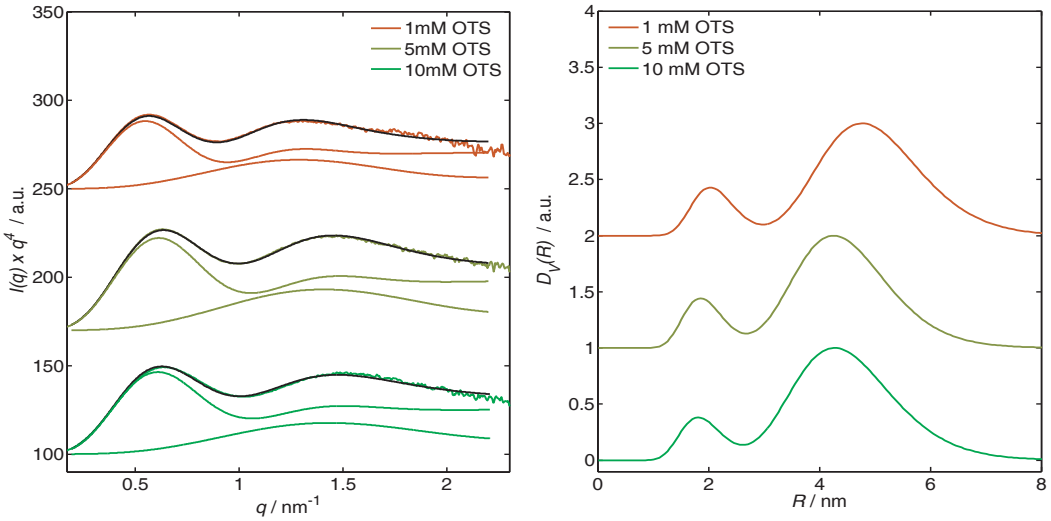

Figure 1: (a) Measured intensities in Porod plot with the refinement using a bimodal distribution function (black) and the contributions to the intensity from the unimodal fractions of the distribution (respective colour). (b) Resulting volume distribution function.

Measurements were performed at beamline BL9 of DELTA employing the SAXS setup already described in Ref. [10]. A photon energy of 10 keV and a sample-to-detector distance of about 1353 mm allowed to cover a

q-range from 0.1 up to 2.5 nm^{-1}. The exposure time was chosen to be 600 - 1800 s due to the low concentrations used. Low particle concentration were used to be able to determine the form factors without contributions of an intermolecular structure factor. As the solvent in which the nanocapsules are dissolved affects the glue typically used to fix the window materials of the usually used sample cells a special custom-built sample cell was constructed and employed [11].

In our study nanocapsules with different compositions of the educts forming the iron core were investigated as a function of the OTS concentration used in the synthesis process. Figure 1 shows the SAXS signal of the different particles in the so-called Porod plot, i.e. $I(q) \cdot q^4$, together with the refinement to the experimental data. Using a bimodul distribution function for the iron oxide core together with the form factor of sphere gave the best fitting results to the data. The corresponding distribution functions are also depicted.

As can be seen, for the lowest OTS concentration the distributions for all synthesis compositions are broad and nearly similar. Hence, the compositions has only a minor influence on the particles' shape at these conditions. Increasing the OTS concentrations results in a reducing of the mean particle size as well as in a tightening of the distribution due to the partial dissolving of the iron oxide core. Furthermore, this OTS dependency is different for the various compositions studied. These measurements were supplemented by additional SAXS studies performed at BW4, HASYLAB, as well as by anomalous SAXS (ASAXS) studies at B1, HASYLAB, respectively.

The authors like to acknowledge the DELTA machine group for providing synchrotron radiation and technical support.

References

[1] C.N.R. Rao, A. Müller, A.K. Cheetham (eds), *The chemistry of nanomaterials: synthesis, properties and application.* Wiley, Weinheim (2004).

[2] K. Kamata, Y. Lu, Y. Xia, *J. Am. Chem. Soc.* **125**, 2384 (2003).

[3] Y. Lvov, F. Caruso, *Anal. Chem.* **73**, 4212 (2001).

[4] Y. Lvov, A. Antipov, A. Mamedov, H. Möhwald, G.B. Sukhorukov, *Nano Lett.* **1**, 125 (2001).

[5] O.P. Tiourina, A.A. Antipov, G.B. Sukhorukov, N.L. Larionova, Y. Lvov, H. Möhwald, *Macromol. Biosci.* **1**, 209 (2001).

[6] Q.A. Pankhurst, J. Connolly, S.K. Jones, J. Dobson, *J. Phys. D: Appl. Phys.* **36**, 167 (2003).

[7] C. T. Seip, E. E Carpenter, C. J. O'Connor, *IEEE Trans. Magn.* **34**, 1111 (1998).

[8] P. Degen, A. Shukla, U. Boetcher, H. Rehage, *Colloid Polym. Sci.* **286**, 159 (2008).

[9] M. Husmann, H. Rehage, E. Dhenin, D. Barthes-Biesel, *J. Colloid Interface Sci.* **282**, 109(2005).

[10] C. Krywka, C. Sternemann, M. Paulus, N. Javid, R. Winter, A. Al-Sawalmih, S.B. Yi, D. Raabe, M. Tolan, *J. Synchrotron Rad.* **14**, 244 (2007).

[11] J. Möller, *Strukturelle Untersuchung von Eisenoxid-Nanopartikeln mittels Röntgenkleinwinkelstreuung*, diploma thesis, TU Dortmund (2010).

Local atomic and electronic structure of Ag clusters deposited on SiO_2 substrates

Sabrina Hoffmann*,[a], Stefanie Duffe[a], Stefan Balk[b] Ralph Wagner[b], Christian Sternemann[c], Michael Paulus[c], Christoph J. Sahle[c], Martin A. Schroer[c], and Heinz Hövel[a]

[a] *Fakultät Physik/Experimentelle Physik I, TU Dortmund, Otto-Hahn-Str. 4, 44221 Dortmund, Germany;*
[b] *Bergische Universität Wuppertal, Fachbereich C, Fachgruppe Physik, Gaußstr. 20, 42119 Wuppertal, Germany;*
[c] *Fakultät Physik/DELTA, TU Dortmund, Maria-Goeppert-Mayer-Str. 2, 44227 Dortmund, Germany;*

*email: sabrina.hoffmann@physik.uni-dortmund.de

In this report we describe very first results of our x-ray absorption near edge structure (XANES) spectroscopy measurements at the Ag L_3 absorption edge of Ag clusters on SiO_2 compared to Ag and Ag_2O reference films performed at the synchrotron radiation facility DELTA, TU Dortmund.
Clusters assembled materials are of great impact for future applications in science and nanotechnology [1, 2, 3]. In particular, advances in metal cluster-beam technology allow experiments on free and supported or embedded clusters resembling nanostructures in realistic, technical relevant environments. Optical properties of noble metal clusters and nanostructures such as their UV-VIS absorption band alter significantly with size, shape and interparticle spacing as well as with the properties of the local environment. This yields a wide range of further applications such as optical biosensors [4] or metal nanoantennas as promising systems for field-enhanced spectroscopy or nanoscopic light emitters [5]. XANES yields unique structural and chemical information on supported and embedded clusters. It is well suited to investigate the chemical environment of noble metal clusters and allows the study of changes of the unoccupied density of states (uDOS). The focus of our study is set on the following two topics:

(i) Exposure to air after sample preparation leads to a partial oxidation of the Ag clusters which affects the properties of the clusters significantly. Particularly, the formation of Ag_2O is of relevance due to its similarities with its isoelectronic analogue Cu_2O, with obvious links to high temperature superconductors [6]. The oxidation of supported and embedded clusters was examined using optical spectroscopy, where one can see a shift in the plasmon energy after exposing the clean Ag clusters to air (Figure 1, small). Then we performed XANES measurements at the Ag L_3 edge [7] of the same cluster sample at DELTA, BL8.
(ii) The uDOS of clusters is different from that of bulk Ag because clusters connect molecular and solid state physics which manifests - depending on their size - in quantized or bulk-like properties. Thus, the uDOS is strongly influenced by the size which is under investigation.
In our studies we performed measurements at BL8, DELTA, where we used a newly installed vacuum setup to avoid x-ray absorption in air and the Si(111) monochromator to investigate the L_3 absorption edge of Ag clusters on SiO_2, a Ag reference film, a Ag_2O reference powder, a Ag_2S reference and a Ag cluster reference which has been transformed to Ag_2S by an external treatment with H_2S.

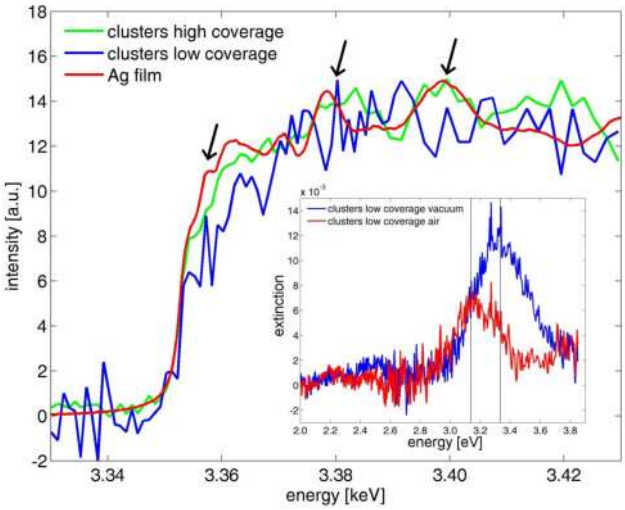

Figure 1: Large: XANES spectra of a Ag film and two different packing densities of Ag clusters. Small: Silver plasmons at low coverage in vacuum before and after exposure to air.

The data show a significant difference between the Ag L_3 edge of the reference film and the signal of deposited Ag clusters (cluster radius 1 nm) with different cluster coverages. It is clearly visible, that the XANES signal of the highest cluster coverage (effective film thickness of approx. 2 nm), for which the Ag clusters form larger particles due to coalescence, looks very similar to that of the silver film reference (Figure 1). However there are remarkable differences (in particular at the energy positions marked with arrows) in the near edge structure

for low coverage (approx. 0.3 nm, Figure 1), for which the clusters stay separated. The investigated Ag_2S clusters, where we performed measurements only for the high coverage, show no significant differences to the Ag_2S reference film, but are clearly distinguishable from the Ag reference sample (Figure 2). Thus, XANES is a suitable method to investigate the differences between electronic properties of bulk Ag, Ag clusters and chemically transformed samples.
In these first measurements it was possible to see the feasibility of the experiment as well as a great potential for gaining additional information on the influence of cluster size as well as cluster coverage. Another sample system of interest will be Ag clusters with a narrow size distribution deposited into polymethylmethacrylate (PMMA) or polydimethylsiloxane (PDMS). Using these polymers it is possible to produce a layer of separate clusters with an effective film thickness of approx. 50 nm [8]. Thus, the higher signal to noise ratio will provide the possibility to measure the size dependent changes in detail. We plan to investigate this kind of samples in the next beamtime at BL8, DELTA, in November.

Although these are first measurements the results are very promising. It is possible to clearly distinguish between the XANES signal at the L_3 absorption edge of the Ag film reference and the Ag cluster sample with low coverage. In addition to the oncoming beamtime at BL8, DELTA, we submitted a proposal to the European Synchrotron Radiation Facility (ESRF), ID26, for 2011. This beamline provides an even higher flux than DELTA with which we will hopefully be able to see differences in the XANES spectrum of the L_3 absorption edges of partly oxidized Ag clusters compared to a Ag reference film with a distinguishable amount of oxide. It will thus be possible to investigate samples with even lower coverage, where the percentage of oxidized material should be high enough to yield a clearly distinguishable change in the L_3 absorption edge compared to the Ag reference.

The authors like to acknowledge the DELTA machine group for providing synchrotron radiation and technical support.

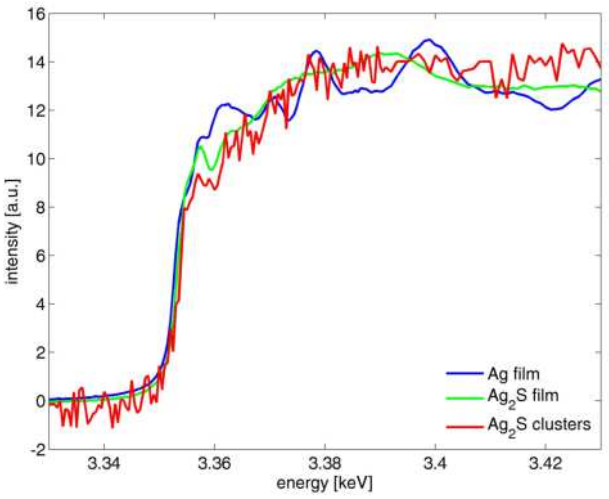

Figure 2: XANES spectra of a Ag_2S film and Ag_2S clusters. No significant differences visible between the Ag_2S reference and the clusters.

References

[1] R.E. Palmer, S. Pratontep, and H.-G. Boyen, Nature Materials **2**, 443 (2003).

[2] Z.Y. Li, N.P. Young, M. Di Vece, S. Palomba, R.E. Palmer, A.L. Bleloch, B.C. Curley, R.L. Johnston, J. Jiang, and J. Yuan, Nature **451**, 46 (2008).

[3] S. Duffe, N. Grönhagen, L. Patryarcha, B. Sieben, C. Yin, B. von Issendorff, M. Moseler, H. Hövel, Nature Nanotechnol. **5**, 335 (2010).

[4] A.J. Haes and R.P. van Duyne, J. Am. Chem. Soc. **124**, 10596 (2002).

[5] J. Merlein, M. Kahl, A. Zuschlag, A. Sell, A. Halm, J. Boneberg, P. Leiderer, A. Leitenstorfer, and R. Bratschitsch, Nature Photonics **2**, 230, (2008).

[6] O. Sipr, F. Rocca, and G. Dalba, J. Synchrotron Rad. **6**, 770 (1999).

[7] P. Behrens, S. Aßmann, U. Bilow, C. Linke, and M. Jansen, Z. anorg. allg. Chem. **625**, 111 (1999).

[8] L. Ravagnan, G. Divitini, S. Rebasti, M. Marelli, P. Piseri and P. Milani, J. Phys. D **42**, 082002 (2009).

[9] H. Hövel, S. Fritz, A, Hilger, and U. Kreibig, Phys. Rev. B **48**, 18178 (1993).

[10] H. Hövel, A. Hilger, I. Nusch, and U. Kreibig, Z. Phys. D **42**, 203 (1997).

Characterization of X-ray Standing Waves Fields

M. Brücher[1], A. von Bohlen[1], R. Wagner[2], R. Hergeröder[1]

[1] Leibniz-Institut für Analytische Wissenschaften – ISAS e.V., Bunsen-Kirchhoff-Str. 11, 44139 Dortmund
[2] DELTA, University of Dortmund, Maria-Goeppert-Mayer-Str. 2, 44221 Dortmund

During the last beamtimes at DELTA, various types of element distributions at interfaces have been analyzed using X-ray standing waves (XSW). The concentration profiles of samples like nanoparticles, aqueous solutions or polymer layers could be characterized with nanometre accuracy. However, the limitation of the extension of the XSW field perpendicular to the reflecting surface still remained an unanswered question.
The experiments presented at the user meeting 2010 were dedicated to the measurement of the vertical intensity distribution of different XSW fields. For this purpose, first a series of gold nanoparticles of different size (25 – 250 nm in diameter) placed on silicon wafers were analyzed by XSW in combination with SEM measurements.
Nanoparticles are particularly suited to this task, as here the vertical element distribution is well-known. The fluorescence curves obtained in the measurement were compared to simulated signals, which were calculated for ideal XSW fields of constant vertical intensity distribution.
In the case of small particles, a good accordance of experimental and theoretical data was found, but for particles of more than 100 nm in diameter, an increasing discrepancy between measurement and simulation was observed.

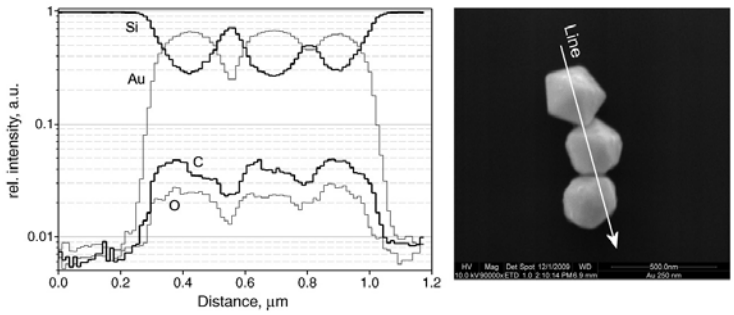

Figure 1: Gold nanoparticles on a silicon wafer. The left diagram shows a line scan of Au Lα fluorescence intensity along the three particles depicted in the SEM image (right). The particle diameter is 250 nm.

The second sample series consisted of polymer layers containing a front of sulfur ions near the surface. By this means, the excitation of markers embedded in a matrix was studied.
In previous investigations of this sample type, which is applied to the development of multilayer organic LEDs, it has been found that for distances of more than 100 nm between the reflecting interface and the front the detected sulfur concentration of the front decreases. Such decrease of concentration is unlikely for the given polymerization mechanism, so the reason for this effect was suspected in an inhomogeneous intensity of fluorescence excitation of the front ions.
By XSW measurements of a series of polymer layers of different thickness with the sulfur front at the top of the layer, the relation between front height over the substrate and the intensity of fluorescence excitation was studied. Comparing these data with those obtained from earlier measurements, it can be concluded that the excitation remains largely constant up to 90 nm above the reflector, for marker positions above this height, the intensity of

fluorescence excitation decreases. The upper limit of the XSW field was detected at z = 140 – 150 nm.

With the experiments performed, the range of applicability of standing waves for the measurement of element distributions in air or vacuum as well as in a matrix could be estimated. The origin of the detected limitation of fluorescence excitation and of vertical extension of the XSW field can be seen in the limited longitudinal coherence length of the incoming radiation and in the loss of photon coherence during the transition of the beam through the matrix containing the marker atoms or ions.

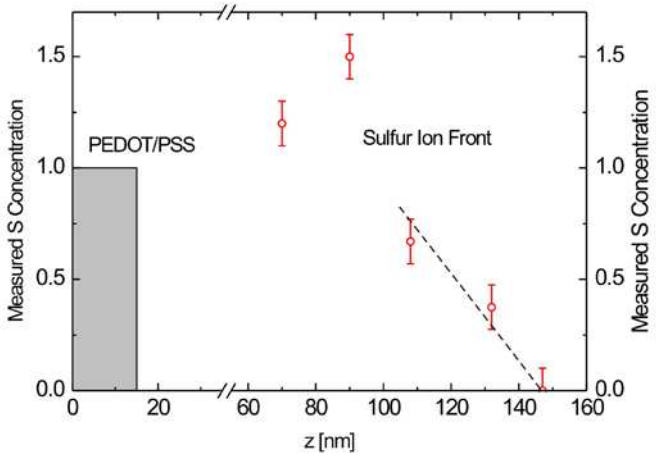

Figure 2: Sulfur distribution in thin polymer layers on silicon wafers. Sulfur is located in the PEDOT/PSS layer at the lower end and in the sulfur ion front at the upper end of the polymer.

1. A. von Bohlen, M. Krämer, C. Sternemann, M. Paulus. The influence of X-ray coherence length on TXRF and XSW for the characterization of nanoparticles observed under grazing incidence of X-rays. J. Anal. At. Spectrom. 24 (2009) 792-800.

2. A. von Bohlen, M. Brücher, B. Holland, R. Wagner, R. Hergenröder. X-ray standing waves and SEM-EDX study of gold nanoparticles. Spectrochim. Acta B 65 (2010) 409-414. DOI:10.1016/j.sab.201004.017

Hydrolysis of Ti-containing alkoxides: Preparation, characterization and stabilization of TiO_2 nanoparticles

S. Pfleiderer, D. Lützenkirchen-Hecht and R. Frahm

Fachbereich C-Physik, Bergische Universität Wuppertal, Gaußstr. 20, 42097 Wuppertal, Germany

TiO_2 nanoparticles have a large field of applications, e.g. as a hydrogen storage material [1], in Li batteries and as a catalyst [2]. Especially in the field of catalysis, there are some desirable characteristics the material should have: The material should have a high anatase concentration. The surface of the material should be as large as possible [2]. To get transition metal oxide nanoparticles, the sol-gel method is an often used synthesis process.
Advantages of sol-gel processes are the possibility to synthesize large amounts of the material (useful for industry) and to prepare thin films from the resulting suspensions. Disadvantages are that the desired characteristics are difficult to combine. For example if a high degree of crystallinity is achieved, particles are usually large and phase transitions occur. A known method to prepare powders with anatase crystalline phase is to hydrolyse an alkoxide in an alkaline water solution [2]. Problems occurring are an increasing particle size with increasing pH [3] value and a high amorphous concentration in case of the often investigated sodium hydroxide (NaOH) [4]. Samples prepared in acidic water solutions show strong differences between different acids in connection with the amount of amorphous phase [4]. So there is a possibility that the use of alkaline solutions for the preparation may lead to powders with a high crystallinity if a suitable liquid is found. The problem of the particle size may be controlled by using higher water to alkoxide ratios which is known to decrease the particle size [4].
For first experiments, we have used sodium hydroxide (NaOH) and potassium hydroxide (KOH). A possibility to prepare suspensions for thin film preparation is to ultrasonicate the fluids during the chemical reaction. Powders are prepared with and without ultrasonication for comparison. The dried powders are annealed at 350°C, 400°C, 450°C and 500°C for four hours.
Another possibility to prepare stable anatase nanoparticles is to prepare TiO_2/ZrO_2 composites [5]. The ZrO_2 network avoids agglomeration of particles to larger ones. Materials of TiO_2/ZrO_2 are also interesting because of their augmented catalytic activity. Samples are prepared with water to alkoxide ratio of 160:40 mmol. Pure TiO_2 and ZrO_2 powders are prepared for comparison. Powders were annealed as described above.

Transmission x-ray absorption performed at BL 8 at DELTA and BL C at HASYLAB and x-ray diffraction experiments show obvious structural differences between the samples made in alkaline reaction media with and without ultrasonication. For example, the samples prepared in NaOH and KOH, particles of the annealed samples are larger in the powders prepared under ultrasonication (Fig. 1), which can be determined by x-ray diffraction. The XANES spectra show differences in the degree of crystallinity in the samples prepared with and without ultrasonication. Quantitative analysis was made by linear combination fits with reference samples. EXAFS spectra were fitted with theoretical absorption structures.

In the case of the composite powders, only the samples of pure TiO_2 and the ones with TiO_2:ZrO_2=10:1 show diffraction peaks and characteristics of the anatase structure in the XANES spectra. In these samples, the fraction of the amorphous phase decreases with increasing annealing temperature. In all other samples, the amorphous concentration stays

nearly constant (Fig. 2), probably because the crystallisation is impeded by the ZrO_2 network, which separates the TiO_2 clusters from particles necessary for further crystallisation.

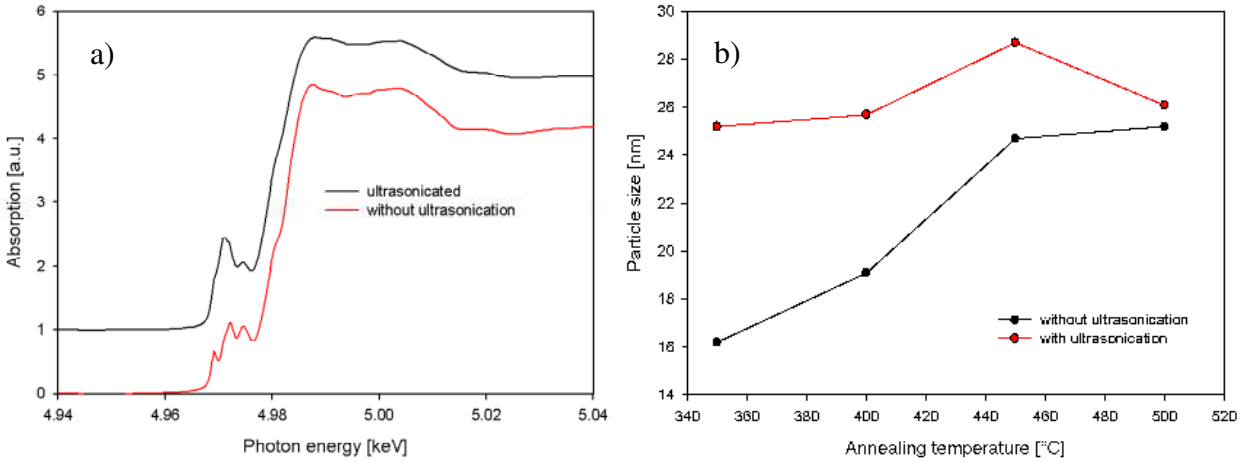

Fig. 1: a) Near edge absorption spectra of TiO_2 samples prepared with 1 M NaOH annealed at 400°C. Significant structural differences can be observed especially in the pre-edge region. b) The particle sizes of the powders synthesized in 1M KOH with and without ultrasonication after annealing. The sizes of the particles in the ultrasonicated powders are larger.

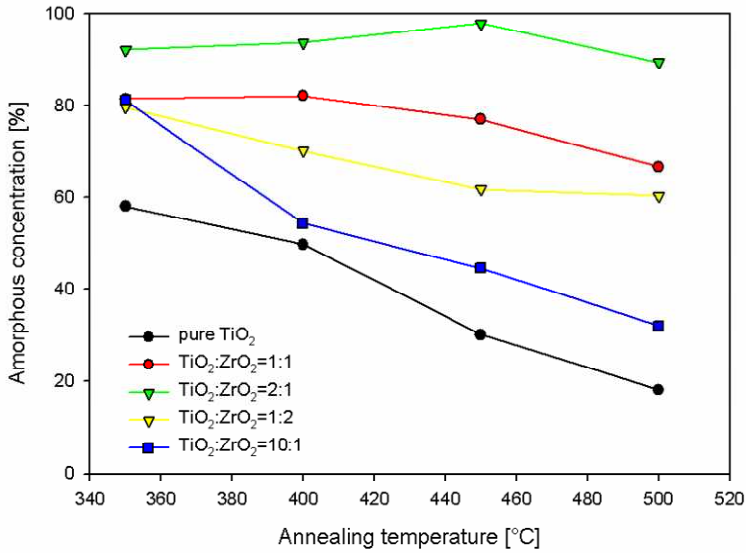

Fig. 2: Amorphous contents on the TiO_2-ZrO_2 composite powders determined from linear combination XANES analysis. Only in the pure TiO_2 and the TiO_2:ZrO_2=10:1 samples significant crystallisation occurs.

References

[1] S.H. Lim et al., Inorg. Chem. 44, 4124-4126, 2005
[2] R. Rossmanith et al, Chem. Mater. 20, 5768-5780, 2008
[3] S. Mahshid, M. Askari, M. Sasani Ghamsari, J. Mater. Proc. Technol., 189, 296-300, 2007
[4] S.L. Isley, R. Lee Penn, J. Phys. Chem. B, 110, 15134-15139, 2006
[5] S.H. Elder et al., Chem. Mater., 10, 3140-3145, 1998

Temperature induced phase separation and nanocrystal formation in bulk amorphous $Si_xGe_yO_z$

A. Nyrow[1], Ch. J. Sahle[1], C. Sternemann[1], R. Wagner[2], A. Hohl[3] and M. Tolan[1]

[1]Fakultät Physik/DELTA, TU Dortmund, D-44221 Dortmund, Germany
[2]Fachbereich C- Abteilung Physik, Bergische Universität Wuppertal, D-42097 Wuppertal, Germany
[3]Institute for Materials Science, Darmstadt University of Technology, D-64287 Darmstadt, Germany

Materials containing Si and Ge nanocrystals embedded in an oxide matrix are promising candidates for new (opto)-electronic applications, e.g. for the development of high-efficient photoluminescent devices [1] or fast and stable non-volatile memory devices [2]. Here, amorphous $Si_xGe_yO_z$ serves as a starting material for the production of nanocrystals. Despite the relevance of this material for technological applications, detailed spectroscopic studies of its microscopic bulk structure in the native and annealed state are still rare. In this study, x-ray diffraction (XRD) and x-ray absorption near-edge spectroscopy (XANES) at the Ge K-edge have been used to investigate the temperature induced phase separation and nanocrystal formation.

Amorphous $Si_xGe_yO_z$ samples were prepared by evaporation of Si and GeO_2 with a ratio of 0.27/1 in vacuum at 1225°C and subsequent condensation on a molybdenum plate resulting in $Si_{34.5}Ge_{3.5}O_{62}$ and $Si_{44.5}Ge_{2.1}O_{53.4}$ samples. The samples were afterwards annealed for 30 minutes in a nitrogen atmosphere in a temperature range between 200°C and 1200°C.

XANES measurements at the Ge K-edge at 11.103 keV were carried out at beamline BL8 of DELTA using the Si(111) monochromator. The fluorescence was detected using the PIPS and the AMPTEK detectors. The samples were precharacterized by XRD measurements performed at the D8 laboratory diffractometer using the K_α radiation and an angle between the incident beam and the sample surface of 0.3°.

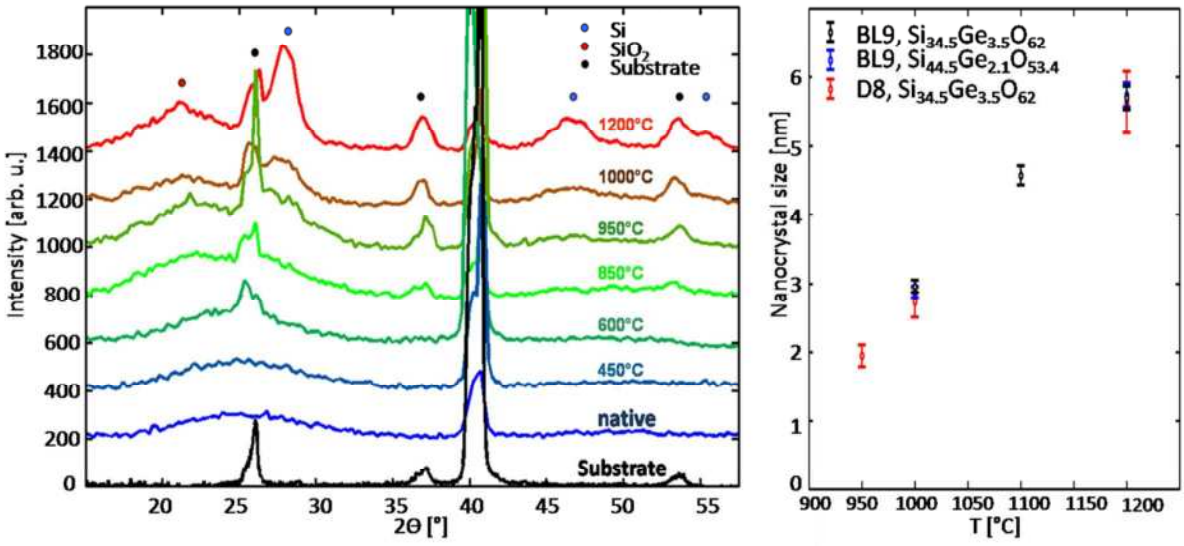

Figure 1: XRD spectra of the native and differently annealed $Si_{34.5}Ge_{3.5}O_{62}$ sample (left) and the estimated nanocrystal size.

XRD spectra of the native and differently annealed $Si_{34.5}Ge_{3.5}O_{62}$ sample are presented in figure 1. A broad contribution of bonding lengths indicates a profoundly amorphous state of

the native sample leading to a broad maximum at 2Θ≈25°. This maximum shifts to smaller scattering angles indicating a structural change which is typical for Si-O bonding length in the amorphous SiO_2 with increasing temperature [3]. Si nanocrystal formation has been observed above 900°C with a mean Si nanocrystal size of 6 nm at 1200°C.

XANES measurements carried out at BL8 are presented in figure 2. In the spectrum of the native sample, no indications of suboxides have been found. With increasing temperature the GeO_2 contribution decreases, which is indicated by the decrease of the spectral intensity at about 11.110 keV accompanied by an increase of the maximum at 11.105 keV. Energy dispersive x-ray spectroscopy results do not show any changes of the stoichiometry, so the changes of the XANES spectra a due to an increase of the pure Ge content on costs of GeO_2 while the total fraction of Ge, independent on its oxidation state, of the whole sample volume remains constant (3,5 vol%). This process occurs above 600°C. The amorphous Ge and GeO_2 reference spectra can be fitted to the measured spectra using the equation $I_{obs}=a\times I_{Ge}+(1-a)\times I_{GeO2}$ where I_{obs} is the observed intensity and *a* describes the fraction of pure Ge in the oxidation stat 0. The estimated GeO_2 fraction decreases from 15-17% to a negligible content at 1200°C while the Ge fraction increases continuously.

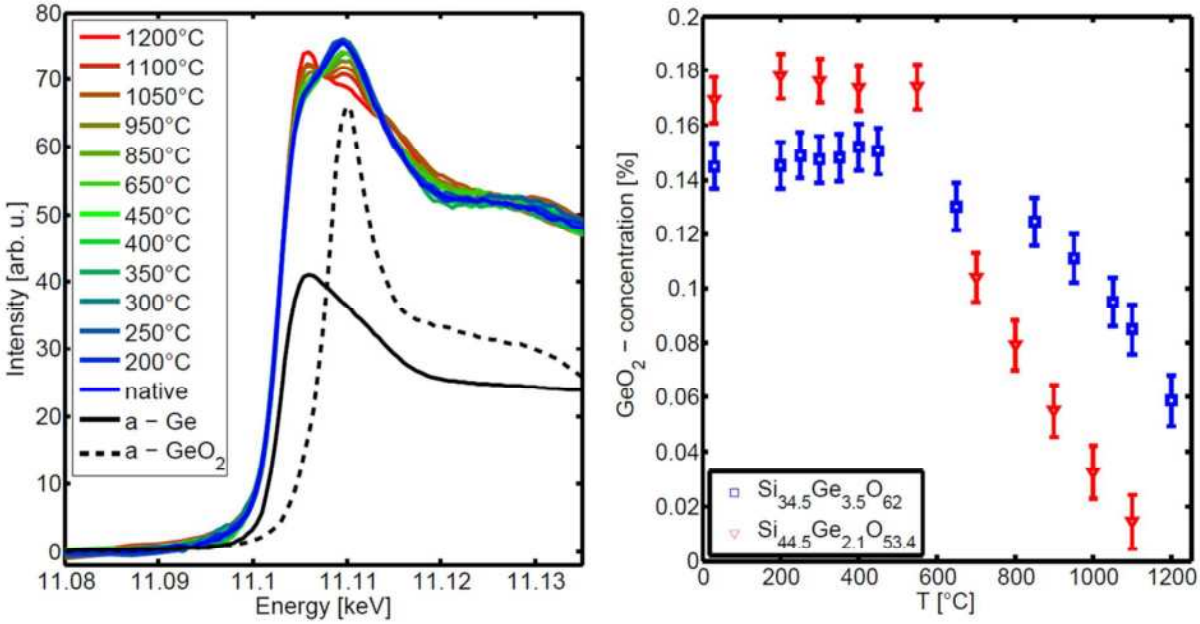

Figure 2: XANES spectra of the native and differently annealed $Si_{34.5}Ge_{3.5}O_{62}$ sample (left) and the estimated GeO_2 content of $Si_{34.5}Ge_{3.5}O_{62}$ and $Si_{44.5}Ge_{2.1}O_{53.4}$ (right).

XRD and XANES results provide valuable information concerning the chemical environment of the Ge atoms and the temperature induced phase separation in amorphous $Si_xGe_yO_z$. The Ge content of the native sample consists of about 83-85% pure Ge and of about 15-17% GeO_2. No suboxides could be observed in contrast to bulk amorphous GeO [4]. With increasing temperature above 600°C a reduction of the GeO_2 content is accompanied by an increase of the pure Ge content. Up to 850°C Ge clusters embedded in an amorphous SiO_2 matrix are growing while the crystallization of the Ge clusters is hindered by the small Ge content in the samples. At 850°C a temperature induced phase separation in the SiO_x content of the samples takes place resulting in Si nanocrystals with an average size of 6 nm at 1200°C, similar to the phase separation found in bulk amorphous SiO [3].

References:

[1] L. Pavesi, L. Dal Negro, C. Mazzoleni, G. Franzo, F. Priolo, Nature **408**, 440 (2000).
[2] W.-R. Chen, T.C. Chang, P.T.Liu et al., Surface & Coating Technology **202**, 1333 (2007).
[3] O.M. Feroughi, C. Sternemann, Ch. J. Sahle et al., Appl. Phys. Lett. **96**, 081912 (2010).
[4] Ch. J. Sahle, C. Sternemann, H. Conrad, A. Herdt et al., Appl. Phys. Lett. **95**, 021910 (2009).

Sub-nanosecond delay of light in CdZnTe crystals

I.A. Akimov[1], T. Godde[1], D.R. Yakovlev[1], H. Mariette[2], and M.Bayer[1]
[1] *Experimentelle Physik II, Technische Universität Dortmund, 44221 Dortmund, Germany*
[2] *CEA-CNRS group "Nanophysique et Semiconducteurs", Institut Néel, CNRS and Université Joseph Fourier, 25 Avenue des Martyrs, 38042 Grenoble, France*

Abstract: We study the propagation of lower branch excitonic polariton in bulk $Cd_{0.82}Zn_{0.12}Te$ using time resolved photoluminescence (PL) and time of flight techniques. Propagation of picosecond optical pulses through a 0.75 mm thick crystal show the time delay up to 350 ps depending on the photon energy. Optical pulses with duration 150 fs are strongly stretched and the spectral dependence of the group velocity is consistent with the dispersion of lower excitonic polariton branch.

When a light photon energy is close to the exciton resonance its group velocity for propagation in a semiconductor may be significantly decreased[1]. At the same time the excitonic polariton energy relaxation in the lower branch is strongly suppressed due to the existence of the phonon bottleneck in the relaxation path[2]. These two facts can be used for long distance coherent propagation for polaritons and realization of long delays for optical pulses.

In this work[3] we investigated bulk $Cd_{0.82}Zn_{0.12}Te$ sample with the thickness of 0.75 mm. The position of the exciton resonance at 1.664 eV is the same in PL and reflectivity spectra, which indicates the absence of exciton localization. At lower energies a broader peak centered around 1.657 eV is observed in the PL spectrum, which is attributed to the excitonic polariton emission from the lower branch. The absence of the emission related to donor or acceptor bound excitons signifies high purity of the samples.

The optical pulse propagation have been studied using spectrometer in conjunction with a streak camera. In the case of spectrally narrow pulses with duration $\tau_D = 1$ ps strong dependence of the pulse delay on the photon energy $\hbar\omega$ is observed [see Fig. 1(a)]. For $\tau_D = 150$ fs the pulses experience strong distortion [see Fig. 1(b)]. The delay time increases when photon energy approaches the exciton resonance and reaches 350 ps at $\hbar\omega$=1.661 eV. The data can be well reproduced using the dispersion relation for lower excitonic polariton branch with well known parameters.

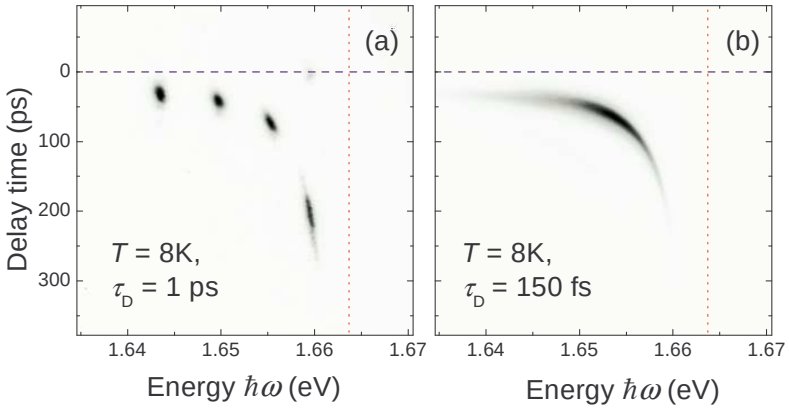

Figure 1: Two dimensional plots in the delay time - energy scale showing the intensity of the transmitted optical pulse in grey-scale for pulse duration (a) $\tau_D = 1$ ps (b) $\tau_D = 150$ fs. The data in (a) are superimposed for 4 optical pulses with different $\hbar\omega$. Horizontal line indicates zero point time, vertical - exciton resonance position.

References

[1] E. S, Koteles, in *Excitons*, edited by E. I. Rashba and M. D. Sturge (North-Holland, Amsterdam, 1982), Chap. 3, p. 83.
[2] F. Askary and P. Y. Yu, Phys. Rev. B **28**, *6165*(1983)
[3] T. Godde, I. A. Akimov, D. R. Yakovlev, H. Mariette, and M. Bayer Phys. Rev. B **82**, *115332* (2010)

Biomineralization of iron oxides under lipid monolayers

Steffen Bieder*,[a], D. C. Florian Wieland[a], Michael Paulus[a], Patrick Degen[b], Ralph Wagner[c], Heinz Rehage[b], and Metin Tolan[a]

[a] *Fakultät Physik/DELTA, TU Dortmund, Maria-Goeppert-Mayer-Str. 2, D-44227 Dortmund, Germany*

[b] *Fakultät Chemie, TU Dortmund, Otto-Hahn-Strae 6, D-44227 Dortmund, Germany*

[c] *Faculty of Physics, Bergische Universität Wuppertal, Gaußstr. 20, 42097 Wuppertal, Germany*

*email: steffen.bieder@tu-dortmund.de

Introduction

Nature forms inorganic structures in living organisms for different purposes like protection or modeling. Thereby structures are formed exhibiting material properties regarding to weight and stability which exceed known synthetic materials. Several studies report on the influence of additives and surfacants on the biomineralisation process showing a strong connection between the morphology of the formed structures and the used additives [1, 2, 3]. Aim of this work was to study the early stages of the biomineralisation process at liquid gas interfaces by x-ray diffraction and x-ray absorption spectroscopy. Therefore the mineralisation process was analyzed at the aqueous solution-air interface, whereby a biological membrane was mimicked by a Langmuir layer.

Experiments and Results

The sample systems consisted of aqueous iron(II)- and iron(III)chloride solution subphases with different concentrations and Langmuir layers of various phosphorlipids. The subphase was placed in a Langmuir trough. Stearic acid, stearylamine, 1,2-dipalmitoylphosphatidic acid (DPPA) and 1,2-dipalmitoyl-snglycero-3-phosphocholine (DPPC) were used as these lipids exhibit differently charged headgroups interacting with the positively charged iron ions. DPPA and stearic acid are positively charged, stearylamine is negatively charged and DPPC is bipolar. These Langmuir layers were compressed to surface pressures between 15 $\frac{mN}{m}$ and 40 $\frac{mN}{m}$. To induce the biomineralization process (the formation of iron oxide) gaseous ammonia was added to the gas phase above the sample system.

Grazing incidence diffraction (GID) measurements were carried out at beamline BL9 of DELTA using an incident photon energy of 13 keV and a MAR345 image plate in order to analyse the crystalline structure of the forming films. Due to the liquid sample system the x-ray beam had to be bend down on the sample's surface by a silicon mirror resulting in an incident angle of $\alpha = 0.076°$. Extended x-ray absorption fine structure (EXAFS) measurements of the Fe K absorption edge were performed at beamline BL8 of DELTA. The harmonic rejection mirror M3 was used to bend the beam down to an incident angle of 0.1°. The reflected signal was measured by an ionisation chamber behind the sample system.

Figure 1(a) shows a MAR-image of a 12 mM iron(II)chloride solution with a DPPC Langmuir layer. The layer

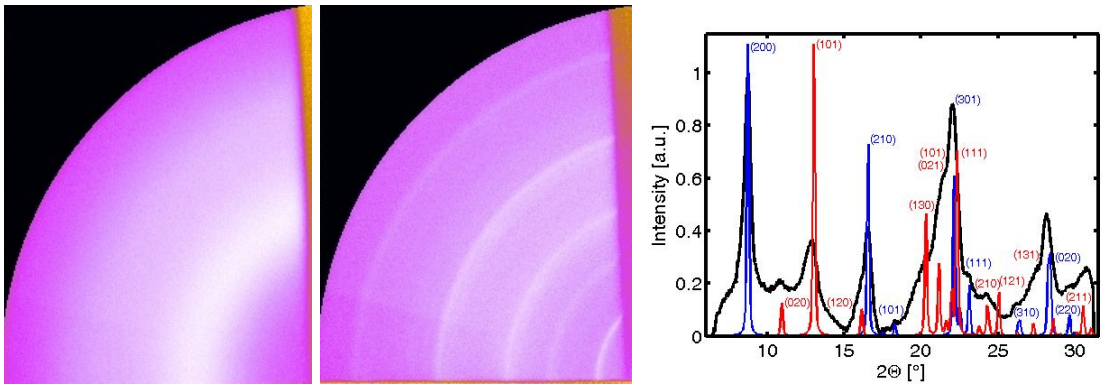

(a) (b) (c)

Fig. 1: (a) Diffracton pattern of an iron(II)chloride solution with a DPPC Langmuir layer after application of gaseous ammonia (b). Figure (c) shows the integrated spectrum of (b) (black) compared with the theory spectra of lepidocrocite (blue) and goethite (red).

was compressed to a surface pressure of 40 $\frac{mN}{m}$. The structure peak of water can be observed. After application

of gaseous ammonia the MAR-image shown in figure 1(b) was measured. Here, Bragg reflections originating from growing crystals become visible. In figure 1(c) the integrated spectrum is plotted along with theory spectra of different FeOOH formations, lepidocrocite (blue) and goethite (red), which match the observed scattering signal. Other structures like magnetite or meghemite did not match the data. This measurement was also performed without Langmuir layer. In this case only lepidocrocite was formed. This indicates that the Langmuir layer causes the formation of goethite. MAR-images measured at sample systems with iron(III)chloride did not show any Bragg refexions.
During the EXAFS measurements the same sample systems were studied at lower iron chloride concentrations. In contrast to the GID measurements, using iron(III)chloride the EXAFS measurements show the formation of small iron oxide clusters. Figure 2(a) shows an EXAFS spectrum of a 2 millimolar iron(III)chloride solution with DPPA Langmuir layer after the application of ammonia. The surface pressure of the layer was 15 $\frac{mN}{m}$. The fourier transform χ(R) of the data is shown in figure 2(b). It was calculated with the program ATHENA. A

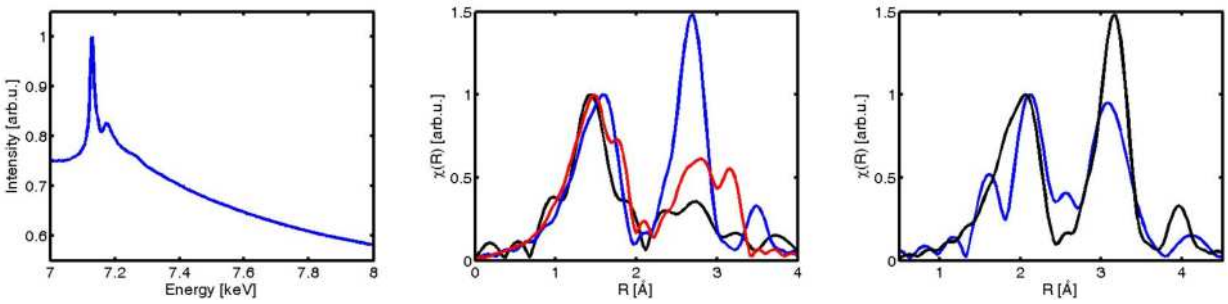

(a) (b) (c)

Fig. 2: (a) EXAFS spectra of an iron(III)chloride solution with a DPPA Langmuir layer. The spectra were taken after the application of ammonia. For a better overview the spectra are shifted in intensity. (b) shows the fourier transform χ(R) of the spectrum of (a) (black) compared to the theory spectra of lepidocrocite (blue) and goethite (red). (c) shows the fourier transform χ(R) of an iron(II)chloride solution with a DPPC langmuir layer (blue) compared to the theory spectrum of lepidocrocite.

comparison of the obtained χ(R) with several theory spectra indicates rather a match with goethite (red) than with lepidocrocite (blue). The χ(R) of a spectrum taken from a iron(II)chloride solution with a DPPC layer is shown in figure 2(c). In contrast to the previous spectrum this data shows a good match to the spectrum of lepidocrocite (black).

Conclusion

GID and EXAFS show an agglomeration of iron oxide at the samples surface. The subphase containing iron(II) ions shows the formation of crystaline iron under the monolayer yielding Bragg reflections. The GID patterns show the formation of goethite. In comparison to the measurements performed at the free interface where only lepidocrocite is formed, DPPC seems to favour the crystallisation of goethite. The measurements on subphases of iron(III)chloride show the formation of extreme small clusters at the interface which do not cause Bragg reflections.
Further informations and results of this experiment can be found in [4].

The authors want to thank the DELTA for providing synchrotron radiation.

References

[1] F. F. Amos, D. M. Sharbaugh, D. R. Talham, *Langmuir*, 24(4):1988-1994 (2007)

[2] X. R. Xu, J. T. Han, K. Cho, *Chemistry of Materials*, 16(9):1740-1746 (2004)

[3] F. C. Meldrum, *Int. Materials Review* , 48(3):187-224 (2003)

[4] Diploma Thesis Steffen Bieder, "Formation von Eisenoxid an der Wasser-Luft Grenzfläche", TU Dortmund, 2010

Templated Self Assembly of Magnetic Nanoparticles

D. Mishra,[1] M.J. Benitez,[1,2] P. Szary,[1] G.A. Badini Confalonieri,[1]
M. Feyen,[2] A. Lu,[2] O. Petracic,[1] and H. Zabel[1]

1 Institut für Experimentalphysik / Festkörperphysik, Ruhr-Universität Bochum, 44780 Bochum, Germany.
2 Max-Planck-Institut für Kohlenforschung, 45470 Mülheim an der Ruhr, Germany.

Magnetic nanoparticles have been the focus of research for its numerous application possibilities in data storage [1], spintronics devices, [2] and biomedical applications [3]. Particularly, assisted or templated self assembly of these nanoparticles is desirable for minimizing the disclinations or defects which form during the self-assembly on extended substrates [4].
We show here the electron density profile variation in the templated self-assembly of iron oxide nanoparticles investigated in the framework of reflection gratings. The details about sample preparation and magnetic properties can be found in ref 5. Fig 1 (a) and (b) show SEM images of lithographically fabricated trenches of 500 nm and 130 nm width, respectively, which are filled with iron oxide nanoparticles. The narrower the width of the trenches, the lower is the defect density due to confinement.

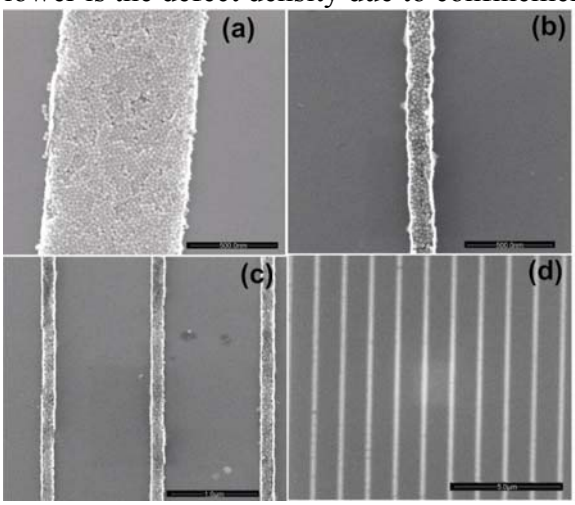

Fig 1: SEM images of trenches of width (a) 500 nm (b) 130 nm. Trenches of 130 nm width (c) filled (d) empty respectively.
We investigated the trenches of widths 130 nm with a period of 1.2 μm filled with nanoparticles and without nanoparticles (empty trenches) to determine the filling factor via x-ray structure factor analysis. Transverse scans were performed at BL9 of DELTA at energy of 13 keV at different ω values. Fig 2 (a) and (b) show the transverse (rocking) scans from filled trenches at $2\omega = 0.8°$ and 0.7° respectively. From the scans we observe satellite peaks around the specular peak due to interference of the reflected beam from the periodic structure. The periodicity corresponds to 1.2μm, which matches well with the SEM observation. In addition, we also observe variations of the normalized intensity of the satellite peaks which follow an intensity variation according to the diffraction from a

single slit. This feature is more pronounced in Fig 2 (c) and (d) where a comparison of the scans from filled and empty trenches is shown. The trenches are fabricated on Si substrates. Therefore, the electron density of the trenches is similar to that of the substrate. When the trenches are filled with iron oxide nanoparticles a drastic change in electron density is expected within the trenches. This could probably lead to an intensity variation in the interference pattern of the filled trenches. However, it is very difficult to obtain the filling factor from transverse scans alone.

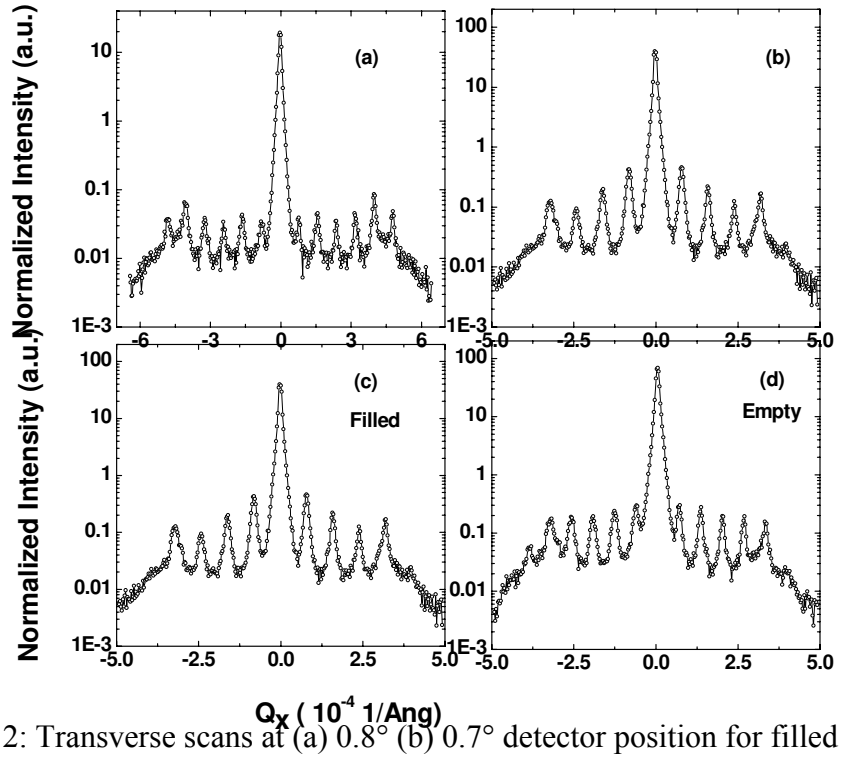

Fig 2: Transverse scans at (a) 0.8° (b) 0.7° detector position for filled trenches. Transverse scan at 0.7° for (c) filled and (d) empty trenches.

We were able to observe qualitatively the intensity variation from a filled and empty trench. Further efforts are in progress to analyze the reflectivity from the two systems together with the transverse scans to calculate the filling factor of the nanoparticles.

References

[1] Sun S C, Murray C B, Weller D, Folks L and Moser A 2000 *Science* **287** 1989.

[2] Kim T H , Jang E Y, Lee N J, Choi D J, Lee K J, Jang J T, Choi J S, Moon S H, Cheon J 2009 *Nano Lett.* **9** 2229.

[3] Jeong U, Teng X, Wang Y, Yang H and Xia Y 2007 *Adv. Mater.* **19** 33.

[4] Terris B D and Thomson T 2005 *J. Phys. D: Appl. Phys.* **38** R199.

[5] Benitez M J ,Sazry P, Mishra D, Feyen M, Lu A H, Petracic O, Zabel H, J. Supercond. Nov. Magn., submitted (arXiv:1010.4166).

X-ray diffraction study of the phase transition of $[Zn_2(BME\text{-}bdc)_2(dabco)]_n$ induced by absorption of CO_2

D.C. Florian Wieland,** Sebastian Henke,* Mikhail Meilikhov,* Kirill Yusenko,*Michael Paulus**; Metin Tolan** and Roland A. Fischer*

* Lehrstuhl für Anorganische Chemie II, Ruhr-Universität Bochum, Universitätsstr. 150 44801 Bochum

** Experimentelle Physik I, Technische Universität Dortmund, Otto-Hahn-Strasse 4 44221 Dortmund

Metal organic frameworks (MOFs) are composite materials, which are highly flexible and can be modified on a molecular level. One major advantage of this type of structures is their high porosity and tunable coordination space. These properties make MOFs interesting for applications in gas storage and sensing or for usage in membranes. The crystalline materials consist of inorganic clusters, which are joined by organic junctions. This hierarchic architecture allows the modification of MOF structures by changing the inorganic clusters or by modification of the organic linkers. Thereby the properties of the materials can be tailored by changing organic side groups of the linker without changing the overall topology.[1,2,3]

A unique property, which distinguishes certain MOFs from zeolites or other porous materials, is the ability to undergo pronounced framework dynamics in response to external stimuli, like temperature or pressure. The phase transitions can for example be induced by exchange of the adsorbed molecules. Therefore, such soft and dynamic frameworks announce huge potential for applications in highly selective chemical sensing and gas separation.[4]

In this work we have investigated the structural changes upon adsorption of CO_2 in the functionalized layer-based MOF $[Zn_2(BME\text{-}bdc)_2(dabco)]_n$ (**1**; BME-bdc = 2,5-bis(2-methoxyethoxy)-1,4-benzene dicarboxylate; dabco = diazabicyclo[2.2.2]octane). Isothermal gas adsorption measurements showed that **1** offers highly selective adsorption of CO_2 over N_2 and CH_4. Furthermore, the stepped CO_2 sorption isotherm indicated significant structural changes of **1** upon adsorption, see Figure 2. Powder X-ray diffraction measurements on solvent loaded and dried **1** also showed remarkable phase transition upon solvent sorption. Therefore, an analogue structure transition is expected upon CO_2 sorption.

In order to correlate the gas absorption experiments with the structural changes of **1** CO_2 pressure depended X-ray diffraction measurements were performed at beamline BL9. These experiments were performed at a temperature of 195 K, which made the use of a closed cycle cryostat necessary. The diffraction patterns were recorded using a two-dimensional MAR345 detector and a

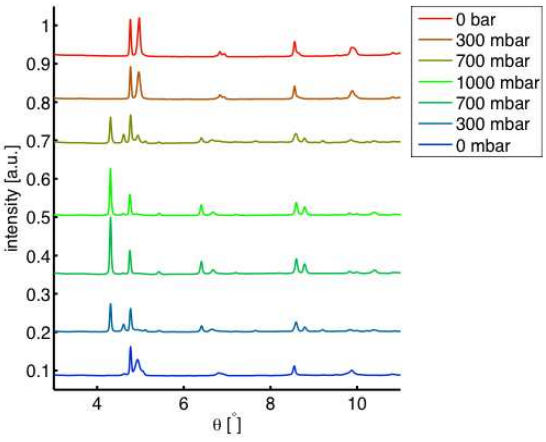

Figure 1: Diffraction patterns of **1** as a function of CO_2 pressure at 195 K

photon energy of 27 keV.[5] The low temperature was necessary to induce the structural transition of **1** at reasonable pressures. The high-pressure phase has a bigger cell volume than the low-pressure phase. Without the presence of CO_2 guest the pores are collapsed. By offering CO_2 the pores open in order to generate more space for the adsorption of CO_2 molecules. A selection of the obtained diffraction patterns is shown in Figure 1. The phase transition starts at CO_2 pressures higher than 300 mbar. After the MOF has completely transformed to the open pore structure at the saturation pressure of 1 bar the pressure was decreased again. Thereby **1** returns to the closed pore structure indicating desorption of CO_2 until the pressure drops to 0 mbar. The diffraction patterns show that the transformation is not completely reversible in these measurements. Some CO_2 remains in the pores. The remaining CO_2 can be removed by heating the sample to room temperature. We suggest, that the irreversibility of the transition observed in this measurement is due to kinetic effects. The adsorption/desorption of CO_2 in **1** is a slow process. In the time frame of the synchrotron experiments it was not possible to achieve the complete desorption of CO_2 at 195 K. Nevertheless, the isothermal sorption studies indicate the full reversibility of the CO_2 sorption (Figure 2). Notably, a minor contribution of a third metastable state could be observed in the diffraction experiments. Detailed analysis of this phase is in progress.

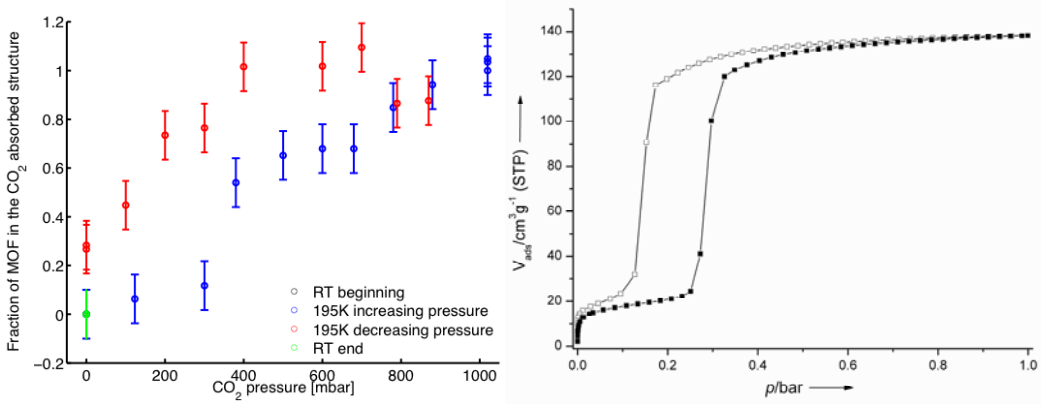

Figure 2: Fraction of **1**, which is in the open pore form as function of CO_2 pressure (left) and CO_2 sorption isotherm recorded on **1** at 195 K (right). Adsorption and desorption branches are shown with closed and open symbols, respectively.

In order to obtain the adsorption isotherm from the diffraction measurements a linear combination of the pattern of **1** in the closed pore state and of the pattern of **1** in the open pore state was fitted to the data. Figure 2 shows the fitted fraction of the open pore state as function of the CO_2 pressure in comparison to the CO_2 sorption isotherm. The data shows a hysteresis of the adsorption sequence. This effect is also observed in the CO_2 sorption measurement.

[1] M. O'Keeffe, M. Eddaoudi, H. Li, T. Reineke, and O.M. Yaghi *J. of Sol. St. Chem.***152**, 3 (2000)
[2] O. Shekhah, H. Wang, S. Kowarik, F. Schreiber, M. Paulus, M. Tolan, C. Sternemann, F. Evers, D. Zacher, R.A. Fischer, and C. Wöll, *J. Am. Chem. Soc.* **131**, 15118 (2007).
[3] S. Hermes, F. Schröder, R. Chelmowski, C. Wöll, and R.A. Fischer, *J. Am. Chem. Soc.* **127** , 13744 (2005).
[4] P. Llewellyn, G. Maurin, T. Devic, S. Loera-Serna, N. Rosenbach, C. Serre, S. Bourrelly, P. Horcajada, Y. Filinchuk, and G. Ferey, *J. Am. Chem. Soc.* **130**, 12808 (2008).
[5] K. Yusenko, M. Meilikhov, D. Zacher, F. Wieland, C. Sternemann, X. Stammer, T. Ladnorg, C. Wöll, R.A. Fischer, *Cry. Eng. Com.* **12**, 2086 (2010)
[5] C. Krywka, C. Sternemann, M. Paulus,N. Javid, R. Winter, A. Al-Sawalmih, S. Yi, D. Raabe, and M. Tolan, J. Synchrotron Rad. **14**, 244 (2007).

Zwischenbericht für die NRW Forschungsschule „Forschung mit Synchrotronstrahlung in den Nano-und Biowissenschaften“

Hydrolysis of Ti-containing alkoxides: Preparation, characterization and stabilization of TiO_2-nanoparticles

Stefanie J. Pfleiderer

Fachbereich C-Physik, Bergische Universität Wuppertal, Gaußstr. 20, 42079 Wuppertal, Germany

I. Motivation of the topic

Titanium dioxide (TiO_2) nanoparticles are interesting for a wide field of applications like solar radiation protection [1], as electrode material of lithium ion batteries and as a catalyst [2].
Especially for the last of the named applications, some demands have to be made to the materials structure, namely for example a high degree of crystallinity, small crystalline particles, a high porosity to achieve a high surface of the catalyst and a large amount of the anatase phase [2]. Anatase is one of the three common crystalline phases of TiO_2; the other two are brookite and rutile.
For the synthesis of porous, nanocrystalline TiO_2 materials, the sol-gel process is an often used method. In this process, a liquid, organometallic or alkoxide precursor is hydrolysed and the powder, which forms after a polycondensation step can be dried and annealed to achieve crystallisation. In most cases, a metal alkoxide is used as precursor. In this work titanium isopropoxide ($Ti(OC_3H_7)_4$) and zirconium n-propoxide ($Zr(OC_3H_7)_4$) are hydrolysed for the preparation of porous nanopowders. The reactions the powders are synthesized which work in the same way for titanium and zirconium. A general reaction scheme for the case of a titan alkoxide can be given as

$$Ti(OR)_4 + 4\ H_2O \rightarrow Ti(OH)_4 + 4\ ROH \qquad \text{(Hydrolysis)}$$
$$Ti(OH)_4 \rightarrow TiO_2 + 2\ H_2O \qquad \text{(Polycondensation).}$$

If alkoxide and reaction conditions are chosen properly, stable suspensions of particles in the remaining water-alcohol solution can be prepared. Substrates can be dipped in this suspension to prepare thin metal oxide films, which is an advantage of the sol-gel method [3].
However, there are some problems with respect to the requirements stated above: It is very difficult to prepare samples which combine all the stated characteristics. For example, if the anatase phase is the only crystalline phase detected in the prepared and annealed material, than the overall amount of amorphous contributions is still largely dominating. Synthesis pathways which lead to larger amounts of crystalline phases show the strong tendency to form the undesired brookite and rutile structures in addition to the anatase.

A possible way to influence the structure of the reaction product is to change the pH value of the reaction environment [2]. Hydrolysis and condensation in alkaline media are known to provide anatase in the crystalline parts of the sample, but also yield a large amount of amorphous phase [4]. Furthermore, the particle size increases with increasing pH value [5]. But in most cases, only TiO_2 nanoparticles synthesized with sodium hydroxide (NaOH) are studied, in some cases potassium hydroxide (KOH). A comparison between the crystallisation

behaviour of TiO_2 nanopowders synthesized in different alkaline reaction media is reported up to now. In some works, a comparison between the effects of different acids is made. Isley and Penn compared TiO_2 nanoparticles synthesized in nitric acid, hydrochloric acid and sodium hydroxide [6]. They found, as already mentioned, that the powders prepared in sodium hydroxide had large amorphous contributions. But the powder prepared with hydrochloric acid showed the same tendency to large amorphous fractions. In contrast, the powder prepared with nitric acid did not show that tendency. So in general, the use of acids as catalysts does not necessarily lead to large crystalline fractions in the synthesized oxide powders. This allows assuming that there may be alkalines which may lead to high crystalline concentrations and provide the advantage of resulting in high anatase contents. One mayor idea of this work is to prepare particles in different alkalines and to analyse and compare them with respect to the crystalline composition of the annealed TiO_2 powders, their crystalline and amorphous fractions and an assessment of their lattice defects. It is important that TiO_2 nanoparticles used in photooxidation processes should only have a small number of lattice defects, because electron-hole pairs may concentrate and recombine at those defects [7]. To prepare thin films by dip-coating, suspensions of the TiO_2 particles in a volatile solvent have to be synthesized. In literature, the dried powders are often ultrasonicated in a solvent [8]. Suspensions may also be prepared by ultrasonication treatment during the chemical reaction. Possibilities of structural changes are investigated here for the first time.
Another possibility to get preferably large amounts of anatase in the annealed sol-gel synthesized powders is to stabilize the anatase phase in a ZrO_2 network [9]. Sol-gel processes easily allow mixing titanium- and zirconium alkoxides and a hydrolysis of the mixture. There are two possible ways for the growth of the oxide nanoparticles: The first is the addition of molecules of the amorphous phase to the surface of small particles build during the initial condensation phase, the second is the coalescence of smaller particles to larger ones [10]. If the amorphous TiO_2 powders are embedded in ZrO_2, merging of small particles may be avoided. In addition, an interesting advantage of the TiO_2/ZrO_2 nanomaterials is an augmented catalytic activity [11].
Thus two different ways to prepare samples with pure or nearly pure anatase crystalline phase will be studied here: The first one is of chemical nature and consists of using alkalines as polymerisation catalyst; the second one is of physical nature and here a ZrO_2 network is employed to impede the coalescence of the formed TiO_2 particles.

II. Experiments

a) TiO_2 synthesized in alkaline reaction media

First examinations are made with 1M sodium hydroxide (NaOH) and potassium hydroxide (KOH). For the preparation of the amorphous powders, 2 ml of the alkaline solution are dropped into 5 ml of $Ti(OC_3H_7)_4$. The resulting powders are dried between two filter papers overnight. Annealing is carried out in an industrial furnace at 350°C, 400 °C, 450 °C and 500°C for four hours. A second set of samples was prepared in the same way under ultrasonication for about two or three minutes.
To determine the size of the crystalline particles, the broadening of x-ray diffraction (XRD) peaks are evaluated by using the Scherrer formula. From XRD it is also possible to make first conclusions about the formed crystalline phases.
The amounts of the amorphous phase are determined by linear combination fits of x-ray absorption near edge structure (LC-XANES). The structure of the region near the x-ray absorption edge (i.e. the position and the intensity of pre-and post edge peaks) is dependent on the local structure of the material around the x-ray absorbing atom. So the XANES structure of a material is a superposition of the structures included. The contributions of the

different structures can be derived from fitting with the spectra of the pure phases. As amorphous reference samples, the as prepared powders with the same preparation path are taken. Those samples do not show any sharp x-ray diffraction peaks.
From the region far behind the x-ray absorption edge (starting about 50 eV above the edge) the distances of the metal atoms and the oxygen neighbours can be determined. Also the coordination numbers of the metal atoms can be examined. From this data, it should be possible to make conclusions about lattice defects in the samples.

b) TiO_2/ZrO_2 nanomaterials

The composite samples are prepared in different ratios of TiO_2/ZrO_2, but with a constant ratio of water to alkoxide, because the water to alkoxide ratio is another factor which influences the hydrolysis reaction and should no overlap with the effect of the different metal oxide composition [8]. The water to alkoxide ratio is set to 40 mmol alkoxide to 160 mmol water. The ratios of TiO_2/ZrO_2 are set to 1:2, 1:1, 2:1, and 10:1. In addition, pure TiO_2 and ZrO_2 powders were prepared to compare them to the compound samples. These two pure samples are synthesized under the same conditions as the composites. The powders are annealed at 350°C, 400°C, 450°C and 500°C subsequently and analysed with XRD, XPS and x-ray absorption experiments.

III. Results and discussion

3.1. X-ray diffraction experiments

3.1.1. Preparation in alkaline reaction environment and effect of ultrasonication

The samples were investigated with XRD after they were annealed at the temperatures stated above. It can be seen from the diffraction patterns, that the crystalline fractions in the samples only consist of anatase. The particle sizes of the ultrasonicated samples are larger than those without ultrasonic treatment (see Fig.1 b)). So from this point of view, ultrasonication leads to powders with undesired properties. In both cases, the particle sizes increases with increasing annealing temperature, however the increase is smaller for the ultrasonicated samples.

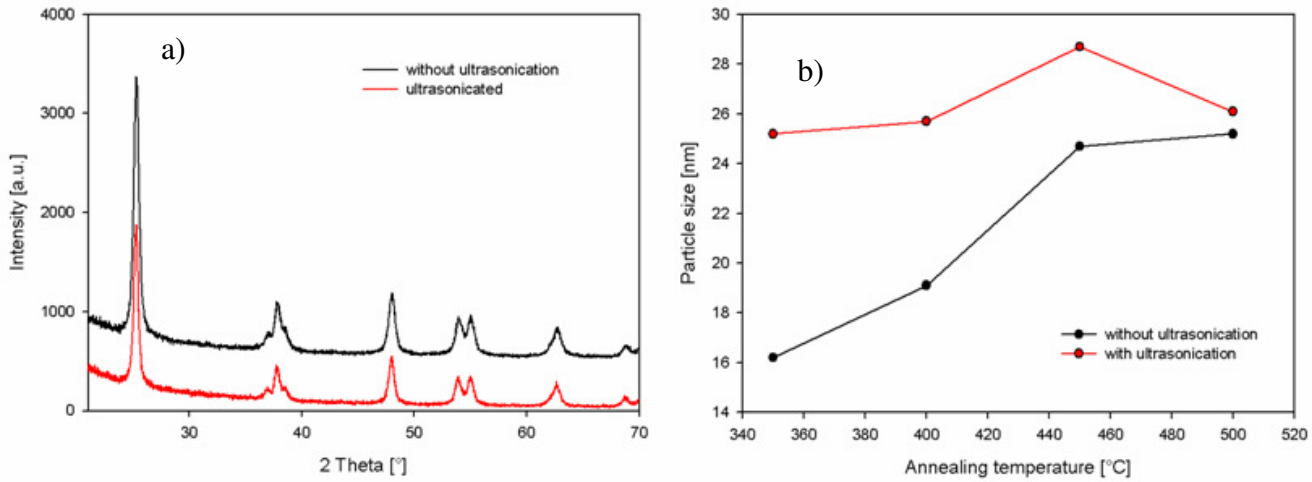

Fig. 1: a) Diffraction patterns of TiO_2 powders synthesized with 1 M NaOH and annealed at 450°C for four hours. b) Development of the particle size with increasing annealing temperature in samples synthesized with 1M KOH. The trend of higher particle sizes in the ultrasonicated samples is also visible in the case of samples prepared with 1M NaOH.

3.1.2. TiO_2/ZrO_2 composite samples

In the diffraction patterns of the composite samples, it can be seen that only in the case of pure TiO_2 samples and the samples with TiO_2:ZrO_2=10:1 anatase peaks are observable. The other samples are not crystallized during annealing, even after calcination at 500°C (Fig. 2(a)). It could be speculated that the crystallites which may have developed during the annealing are too small to be observable in XRD. As will be seen later from LC-XANES fits, however, this is not true and large amounts of the sample really stay amorphous after the calcination. So if the content of ZrO_2 is chosen to large, crystallisation is impeded and so it is not helpful to choose large amounts of ZrO_2. The development of the particle size in the two crystallised powders are shown in Fig. 2 b) for pure TiO_2 and TiO_2/ZrO_2=10:1.

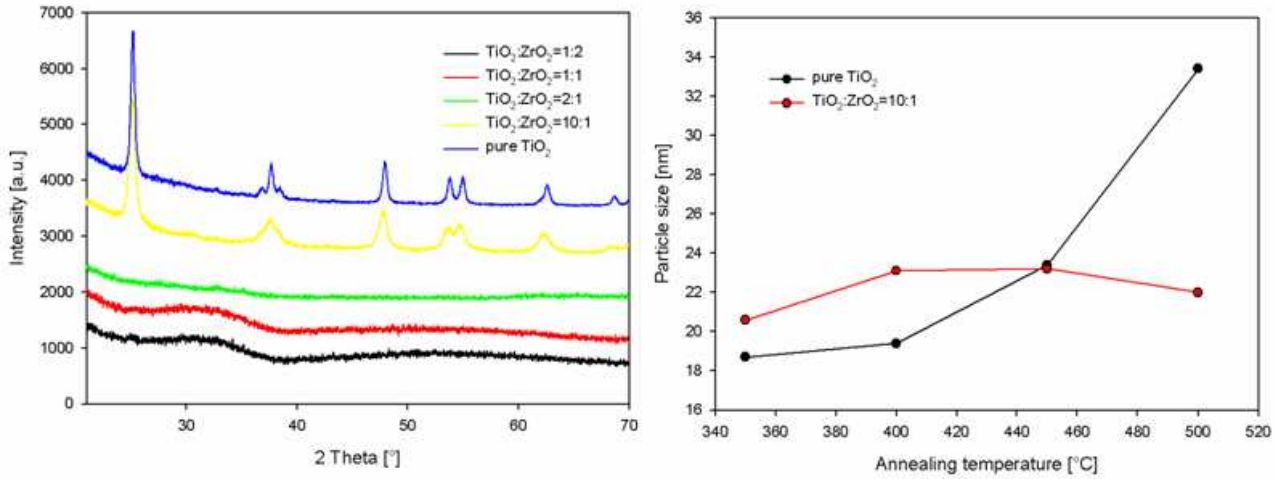

Fig. 2: a) Diffraction patterns of the composite samples after annealing at 500°C for four hours. b) Particle sizes in dependence of the annealing temperature for the two crystallised samples as determined from XRD analysis.

It is observed that the crystals in the pure TiO_2 samples increase in size with increasing annealing temperature. The crystals in the sample with added ZrO_2 stays nearly constant in contrast. This can be explained by the suppressed coalescence of small particles to larger ones, which is not given in the pure ZrO_2 sample. In an experiment made at beamline C at HASYLAB in October 2010, powders with the TiO_2:ZrO_2 ratios of 4:1, 6:1 and 8:1 were measured. They were annealed similar to those explained above. These data are not evaluated jet.

3.2. LC-XANES results

3.2.1. Composition of the powders prepared in alkaline reaction media

If samples prepared with and without ultrasonication are compared, it can be seen that the ultrasonication leads to higher amorphous concentrations (Fig. 3). This effect is observable in the powders synthesized with 1M NaOH and annealed at 350°C, 400°C, 450°C and 500°C. No significant difference in the amorphous concentration can be observed between the two alkalines investigated so far (i.e. KOH and NaOH).

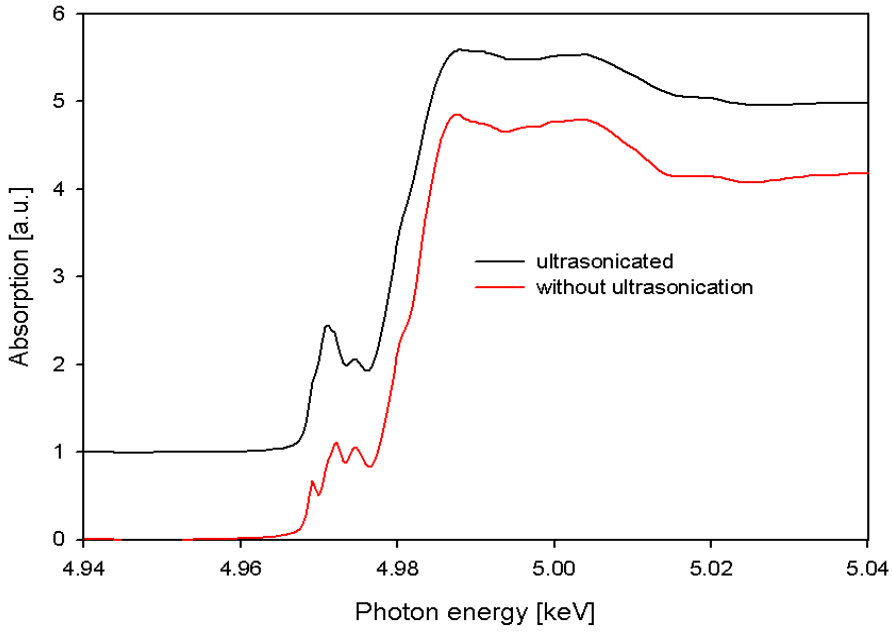

Fig. 3: Ti K-edge XANES spectra of the samples synthesized with 1M NaOH and calcined at 400°C for four hours. The red spectrum of the sample which was not ultrasonicated during synthesis shows more structure which belongs to the typical anatase absorption edge.

3.2.2. Composition of the samples with ZrO_2 addition

From the near edge spectra of the composite samples, it can be seen that all samples except of the ones explained above do not crystallize significantly. The amorphous concentration of the composite samples as determined by LC-XANES analysis is shown in Fig. 4 in dependence on the annealing temperature.

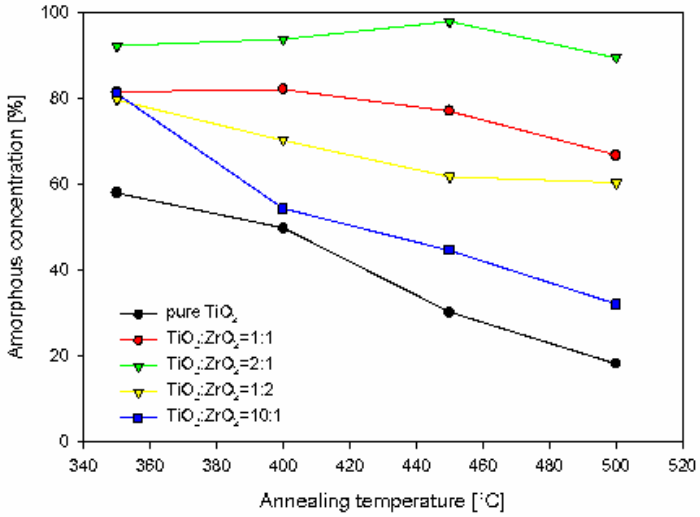

Fig. 4: The concentration of amorphous TiO_2 in samples with different ZrO_2 content in dependence on the annealing temperature. The significantly decreasing amorphous phase matches to the XRD data which showed obvious diffraction peaks in contrast to the other samples.

As could be concluded from the already discussed x-ray diffraction patterns, the pure TiO_2 samples and the samples with TiO_2:ZrO_2=10:1 show a significant decrease of the amorphous phase with increasing annealing temperature. In the other samples, the amount of amorphous phase decreases slowly or stays nearly constant.

3.3. EXAFS results

3.3.1. Atomic binding length in the powders synthesized in alkaline reaction media

EXAFS data is fitted with a very simple model consisting of two scattering paths, which are an anatase structure scattering path and a brookite structure scattering path. Only the first shell is fitted, the q-space was taken as the fitting space (Fig. 5 b)). One of the problems related to the used model is that it does not account for amorphous contents in the powders. It is difficult to embed such amorphous materials to the model because the calculation of the scattering paths is only accomplishable for clusters of a certain size. Thus, when the fit results of the EXAFS data are interpreted, a possible influence of the amorphous contributions should always be kept in mind.
For the ultrasonicated samples prepared in 1M KOH, the Ti-O binding length is constant with respect to the annealing temperature in anatase and brookite. In the samples synthesized with 1M KOH without ultrasonication the binding length slightly decreases with increasing annealing temperature. This might be due to the reduction of the particle surface area with increasing particle size. Less atoms are located at the surfaces of the particles and the atoms in the particle volume have a higher coordination and thus a stronger binding to the neighbouring oxygen atoms. In the binding length of the samples prepared with 1 M NaOH, such a trend is not observable.

3.3.2. Atomic binding in the composite powder samples

The atomic distances determined from the detailed fitting of the x-ray absorption data do not show a trend in dependence on the annealing temperature or the ZrO_2 content. The only obvious tendency is a decrease of the binding length for the samples with TiO_2:ZrO_2=2:1. Because of the simple fitting model, it can not be said if this is due to a special structural effect or an artefact of the data evaluation as indicated above.

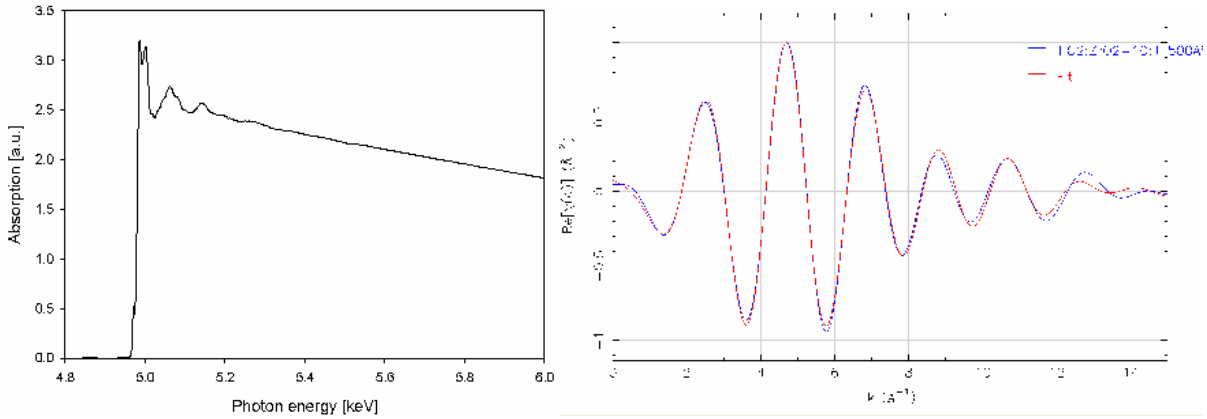

Fig. 5: a) The Ti K-EXAFS spectrum of the sample TiO_2:ZrO_2=10:1 annealed at 500°C. b) A fit of the data in the q space.

IV. Summary and conclusions

Both ways to synthesize TiO_2 nanoparticles lead to anatase crystalline phases, if crystallisation is observed. Between the two tested alkaline reaction media, no significant difference in the amount of amorphous contributions was observed, and the annealing

behaviour is similar, i.e. a reduction of the amorphous phases by 20-50% is observed. Our results suggest that an ultrasonication treatment during the reaction for the synthesis of oxide suspensions should be avoided as it leads to larger particles and higher amorphous concentrations. The anatase particle size of TiO_2-ZrO_2 composites is stabilised during the annealing procedure by the ZrO_2 network that is formed in the synthesis step. On the other hand, the increase of the crystalline fraction in the powder during the annealing step is smaller than in pure TiO_2 nanopowders. Up to now, there is no well defined lower limit for the amount of added ZrO_2 evident, that leads to stable TiO_2 anatase particles, but on the other hand, a high amount of added ZrO_2 impedes crystallisation even at high temperature annealing.
Different alkaline reaction media should be compared to check if alkaline reaction media can be used to achieve stable anatase TiO_2 nanoparticles and a satisfactory amount of crystalline phase. When the most suitable synthesis conditions are found, the size distribution of the particles should be investigated with small angle x-ray scattering (SAXS).

V. Program for the next two years

In the next year, two more alkaline solutions should be tested in connection to the crystallinity and particle size of the powders synthesized with these solutions. Composite samples with titanium dioxide to zirconium dioxide ratios of 4:1, 6:1 and 8:1 have already been prepared and X-ray measured have been performed. Those data will be evaluated to identify the conditions for which the crystallisation is able to start. Subsequently, the amount of ZrO_2 should be reduced to concentrations lower than in TiO_2:ZrO_2=10:1 to find the lowest possible concentration of ZrO_2 to prepare stable anatase TiO_2 nanoparticles. In addition, the best alkaline solution and the most suitable ratio of TiO_2 and ZrO_2 should be used to prepare samples at different water to alkoxide ratios for a further reduction of the particle size.
In the third year, some thin films should be prepared by dip- or spin-coating using the best preparation methods identified. The particle size distribution of the best samples should be determined with SAXS measurements to see if the found synthesis ways also provide desirable results in connection with this parameter. XPS measurements should be made to see in how far ions of the used alkalines are able to segregate through the powders and if annealing leads to destruction and segregation of the ZrO_2 network.

V. References

[1] A.P. Popov et al., J. Phys. D: Appl. Phys., 38, 2564-2570, 2005
[2] R.Rossmanith et al, Chem. Mater. 20, 5768-5780, 2008
[3] T. L. Hanley et al., J. Phys. Chem. B, 106, 1153-1160, 2002
[4] S.L. Isley, R.L. Penn, J. Phys. Chem. B, 110, 15134-15139, 2006
[5] [3] S. Mahshid, M. Askari, M. Sasani Ghamsari, J. Mater. Proc. Technol., 189, 296-300, 2007
[6] S.L. Isley, R. Lee Penn, J. Phys. Chem. B, 110, 15134-15139, 2006
[7] K.L. Yeung et al., J. Phys. Chem. B, 106, 4608-4616, 2002
[8] K. Sato et al., J. Am. Ceram. Soc., 91 [8], 2481-2487, 2008
[9] S.H. Elder et al., Chem. Mater., 10, 3140-3145, 1998
[10] R. Lee Penn, J.F. Banfield, Geochimica et Cosmochimica Acta, Vol. 63, No. 10, 1549-1557, 1999
[11] X. Fu et al., Environ. Sci. Technol., 30, 647-653, 1996.

Characterization of poly(organosiloxane) nanocapsules with iron oxide core by means of x-ray diffraction

Michael Paulus[1], Johannes Möller[1], Martin A. Schroer[1], Patrick Degen[2], Melek Cebi[2], Heinz Rehage[2], and Metin Tolan[1]
[1]Fakultät Physik/DELTA, TU Dortmund, Maria-Goeppert-Mayer-Str. 2, D-44227 Dortmund, Germany;
[2]Fakultät Chemie/ Physikalische Chemie II, TU Dortmund, Otto-Hahn-Str.6, D-44227 Dortmund, Germany

Because of their multifarious applicability in science and technology, interest in the properties of nanoparticles has grown in the last few years. They offer important applications in medicine, cosmetics, solar energy transformation, electronics, chemical catalysis and magnetic recording [1]. The controlled synthesis and manipulation of nanoparticles e.g. the production of nanocapsules for medical applications is important for the production of advanced materials.

In this work the structural characterization of nanocapsules containing magnetic cores of iron oxide by means of x-ray diffraction is reported. Such capsules can be used to produce new types of microreactors [2, 3, 4] or for the therapeutic delivery of drugs, genes or radionuclides [5]. However for this purpose the knowledge of the structural assembly of these capsules is essential for the development of reliable drug containers.

The synthesis of iron oxide cores took place in reverse micellar cavities dispersed in organic solution [6]. After core formation the weekly bounded organic shell around the nanoparticle was replaced by octadecyl-trichlorosilane (OTS). Due to the polymerization of the OTS shell a stable covalent Si-O bound capsule was formed [7].

The dried nanocapsules were investigated regarding to shell and core structure by x-ray diffraction at beamline BL9. A photon energy of 27 keV and an image plate (MAR345) was used. For comparison diffraction images of pure maghemite and magnetite nanoparticles as well as polymerized OTS were recorded. Figure 1 shows exemplarily diffraction spectra of magenetite (Fe_3O_4) nanoparticles, nanocapsules and the pure polysiloxane respectively as a function of the wave vector transfer q.

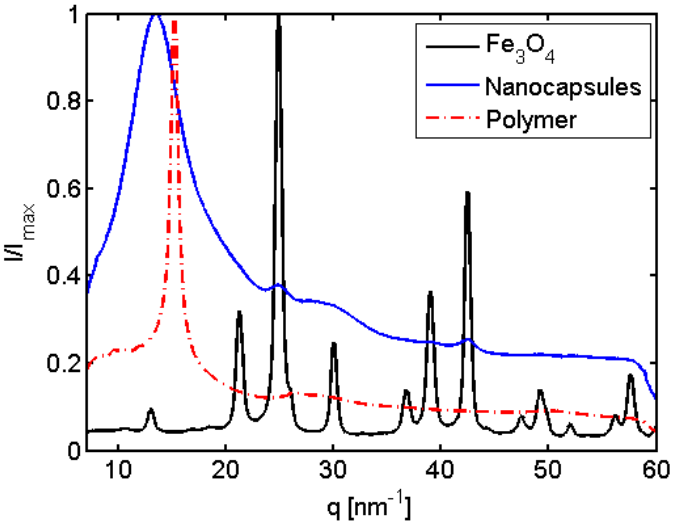

Figure 1: Diffraction spectra of nanocapsules, magnetite nanoparticles and polymerized OTS.

The nanocapsules offer only a week scattering signal due to Fe_3O_4 cores while the shell causes a strong first diffraction peak. In comparison to the pure polymer the shell signal is shifted to lower q which goes in hand with a strong broadening of the diffraction peak. Following Lucovsky [8] the peak position q_p and peak width Δq determine a correlation length and coherence length, respectively, of the investigated system. A fit to the first diffraction peak yields a correlation length for the polymer of $R_p = (4.15 \pm 0.05)$ Å which can be attributed to Si–O second nearest-neighbour bond length which was found for SiO_2 in previous works [8]. The coherence length was found to be $L_p = (60 \pm 10)$ Å which is a factor of 6 higher as expected for SiO_2 pointing to a large three dimensional polymer network. In comparison the nanocapsules exhibit a dilated network

with a correlation length of R_{nc} = (4.67 ± 0.05) Å while the coherence length is reduced to L_{nc} = (10 ± 1) Å reflecting the small size of the formed nanocapsules which have radii in the regime of several nanometers.

The authors like to acknowledge the DELTA machine group for providing synchrotron radiation and technical support.

[1] C.N.R. Rao, A. Müller, A.K. Cheetham (eds), *The chemistry of nanomaterials: synthesis, properties and application.* Wiley, Weinheim (2004).
[2] Y. Lvov, F. Caruso, Anal. Chem. **73**, 4212 (2001).
[3] Y. Lvov, A. Antipov, A. Mamedov, H. Möhwald, G.B. Sukhorukov, Nano Lett. **1**, 125 (2001).
[4] O.P. Tiourina, A.A. Antipov, G.B. Sukhorukov, N.L. Larionova, Y. Lvov, H. Möhwald, Macromol. Biosci.**1**, 209 (2001).
[5] Q.A. Pankhurst, J. Connolly, S.K. Jones, J. Dobson, J. Phys. D: Appl. Phys. **36**, 167 (2003).
[6] C. T. Seip, E. E Carpenter, C. J. O'Connor, IEEE Trans. Magn. **34**, 1111 (1998).
[7] P. Degen, A. Shukla, U. Boetcher, H. Rehage, Colloid Polym. Sci. **286**, 159 (2008).
[8] Lucovsky, G. ; Phillips, J. C., Physica Status Solidi B **246**,1805 (2009).

Structure determination of polyethylene gas pipes by means of x-ray diffraction

Saskia Schmacke*,[a], Michael Paulus[a], Christian Sternemann[a], Dirk Grahl[b], Thomas Theisen[b], Metin Tolan[a]

[a] *Fakultät Physik/DELTA, TU Dortmund, D-44221 Dortmund,*
[b] *RWE Vertrieb AG, Freistuhl 7, 44137 Dortmund.*

*email: Saskia.Schmacke@tu-dortmund.de

Polyethylene (PE) is a widely used material in many fields of daily life like automotive industry (wheels, interior), packing industry and building industry. The materials studied in this work are polyethylene gas pipes, which have been in use since the late seventies.

PE is a macromolecule, consisting of a long chain of ethene units. The examined PE gas pipes were made of PE63. The solid body is composed of crystalline and amorphous areas. In the crystalline parts the chains order in an orthorhombic unit cell (space group *Pnam*) with cell parameters a = 7.4241 Å, b = 4.9491 Å, and c = 2.5534 Å [1]. The polyethylene chains are oriented parallel to the c axis of the unit cell. In the amorphous regions the polyethylene molecules are randomly distributed. With increasing amorphous fraction the elasticity increases and the brittleness decreases [2]. Thus, the composition of crystalline and amorphous areas effects the macroscopic behaviour of the material.

The task is to obtain information about the structure of bulk PE at room temperature and its ageing behaviour by means of thermal and pressure treatment. The goal is to predict material failure. X-ray diffraction and small angle x-ray scattering are proper tools to analyse the crystalline and amorphous contributions within the samples and to establish a connection between molecular structure and macroscopic properties such as material stability.

The examined samples were prepared from 30-35 years old PE63 pipes, which have been used in the gas supply under street and pavement, respectively. They possess a diameter of 160 mm and a wall thickness of 9.1 mm. For sample preparation a 10 mm broad stripe was cut along the longitudinal axis out of the pipe. This stripe was divided in cuboids. Each of the cuboids was cut in four slices from the outer wall surface (slice 1) over two bulk slices (slices 2 and 3) and a fourth slice from the inner wall surface (slice 4). Each slice has a thickness of 1.5-2 mm.

The diffraction experiments were carried out at the wiggler beamline BL9 at DELTA [3]. Diffraction patterns were taken at a wavelength of $\lambda = 0.459$ Å using a MAR345 image plate scanner. The distance between the sample and the detector was 359 mm. The exposure time was 300 s for each of the three scans conducted for the particular sample slice. After the measurements the 2d data were radially integrated with the program Fit2D [4].

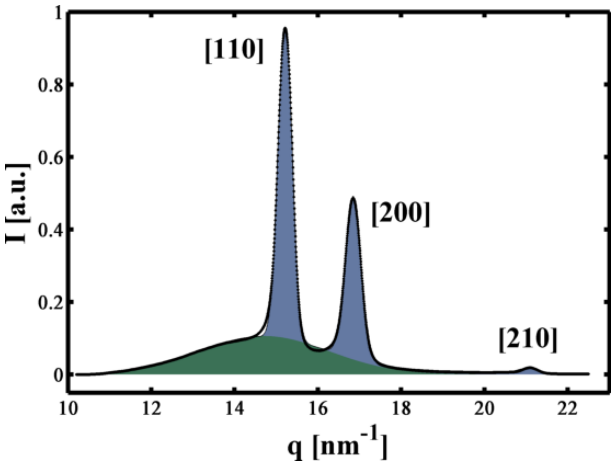

Fig. 1: Decomposition of a typical x-ray diffraction spectrum after background correction in crystalline (blue area) and amorphous (green) contributions for a semicrystalline PE sample.

Since the samples are neither completely amorphous nor completely crystalline, scattering experiments yield both crystal reflections and a broad amorphous scattering halo. The region of the [110] and [200] reflections as well as the strong amorphous scattering halo have been used for the analysis of the sample's crystallinity. Pseudo Voigt profiles are selected as profile functions for the crystalline reflections and a Gaussian profile function in the case of the amorphous contribution. This functions are fitted to the background corrected data set. The positions of the Bragg reflections yield the unit cell parameters. Integration of the amorphous scattering contribution (integrated intensity I_{am}) as well as contribution of the [110] and [200] reflection (integrated intensity I_{cryst} of both reflections) and calculation of the ratio of both yields the relative crystallinity χ of the sample:

$$\chi = \frac{I_{cryst}}{I_{cryst} + I_{am}}.$$

Fig. 1 shows a typical diffraction pattern for a PE sample after background correction. The sample's crystallinity is obtained by profile fitting and integration of the crystalline and amorphous contributions of the scattering signal.

Crystallinities have been determined for 3 gas pipes utilised under streets and 4 gas pipes, that have been used under pavements. The left hand data of Fig. 2 show the crystallinities deduced from scattering signals originating from street samples as a function of the sample slice. An almost perfect agreement in the trend with

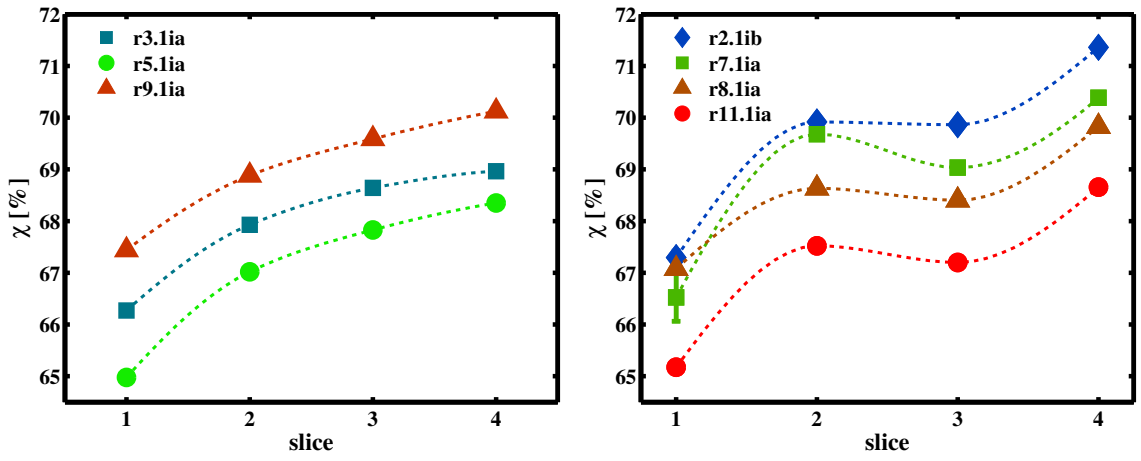

(a) (b)

Fig. 2: Relative crystallinities of (a) street and (b) pavement sample cuboids as a function of the sample slice. Dashed lines serve as guide lines for the eye and are shape-preserving interpolating data curves.

lowest amounts of crystalline material at the outer surface and steadily increasing crystallinity within the bulk and highest accumulation of crystallites at the inner surface can be seen. The crystallinity values of the three different samples are very similar in the slope of the curves, but differ in the absolute value of crystallinity. The amount of crystalline material is about 3 % higher than at the inner surface.

Correspondingly, the crystallinities of the pavement pipes are depicted in Fig. 2(b). Here the slope of the crystallinity curve is different. The crystallinities of the pipe samples r2.1ib, r7.1ia, r8.1ia, and r11.1ia show the lowest crystallinity at the outer surface, followed by a rather strong increase of crystalline material in the transition to the first bulk slice. Afterwards, the crystallinity is rather constant, while the crystallinity is strongly decreasing in transition to inner surface and the change of crystallinity is about 3.5 %.

Thus, all pipes show the highest crystallinity at the inner wall surface. Results of internal pressure creeping tests and DSC measurements [5] did show that these are the sample spots where material failure occurs. By comparing crystallinities of street and pavement pipes it becomes clear, that the biggest difference consists in the development of crystalline material over the cross section of the pipe wall between outer and inner surface. While both types of pipes show a gradient of χ with lowest crystallinity at the outer surface and highest accumulation of crystalline material at the inner surface, street pipe crystallinities exhibit a steadily increasing amount of crystalline material. In contrast, pavement pipes possess a constant crystallinity within the bulk.

The authors want to thank *RWE AG* for financial support of the work and the DELTA institute for beamtime.

References

[1] R. Caminiti, L. Pandolfi, and P. Ballirano, *J. Macromol. Sci – Phys.*, „Structure of Polyethylene from X-Ray Powder Diffraction: Influence of the Amorphous Fraction on Data Analysis", B39(4), 481 – 492 (2000)

[2] H. Gräfen, „Lexikon der Werkstofftechnik", VDI-Verlag Düsseldorf, 779 – 785 (1993)

[3] C. Krywka, C. Sternemann, M. Paulus, N. Javid, R. Winter, A. Al-Sawalmih, S. Yi, D. Raabe, and M. Tolan, *J. Synchrotron Rad.*, **14**, 244 (2007).

[4] http://www.esrf.eu/computing/scientific/FIT2D.

[5] Private communications. Meeting with D. Grahl of RWE and A. Regeling, M. Stranz, and M. Paaßen of egeplast Werner Strumann GmbH & Co. KG, Greven.

Characterization of poly(organosiloxane) nanocapsules with iron oxide core by SAXS

Johannes Möller*,[a], Martin A. Schroer[a], Patrick Degen[b], Melek Cebi[b], Michael Paulus[a], Christoph J. Sahle[a], Alexander Nyrow[a], Heinz Rehage[b] and Metin Tolan[a]

[a] *Fakultät Physik/DELTA, TU Dortmund, Maria-Goeppert-Mayer-Str. 2, D-44227 Dortmund, Germany;*
[b] *Fakultät Chemie/ Physikalische Chemie II, TU Dortmund, Otto-Hahn-Str.6 , D-44227 Dortmund, Germany*

*email: johannes.moeller@tu-dortmund.de

In this report we describe recent results of our small angle x-ray scattering (SAXS) experiments to study the internal structure and the formation process of poly(organosiloxane) nanocapsules filled with an iron oxide core of different size.

Iron oxide nanoparticles offer different important applications in magnetic recording, solar energy transformation, electronics and chemical catalysis [1]. Concerning nanocapsules with solid cores most work has been focused on the synthesis of these materials. Very little attention has been directed towards the interaction between the shell and the core or to the modification of the core within the capsule [2]. The possibility of removing partially or completely the magnetic core of the capsule by chemical etching processes offers the opportunity of assembling hollow poly(organosiloxane) nanocapsules, which can be used to produce new types of microreactors [3, 4, 5] or for the therapeutic delivery of drugs, genes or radionuclides [6]. However for this purpose the knowledge of the structural assembly of these capsules is essential for the development of reliable drug containers. The synthesis approach of the nanoparticles has two essential features: (A) the synthesis of iron oxide nanoparticles induced by a chemical precipitation process in reverse micellar cavities [7]; (B) preparation of the thin poly(organosiloxane) shell around the aqueous ferrofluid droplet [8]. The organic shell around the droplet surface was formed through the hydrolysis and polycondensation of octadecyl-trichlorosilane (OTS) [9]. During the polymerization process the original stabilizing surfactant shell was replaced by the very thin coherent OTS-layer. Because of the release of HCl during the polymerization the magnetic core was dissolved as seen in a colour change of the samples. Due to the polymerization, the nanocapsules are extreme stable and can be purified by subsequent washing cycles with water without being damaged. The cleaned nanocapsules (with or without cores) can be dried in vacuum and redispersed in various organic liquids. While dynamic light scattering and UV-Vis measurements were already applied, there is a lack of information concerning the size and the structure of the iron oxide core inside the capsule. Here, small angle X-ray scattering experiments can give valuable information as this technique is excellently suited to probe colloidal particles of a size of several Angstroms up to a few nanometers in solution.

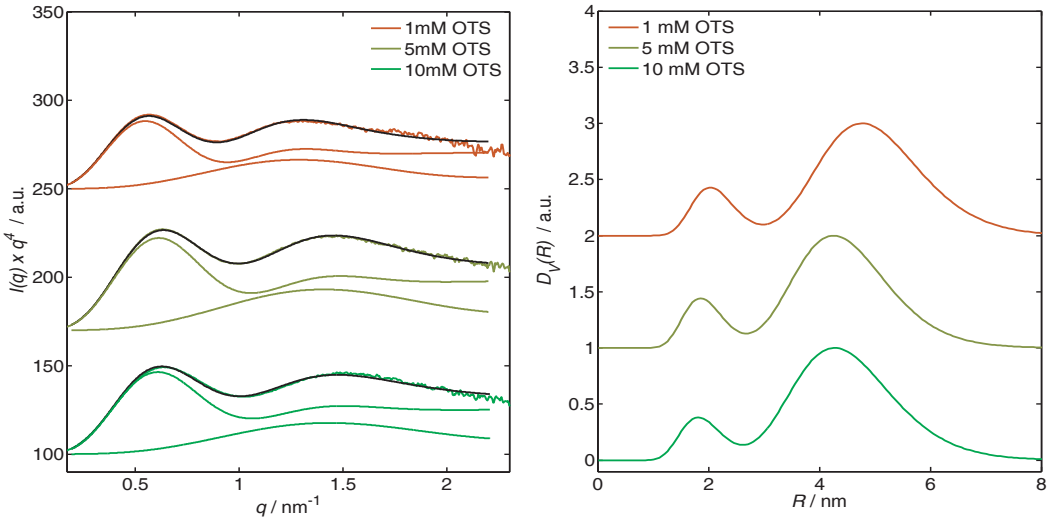

Figure 1: (a) Measured intensities in Porod plot with the refinement using a bimodal distribution function (black) and the contributions to the intensity from the unimodal fractions of the distribution (respective colour). (b) Resulting volume distribution function.

Measurements were performed at beamline BL9 of DELTA employing the SAXS setup already described in Ref. [10]. A photon energy of 10 keV and a sample-to-detector distance of about 1353 mm allowed to cover a

q-range from 0.1 up to 2.5 nm^{-1}. The exposure time was chosen to be 600 - 1800 s due to the low concentrations used. Low particle concentration were used to be able to determine the form factors without contributions of an intermolecular structure factor. As the solvent in which the nanocapsules are dissolved affects the glue typically used to fix the window materials of the usually used sample cells a special custom-built sample cell was constructed and employed [11].

In our study nanocapsules with different compositions of the educts forming the iron core were investigated as a function of the OTS concentration used in the synthesis process. Figure 1 shows the SAXS signal of the different particles in the so-called Porod plot, i.e. $I(q) \cdot q^4$, together with the refinement to the experimental data. Using a bimodul distribution function for the iron oxide core together with the form factor of sphere gave the best fitting results to the data. The corresponding distribution functions are also depicted.

As can be seen, for the lowest OTS concentration the distributions for all synthesis compositions are broad and nearly similar. Hence, the compositions has only a minor influence on the particles' shape at these conditions. Increasing the OTS concentrations results in a reducing of the mean particle size as well as in a tightening of the distribution due to the partial dissolving of the iron oxide core. Furthermore, this OTS dependency is different for the various compositions studied. These measurements were supplemented by additional SAXS studies performed at BW4, HASYLAB, as well as by anomalous SAXS (ASAXS) studies at B1, HASYLAB, respectively.

The authors like to acknowledge the DELTA machine group for providing synchrotron radiation and technical support.

References

[1] C.N.R. Rao, A. Müller, A.K. Cheetham (eds), *The chemistry of nanomaterials: synthesis, properties and application.* Wiley, Weinheim (2004).

[2] K. Kamata, Y. Lu, Y. Xia, *J. Am. Chem. Soc.* **125**, 2384 (2003).

[3] Y. Lvov, F. Caruso, *Anal. Chem.* **73**, 4212 (2001).

[4] Y. Lvov, A. Antipov, A. Mamedov, H. Möhwald, G.B. Sukhorukov, *Nano Lett.* **1**, 125 (2001).

[5] O.P. Tiourina, A.A. Antipov, G.B. Sukhorukov, N.L. Larionova, Y. Lvov, H. Möhwald, *Macromol. Biosci.* **1**, 209 (2001).

[6] Q.A. Pankhurst, J. Connolly, S.K. Jones, J. Dobson, *J. Phys. D: Appl. Phys.* **36**, 167 (2003).

[7] C. T. Seip, E. E Carpenter, C. J. O'Connor, *IEEE Trans. Magn.* **34**, 1111 (1998).

[8] P. Degen, A. Shukla, U. Boetcher, H. Rehage, *Colloid Polym. Sci.* **286**, 159 (2008).

[9] M. Husmann, H. Rehage, E. Dhenin, D. Barthes-Biesel, *J. Colloid Interface Sci.* **282**, 109(2005).

[10] C. Krywka, C. Sternemann, M. Paulus, N. Javid, R. Winter, A. Al-Sawalmih, S.B. Yi, D. Raabe, M. Tolan, *J. Synchrotron Rad.* **14**, 244 (2007).

[11] J. Möller, *Strukturelle Untersuchung von Eisenoxid-Nanopartikeln mittels Röntgenkleinwinkelstreuung*, diploma thesis, TU Dortmund (2010).

Exciton-mediated lattice distortions in InAs/GaAs quantum dots

Sebastian Tiemeyer*,[a], Michael Bombeck[b], Michael Paulus[a], Christian Sternemann[a], D. C. Florian Wieland[a], Manfred Bayer[b], and Metin Tolan[a]

[a] *Fakultät Physik/DELTA, TU Dortmund, Maria-Goeppert-Mayer-Str. 2, D-44227 Dortmund, Germany;*
[b] *Experimentelle Physik II, TU Dortmund, Otto-Hahn-Str. 4, D-44227 Dortmund, Germany.*

*email: sebastian.tiemeyer@tu-dortmund.de

Quantum dot heterostructures are a research topic offering both the discovery of principal knowledge in terms of quantum information processing [1] and the development of optoelectronic devices [2]. The confinement of charge carriers to length scales comparable to the de Broglie wavelength in semiconductor heterostructures such as quantum wells and quantum dots leads to a considerable modification of the density of states (DOS). In particular quantum dots represent zero-dimensional structures possessing a DOS similar to that of atoms. From this attribute arises a wide range of applications.

For example, exploiting these unique properties make quantum dot lasers possible which are superior to semiconductor diode lasers regarding the threshold current density and temperature stability of the threshold current. In terms of quantum cryptography single photon sources based on quantum dots are promising devices for secure key distribution [3]. Also applications as 1.3 μm photonic devices or the development of quantum dots in order to realize qubits for quantum computing are research topics attracting a lot of interest.

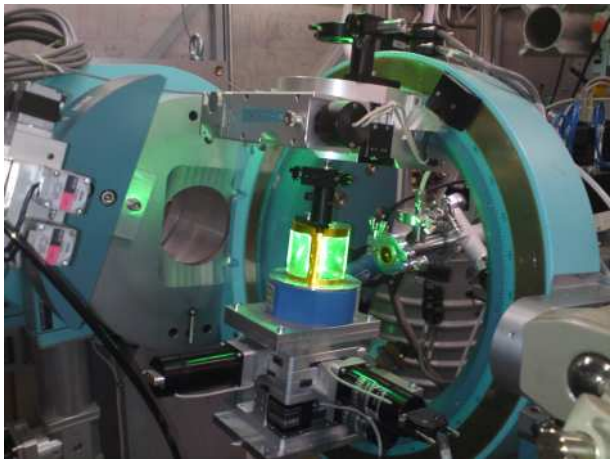

Figure 1: Picture of the in situ sample cell mounted on the flow cryostat inside of the diffractometer at the beamline BL9, DELTA.

A further specific feature is the ability to fabricate structures with atomic precision by self-organized growth. The epitaxial assembly of quantum heterostructures by the Stranski-Krastanov (SK) growth has established as the technique of choice leading to well defined quantum dots with a narrow size distribution. Based on the deposition of material on a substrate of different lattice constant forming a wetting layer, these structures emerge from a minimization of the elastic energy at the expense of the surface energy. Indium Arsenide (InAs) and Gallium Arsenide (GaAs), growing both in the zinc blende structure, exhibit a lattice mismatch of 7%. This attribute predestinates these materials for the SK growth giving rise to considerable strain fields in quantum dot heterostructures. The strain affects significantly the electronic properties of quantum dots e.g. the band structure and gap [4,5].

Previous X-ray studies have determined the strain distribution in quantum dots [6,7]. However, subject to these studies have been passive quantum structures. In the case of excited quantum dots, which will be subject to our study, the injected charge carriers may alter the strain field and consequently the electronic properties. These lattice distortions arising from optically excited carriers have been monitored up to now only indirectly by high resolution continuous wave or non-linear time-resolved optical spectroscopy [8-12].

At the beamline BL9, we have applied anomalous x-ray diffraction in combination with a laser shutter system and a liquid helium flow cryostat setup. The laser system consisted of a Klastech Symphony Nd:YAG laser device operating at a wavelength of 532 nm with an output power of 1 W (cw) which enabled us to excite the whole sample. The cryogenic environment was essential for suppressing the non-radiative recombination of the charge carriers in the quantum dots. Therefore, we have ensured that the x-ray beam probed a sample area containing only excited quantum dots. The state of excitation of the quantum dots was monitored in situ by photoluminescence spectra.

For our experiments we have used an InAs/GaAs quantum dot multilayer grown on a GaAs substrate. The sample consists of 5 quantum dot layers seperated by 30 nm GaAs spacing layers and capped with 50 nm GaAs. The 5 period multilayer structure increases the amount of quantum dots in the volume probed by the x-ray beam. A further increase of the number of quantum dot layers was not possible due to the absorption of the laser light inside of the GaAs matrix. Typically, the density of InAs/GaAs quantum dots is 10^{10} to 10^{11} cm^{-2}. In the case of capped quantum dots, they have a base diameter of approximately 20 nm and their height is in the range of a few nanometer. Thus, the quantum dots cover only a low percentage of the wetting layer.

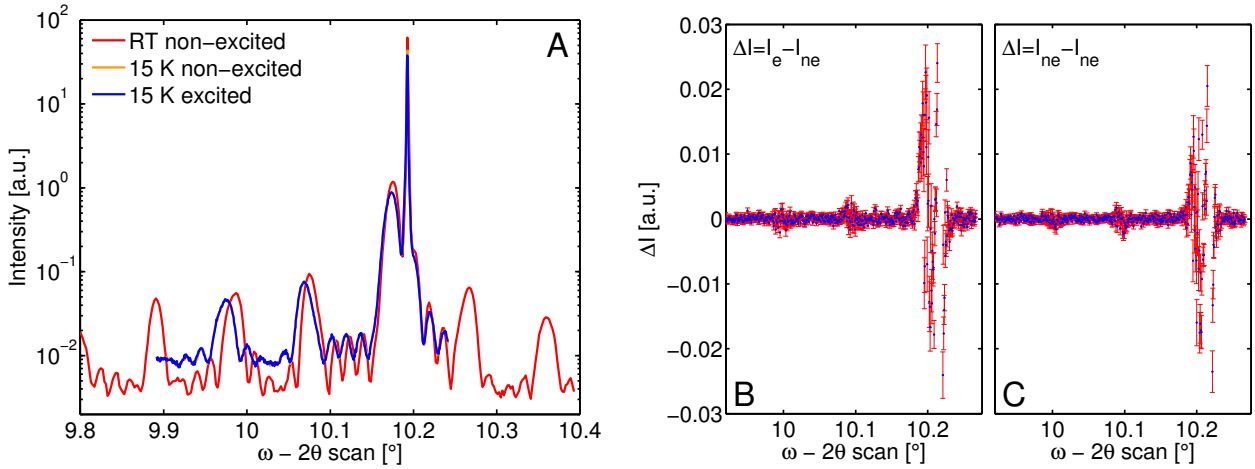

Figure 2: Left: $\omega - 2\theta$ scans of sample QD13776 in the vicinity of the (002) superstructure reflection in non-excited state at room temperature (red line) and at 15 K (orange line) as well as in excited state at 15 K (blue line). Right: Difference plots (blue dots) of data collected in excited state and non-excited state I_e-I_{ne} and data collected with switched-off laser I_{ne}-I_{ne}. Error bars are denoted in red.

Furthermore, the quantum dots are subject to seggregation of GaAs during the growth process resulting in an inhomogenous distribution of InAs inside of the dots. Hence, the scatter intensity steming from the quantum dots is extremely low in comparison to the scatter intensity from the GaAs matrix.

In order to improve the quantum dot's scattering contribution, we have performed ω - 2θ scans at the (002) superstructure reflection. By choosing a photon energy of 12.38 keV, this reflection allows the suppression of the scattering amplitude of the GaAs matrix by a factor of 500 based on the scattering amplitude of InAs.
Figure 2A depicts the ω - 2θ scans at the (002) superstructure reflection. As a reference, we probed the non-excitated sample at room temperature (red line). From the position of the multilayer peaks we can derive the thickness of the multilayer period which is approximately 31 nm. After cooling the sample down to 15 K, we have performed difference scans by recording each scan point alternately in non-excited state (orange line) and excited state (blue line). The difference scans differ significantly from the reference scan at room temperature. This effect originates from a mechanical issue caused by the helium transfer tube. Its semi-flexible characteristic led to a displacement of the sample stage during the variation of the incident angle and therefore pertubated the difference scans.
Figure 2B shows the difference plot of the data collected in excited and non-exicted state for one particular difference scan. At the positions of the superlattice peaks we observed features in the difference plot. Unfortunately, these deviations are also present in difference scans with the laser switched-off (see Figure 2C). On an absolute scale, this effect corresponds to variations of only a few counts regarding the detected intensity of $\sim 10^6$. In fact, these features are artefacts arising from systematical errors caused by the data processing. Hence, no laser-induced lattice distortions perpendicular to the sample surface could be monitored yet.
Acknowledgment. The DELTA staff is gratefully acknowledged for providing synchrotron radiation. S. T. and D.C.F. W. thank the NRW Forschungsschule 'Forschung mit Synchrotronstrahlung in den Nano- und Biowissenschaften' for financial support.

References

[1] F. Henneberger, O. Benson, Semiconductor Quantum Bits (World Scientific, Singapore, 2008). [2] D. Bimberg, M. Grundmann and N. N. Ledentsov, Quantum Dot Heterostructures (John Wiley and Sons, Chichester, 1999). [3] P. Michler et al., *Science* **290**, 2282 (2000). [4] O. Stier et al., *Phys. Rev. B* **59**, 5688 (1999). [5] F. Guffarth et al., *Phys. Rev. B* **64**, 085305 (2001). [6] I. Kegel et al.,*Phys. Rev. Lett.* **85**, 1694 (2000). [7] T. U. Schülli et al., *Appl. Phys. Lett.* **81**, 448 (2002). [8] P. Borri et al., *Phys. Rev. Lett.* **87**, 157401 (2001). [9] P. Borri et al., *Phys. Rev. Lett.* **91**, 267401 (2003). [10] A. Vagov et al., *Phys. Rev. B* **70**, 201305 (2004). [11] B. Krummheuer et al., *Phys. Rev. B* **71**, 235329 (2005). [12] A. Krügel et al., *Phys. Rev. B* **76**, 195302 (2007).

Characterisation of Diamond Cobalt Composites

Andre Steffen[a,*], Michael Paulus[a], Manuel Ferreira[b], Christian Kronholz[b], Wolfgang Tillmann[b], and Metin Tolan[a]

[a] *Fakultät Physik/DELTA, TU Dortmund, Maria-Goeppert-Mayer-Str. 2, 44227 Dortmund, Germany.*
[b] *Institute of Materials Engineering, TU Dortmund, Leonhard-Euler-Str. 2, 44227 Dortmund, Germany.*

*E-Mail: andre.steffen@tu-dortmund.de

Introduction. Drilling bits, wire saws and saw blades are loaded with diamond cutting segments that enable many applications such as grinding and cutting of super hard materials, e.g. concrete and granite [1-5]. Diamond tools are composite materials that are produced powder metallurgically [6]. After the uniaxial cold pressing of the powder mixture including the diamonds the sintering process is the last production step to enabe the bonding between the diamonds and the metal matrix. As the diamonds are primarily responsible for the grinding process this bonding is of great interest bearing the forces at each diamond particle [5,7-8]. Cobalt is still a common used and very important matrix material [1-3,8]. Research studies point to the fact that the formation of a chemical bonding is caused either by the formation of solid solutions or the formation of metal carbids. For example Nittono et al. and Wang et al. report that cobalt carbides are metastable [9-10], Molinari et al. reported about the formation of stable cobalt carbides in hot pressed cobalt based tools [6]. The studies we performed in 2009 at BL9 of DELTA only showed a graphitisation of diamond during the sintering process. The formation of cobalt carbides could not be verified [1-3].

This report is deals with x-ray diffraction (XRD) studies we performed in June 2010 at BL9 of DELTA. We characterised an industrial workpiece and a cobalt coated diamond. Furthermore we tried to induce the formation of cobalt carbides in situ by annealing a mixture of cobalt and diamond particles. At least we report about the dependency between the cooling rate and the hexagonal closed packed (hcp) and the face centred cubic (fcc) phase composition of cobalt powder.

Industrial workpiece. According to the manufacturers information the industrial workpiece consisted of diamonds embedded in a cobalt (Co) bronze (CuSn), 80% Cu and 20% Sn, matrix. The sample had a thickness of several centimeters and therefore was investigated by surface x-ray diffraction. The characterisation of the diffraction pattern, see figure 1, leads to the result that only the phases of the metallic matrix can be clearly determined. The Co fcc phase is very strong in comparison to the small Co hcp volume fraction. The CuSn structure corresponds to an expanded Cu latice. Furthermore a very weak graphite reflection can be observed at 2Θ=7.9°. Distinct reflections from diamond or cobalt carbides could not be detected. All in all this experiment confirms former results that show a graphitisation of diamond but do not reveal the existence of cobalt carbides.

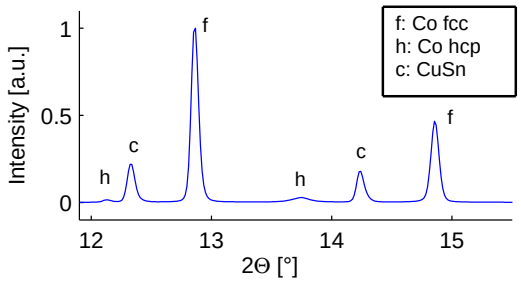

Figure 1: XRD pattern of an industrial workpiece.

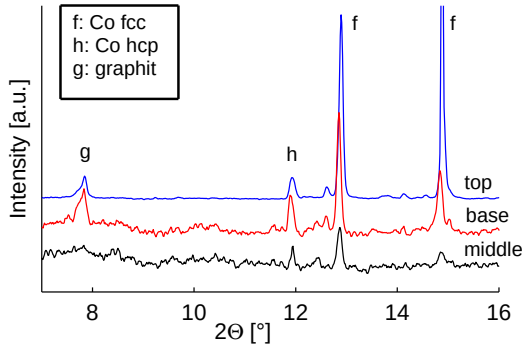

Figure 2: XRD pattern of Co coated diamond.

Cobalt coated diamond. Similar to the industrial workpiece a cobalt coated and sintered diamond was investigated by x-ray diffraction. The size of the diamond was about 2x2x2 mm^3. Three slices (top, base and middle) of the sample were investigated in transmission geometry. In figure 2 the diffraction patterns of all slices are given. for better visibility the intensity of the scattering signal from the top slices is reduced by a factor of ten. It is obvious that the signal from the top slice is much stronger than the signals from the middle and the base slice. In all slices the reflections from Co fcc, Co hcp and graphite can be identified. A further accordance to former results is the fact that the Co fcc volume fraction dominates.

In situ sintering. The in situ sintering of the diamond cobalt composites is important due to two reasons. First, such an in situ study enables to get information about the time scale of the chemical reactions. The second reason is that cobalt carbides, if they are metastabile, may only exist at high temperatures and therefore cannot be detected at room temperature. The experiment has been realised by filling a mixture of cobalt powder and synthetic diamond grains in a capillary and by annealing. Due to technical problems the experiment could only run around one hour. During that duration the phase transition from Co hcp to Co fcc phase could be observed as expected. In figure 3 the diffraction patterns from the native and the annealed (T=800°C) sample are shown. At the beginning both the hcp and the fcc phase coexisted. In the end only the Co fcc phase was present. The shift in the scattering angle is caused by the thermal expansion of the lattice. Neither the graphitisation nor a formation of cobalt carbides could be detected. The absence of graphite and cobalt carbides might be due to the low contact areas between diamond and metal grains as the sample was not compacted.

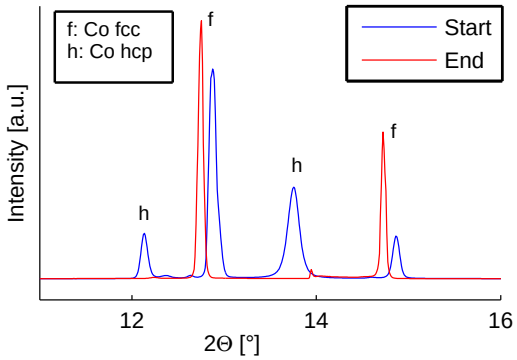

Figure 3: In situ sintering of Co powder and diamond grains.

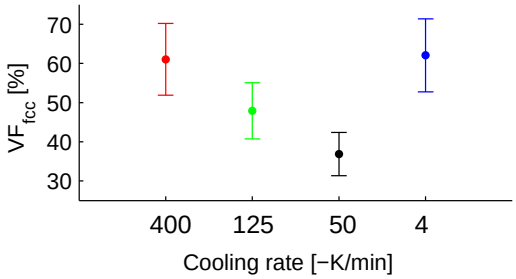

Figure 4: Cobalt phase composition versus cooling rate.

Cooling rate. Even at room temperature cobalt powder occurs in low temperature hcp and in high temperature fcc phase. The influence of the cobalt phase composition on the performance of diamond cobalt tools is given by their different mechanical properties. For example in comparison to the Co fcc phase the Co hcp phase is more brittle and less ductile. Former studies indicate that the hcp fcc phase composition can be tuned by the cooling rate after annealing cobalt at high temperature. Fast cooling leads to high amounts of the Co fcc phase also at room temperature. Slow cooling enables a strong fcc to hcp phase transition. Figure 4 shows the Co fcc volume fractions, VF_{fcc}, of similar annealed cobalt powders. The cooling rates of these four samples differed between -400 and -4 K/min. The Co hcp phase volume fraction is given by 100%-VF_{fcc}. The decrease of the VF_{fcc} by variing the cooling rate from -400 to -125 K/min is expected, as explained above. Therefore the VF_{fcc} that corresponds to the cooling rate of -4 K/min does not fit to our previous results. Nevertheless the study on this correlation needs to be continued. Especially the interesting region, cooling rates between -100 and -5 K/min, need to be investigated in detail.

Acknowledgements

The authors like to acknowledge the DELTA machine group for providing synchrotron radiation and technical support. A. Steffen thanks the NRW Forschungsschule 'Forschung mit Synchrotronstrahlung in den Nano- und Biowissenschaften' for financial support.

References

[1] A. Steffen, Diploma thesis, TU Dortmund, 2009.
[2] C. Kronholz, A. Steffen, M. Ferreira, M. Paulus, Ch.J. Sahle, M. Tolan, and W. Tillmann, Report DELTA User Meeting, 2009.
[3] A. Steffen, M. Paulus, Ch.J. Sahle, C. Kronholz, M. Ferreira, W. Tillmann, and M. Tolan, paper submitted to Materials Science and Engineering A.
[4] W. Tillmann, M. Gathen, C. Kronholz, Materialwissenschaften und Werkstofftechnik 38 (2007) 112-115.
[5] B. Kieback, Ch. Sauer, W. Tillmann, Proc. Int. Workshop on Diamond Tool Production, Turin, 1999.
[6] A. Molinari *et al.*, Materials Science and Engineering A 130 (1990) 257-262.
[7] M. Zeren, S. Karagz, Materials and Design, 28 (2007) 1055-1058.
[8] A. Romanski, Powder Metallurgy 50 (2007) 115-119.
[9] O. Nittono, Y. Fukumiya, Y. Haga, Materials Science and Engineering A 312 (2001) 248- 252.
[10] H. Wang, M.F. Chiah, W.Y. Cheung, S.P. Wong, Physics letters A 316 (2003) 122-125.

The X-ray investigation of doping influence on InAs wire by selective area MOVPE growth

A. Davydok[a], A. Biermanns[a], K.Sladek[b] and U. Pietsch[a]

[a]*Festkörperphysik, Universität Siegen, Walter-Flex-Str. 3,57072, Siegen, Germany*
[b]*Institut für Bio- und Nanosysteme (IBN-1), Jülich Aachen Research Alliance (JARA,)Forschungszentrum Jülich, 52425 Jülich, Germany*

Nanowires (NW) growth is typically realized using vapor-liquid-solid (VLS) mode in MOVPE [1] or MBE onto [111] planes of a zinc-blende or diamond type semiconductor by solution from a molten eutectic alloy formed by metallic seed. In the case of catalyst-free Selective Area MOVPE mode semiconductor NW's grow in periodic arrays throughout pre-patterned dielectric mask onto [111]B surface. Diameter and position of grown NWs is defined by position and size of drilled holes within the dielectric mask [2]. Moreover using doping during growth process aspect ratio can be controlled. But influence on crystal structure of NW's is not so clear.

In recent experiments we investigated the doping influence on InAs NWs onto GaAs[111] substrate grown by SA-MOVPE through SiOx layer. Home measurements revealed that the InAs NRs are grown with lattice parameters known from bulk material. Measuring 111 Bragg reflection the intensity of InAs peak revealed to be proportional to the doping level in the sample. In particular two 2 samples were measured: (1) without doping and (2) sample Si doped with factor of 250x.

In order to determine the particular influence of doping on phase structure of the wires we measured reflection being oblique to the [111] growth direction. In particular we have chosen the 105 WZ reflection what has no overlap with any zinc-blende type reflection. On other hand the 311 reflection appears only in case of a zinc-blende structure. Unfortunately the detected intensities appeared with too low and we were not able to resolve the mentioned reflection signals using the high-resolution setup at BL9 using an analyser crystal in front of the detector.

Fig. 1 shows a radial scan through the GaAs(111) reflection. Intense peaks are observed corresponding to InAs NR's appearing at qz=17.90 and at GaAs position at qz=19.24. The later peak was used for internal calibration of the angular scale.

FWHM of InAs peaks from q_z scans are corresponding to vertical size of NW's ~1μm for both samples. Rocking curves measured at InAs position can be represented by a

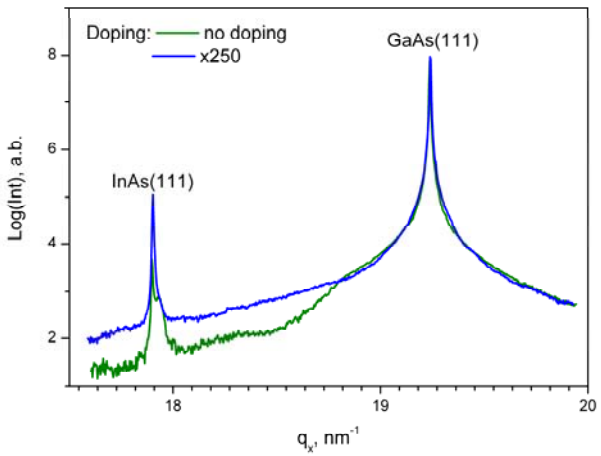

Fig.1 Radial scan through the GaAs(111) reflection

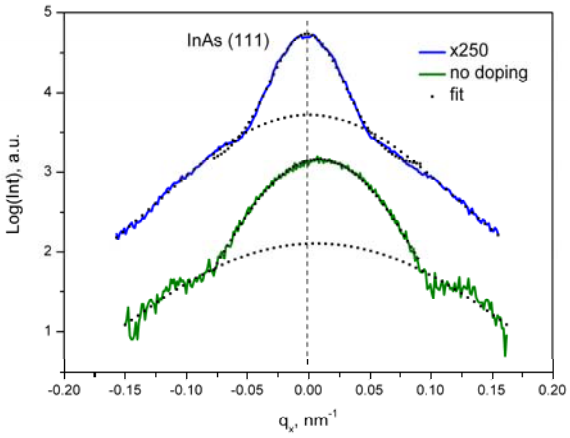

Fig. 2. Rocking curves measured in InAs(111) reflection

superposition of two different Gaussians with different FWHM. The Gaussians on top (see Fig.2) corresponds to widths of 90nm and 330 nm for no doped and doped samples,

respectively. Bottom part of both peaks can be fitted with the same Gaussian – independent from doping which is associated with diffuse scattering from SiOx mask. Suppose to be crystallized SiOx layer around the perfectly align nanowires [3]. Note the small sift of peak from q_x=0 position for the non-doped sample.

As first results we observed a clear between size of nanowires and the doping level applied during a grow process. In future we are planning to extend this investigations to samples with different doping level. With PILATOS detector installed at BL9 our future experiments become more successful.

References

[1] J. Fan, P.Werner and M. Zacharias Small 2, No 6, (2006) 700-717
[2] H. Paetzelt, V. Gottschalch, J.Bauer, G.Benndorf, G.Wagner, *J.Cryst. Growth* **310**, 5093 (2008).
[3] A. Davydok, A. Biermanns, U. Pietsch, J. Grenzer, H. Paetzelt and V. Gottschalch, Metallurgical and Materials Transactions A, 41, 5, 1191-1195

A new PILATUS detector set-up for fast reflectivity measurements at BL9

J. Nase*, M. Paulus, C. Sternemann, S. Tiemeyer, F. Wirkert, M. Tolan
Fakultät Physik/DELTA, TU Dortmund, Maria-Goeppert-Mayer-Str. 2, D-44227 Dortmund, Germany

*email: julia.nase@tu-dortmund.de

We report the set-up of a PILATUS detector at beamline 9 of DELTA. The large sensitive area of $83.8 \times 33.5\,\mathrm{mm}^2$ and the high dynamic range allow for fast reflectivity measurements with fixed detector position. First test measurements showed that we could monitor the time dependent adsorption of lysozyme at a solid-liquid interface. A single reflectivity was performed in as little as 55 s.

Detector and set-up. The recently purchased 2d PILATUS-100k detector from Dectris is based on a CMOS hybrid pixel technology. It has no dark current or readout noise, a read out time of less than 3 ms, and a frame rate of over $200\,^{\mathrm{images}}/_{\mathrm{s}}$ [1]. During operation, the detector is constantly flushed with nitrogen. More technical details are given in table 1 at the end of this report. PILATUS comes with two software components, *TVX,* a data acquisition control and data analysis tool, and *Camserver,* the operating software for the detector.

To realize fast reflectivity measurements, the PILATUS detector was mounted on a fixed metal support at the height of the incoming beam. A flight path, flushed with helium, was fixed on a movable arm. Two apertures at both sides of the flight path suppressed scattered radiation and reduced the background level. The main difference to classical reflectivity measurements is that the detector remained fixed at its position while the sample was tilted continuously from 0° to an angle θ_{max}. Parallel to the sample, the flight path with slits was moved by an angle 2θ. An absorber is not required due to the high dynamic range of 10^6 per pixel. The reflected beam covered the detector area, yielding an image as shown in figure 1(a). Integrating the region of interest (red square frame) column to column, one obtains the intensity as a function of the pixel position, which can be converted into a 2θ scale. A reference measurement showed a perfect linear dependence between the pixel position and the reflected angle 2θ. The angular resolution was 0.0042°. The resulting reflectivity is shown in figure 1(b).

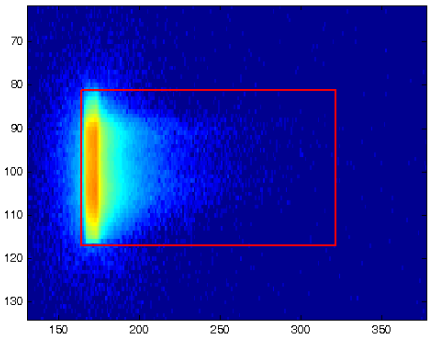

(a) 2d image after accumulated exposure in a reflectivity measurement.

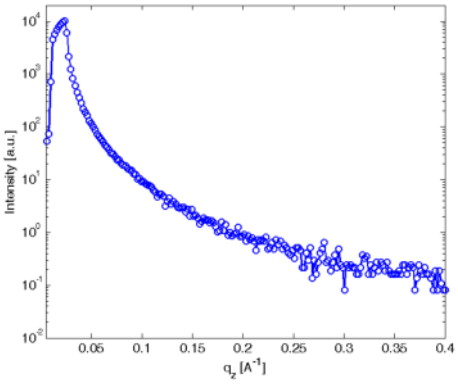

(b) Resulting reflectivity after integration.

Figure 1: TIFF image of a reflectivity scan using the PILATUS detector and corresponding reflectivity.

Material and methods. As first test measurements at an incident energy of 27keV we investigated the adsorption of lysozyme, a protein that is ubiquitous in animal organisms. Its shape is elliptic, with dimensions of $45 \times 30 \times 30\,\mathrm{Å}^3$ [2]. We designed a sample cell for reflectivity measurements at the solid-liquid interfaces, e. g. between a silicon wafer and water. Requirements were first, a small cell volume to reduce the background scattering from water and second, a device to fix the wafer in the cell and guarantee thus a stable wafer position and high angle accuracy. The cell was made of teflon for an easy cleaning with dimensions of $20 \times 20 \times 28\,\mathrm{mm}^3$. A sample holder allowed to fix a wafer at the cell bottom.

Silicon wafers with dimensions of about $10 \times 10\,\mathrm{mm}^2$ were thoroughly cleaned by RCA process and stored under ultrapure water. The buffer was a solution of 55 mg Na_2HPO_4 in 45 ml ultrapure water and had a pH of 8.5. Lysozyme from chicken egg purchased at Sigma Adrich was used as received. 10 mg of protein were dissolved in 10 ml of buffer solution. Further dissolving, we obtained concentrations of $1\,^{\mathrm{mg}}/_{\mathrm{ml}}$ and $0.1\,^{\mathrm{mg}}/_{\mathrm{ml}}$. The final concentration was adjusted placing different amounts of these solutions into the cell. We show results from two series with final concentrations $c_1 \approx 1\,^{\mu\mathrm{g}}/_{\mathrm{ml}}$ and $c_2 \approx 0.1\,^{\mu\mathrm{g}}/_{\mathrm{ml}}$.

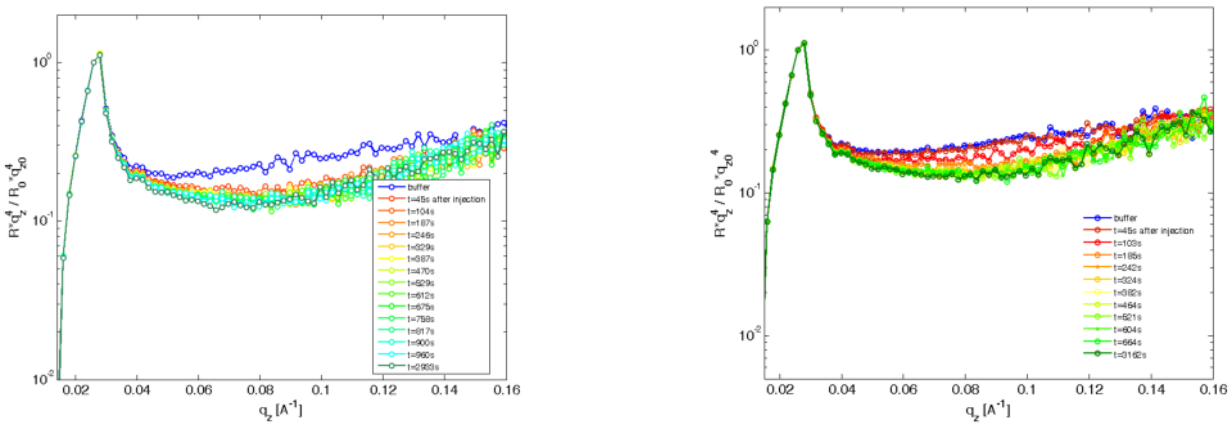

(a) $c = 1\mu$g/ml. (b) $c = 0.1\mu$g/ml.

Figure 2: Intensity as a function of the wave vector transfer $q_z = \frac{4\pi}{\lambda} \sin\theta$ for two different protein concentrations. λ is the wavelength of the incident radiation.

Results. The measurement protocol for the reflectivity measurements at the solid-liquid interface was as described in the following. First, the wafer was placed in the wafer holder and into the teflon cell. The cell was carefully filled with about 10 ml of buffer solution. After adjustment of the wafer, a reference reflectivity without protein was recorded. We then placed a small amount of protein solution (between 10 µl and 100 µl) with a syringe onto the water surface and started the first reflectivity measurement as fast as possible. In general, we obtained a delay of about 45 s between protein injection and start of the first measurement, caused by sample handling and the beamshutter closing time. For continuous data acquisition measurements were performed scanning the 2θ and θ motors in forward and backward direction, that is, from $0\,^\circ$ to $\theta_{\max}$ and then from $\theta_{\max}$ to $0\,^\circ$. In that way, we were able to record fast reflectivity measurements during the adsorption of lysozyme molecules at the wafer surface. Going from $0\,^\circ$ to $0.8\,^\circ$, a single reflectivity took about 110 s. Reducing the angle range to $\theta = 0.4\,^\circ$, a region where changes in the intensity were visible, the duration of a single scan was reduced to 55 s. Figure 2 shows results for two concentrations. The intensity is weighed with q_z^4 for a better visibility of small changes. With ongoing time, the intensity obviously decreases until a stable state is reached.

Conclusion and outlook. During one week of beam time, a PILATUS-100k detector was installed at BL9 and a new set-up for fast reflectivity measurements was put into operation. First test measurements with lysozyme solutions showed that in a sequence of reflectivities taking 55 s each, we could demonstrate the temporal evolution of protein adsorption at a solid-liquid interface. Thus this set-up provides a strong tool for the investigation of time-dependent processes by x-ray reflectivity measurements.

In the future, a more systematic study of lysozyme adsorption will allow us to obtain quantitative information about the adsorption process. We will improve the set-up by an automation of the protein injection. In that way, we will be able to monitor the processes at the wafer surface without delay. It will also be interesting to investigate lower protein concentrations with slower dynamics.

The authors like to acknowledge the DELTA machine group for providing synchrotron radiation and technical support.

pixel size	$172 \times 172\,\mu\text{m}^2$
format	$487 \times 195 = 94965$ pixel
area	$83.8 \times 33.5\,\text{mm}^2$
counting rate per pixel	$> 2 \times 10^6\,{}^1/_\text{s}$
energy range	5-30 keV
read-out time	2.7 ms

Table 1: Specifications of PILATUS type 100K-S.

References

[1] Dectris User Manual, 2010.

[2] S. Tiemeyer et al., *Effect of Surface Charge Distribution on the Adsorption Orientation of Proteins to Lipid Monolayers*, Langmuir, 26(17) 14064-14067, 2010.

DELTA Experimental Report

Experiment title: Micro- and Nanostructure of the Protein-Fibre Silk as a Function of Hydrostatic Pressure and Cosolvent Concentration

Main proposer: Christina Krywka **Coproposers:** Florian Kunze, Martin Müller

Report text: The experiment was performed at the beamline BL9 at two different photon energies: 10 keV for the SAXS (Small-Angle X-ray Scattering) measurements at ~1.1 m sample to detector distance) and 27 keV for the WAXS (Wide-Angle X-ray Scattering) measurements at ~0.5 m sample to detector distance. The beam size was approximately 1 mm². In all measurements the high-pressure hydrostatic cell with diamond-windows was used, as already implemented on BL9 in previous experiments. The samples were bunches of *Bombyx Mori* silkworm silk, typically containing 60 to 100 single silk fibres. Mounted into the modified sample holder the bunch sample was inserted into the pressure cell where it was subsequently surrounded by the pressurizing liquid (clear water or 2.5M aqueous urea solution). Fig.1 shows the high-pressure cell mounted into the diffractometer installed at BL9.

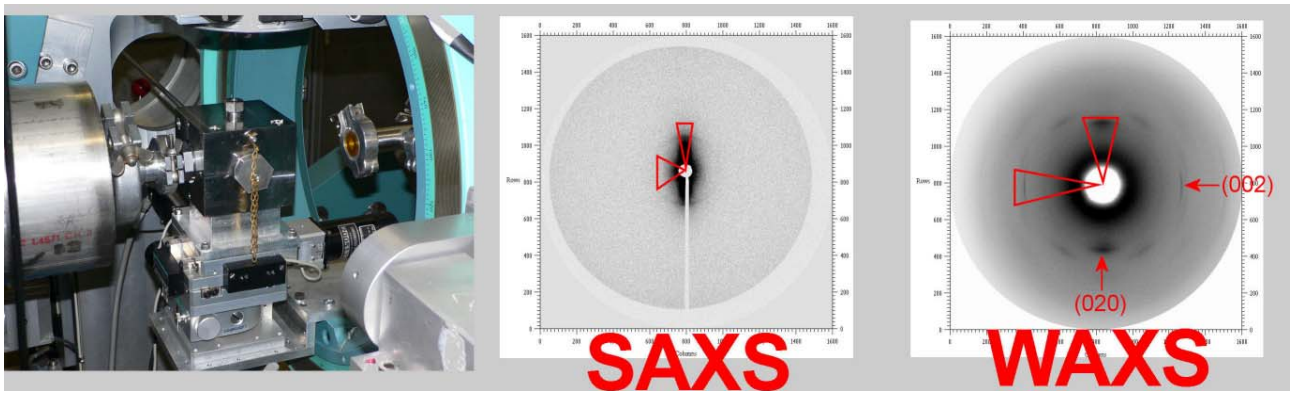

Fig. 1: Left: High-pressure cell used in the experiment, mounted into the diffractometer at beamline BL9. The sample position was set to match the Eulerian cradle's pivot point in order to be able to compensate for the strong pseudo-Kossel reflections that occur due to the passage of the beam through the sample cell's diamond windowa. **Middle+Right**: Typical diffraction images recorded with the 2D-detector for both sample-to-detector distances (SAXS and WAXS). The equatorial and meridional sections (horizontal and vertical, resp.) used in the evaluation are indicated and in the WAXS image the miller indices for the relevant silk fibroin reflections are also displayed.

Both, in SAXS and WAXS geometry, measurements were performed at different hydrostatic pressures of 100 to 4500 bar and the acquisition time for each measurement was 30 minutes. The data at 100 bar were considered to be equivalent to atmospheric pressure as at this low pressure no structural changes in the sample are expected. However, at 100 bar we could assume that no gas bubbles remained in the pressurizing liquid. After radial integration of the equatorial and meridional sections of the 2D-data (see Fig.1) several corrections were made to the so achieved 1D-data. As water and silk expose different, non-negligible compressibilities, these corrections were necessary to compensate for the pressure induced changes in scattering contrast, i.e. to normalize the data. Also, the pressure dependent weakening of the scattered intensity had to be accounted for, which is due to the density increase of the pressurizing medium (water) through which the scattered signal must pass before it exits the sample cell. Exemplary corrected data for both SAXS and WAXS geometry is shown in Fig.2.

Despite of the corrections mentioned above, the SAXS data exposes a decrease of the scattering curve intensity with increasing pressure. This is in contrast to our previous SAXS data recorded with is situ tensile strain (stretching) rather than pressure applied to the silk fibres. Further evaluation is in progress, especially with a focus on the origin of the intensity increase in the tensile strain data.

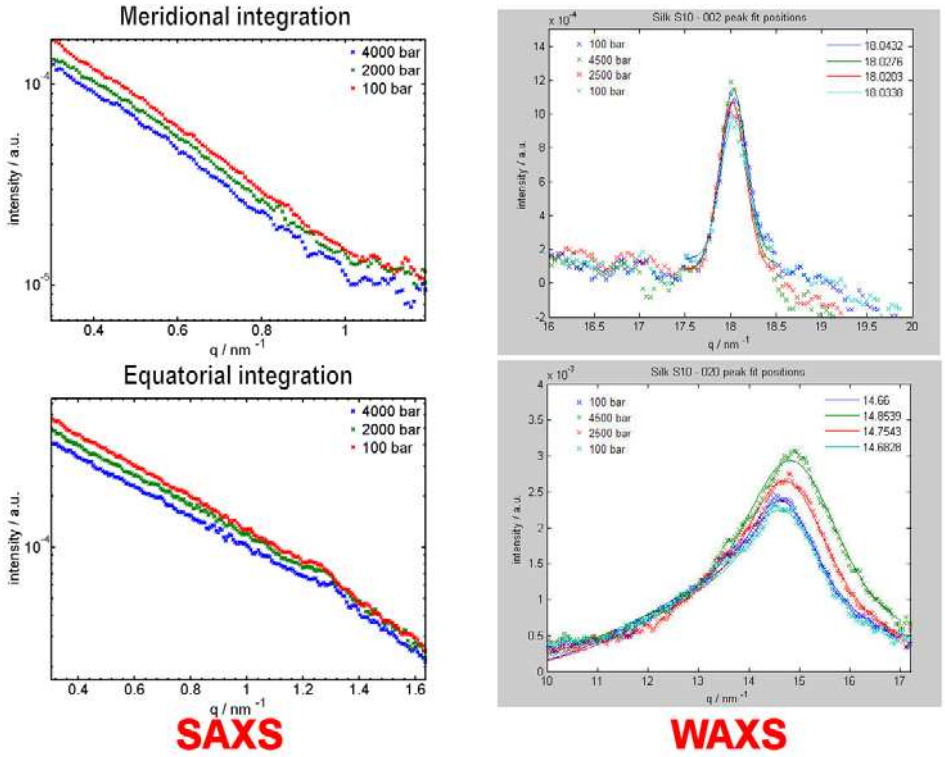

Fig. 2: Radially integrated and normalized pressure dependent data, recorded from silk in SAXS and WAXS geometry. The SAXS data is plotted semilogarithmically in order to better visualize the remaining, slight, yet systematic intensity offset. In WAXS geometry a distinct, reversible shift of the (020) peak position is evident. The position of the corresponding (002) reflection, however, remains constant.

The WAXS data, on the other hand, exposes a distinct pressure dependent shift of the (020) peak position while in the orthogonal direction (i.e. the (002) peak position) no structural changes occur. Assuming the (020) peak's main contribution being the intersheet spacing of the nanocrystallite β-sheets which in turn are aligned parallel to the fibre axis, this peak shift corresponds to a closing in of the beta sheets, i.e. a compression of the crystallites in the [020] direction. The peak shift is reversible and it is proportional to the pressure. At 4500 bar it corresponds to an intersheet spacing reduction of 1.3 %. This complements well our previous WAXS data recorded with tensile strain applied (i.e. stretching the fibre) where there is only an increase of the interchain distances, i.e. a stretching of the polypeptide chains which constitute the β-sheets. The comparison of all the measured effects and how they compete with our previous data is shown in Fig.3. When the pressurizing medium water was replaced with a high concentration aqueous urea solution (2.5 M) no change in any of the aforementioned shifts was observed.

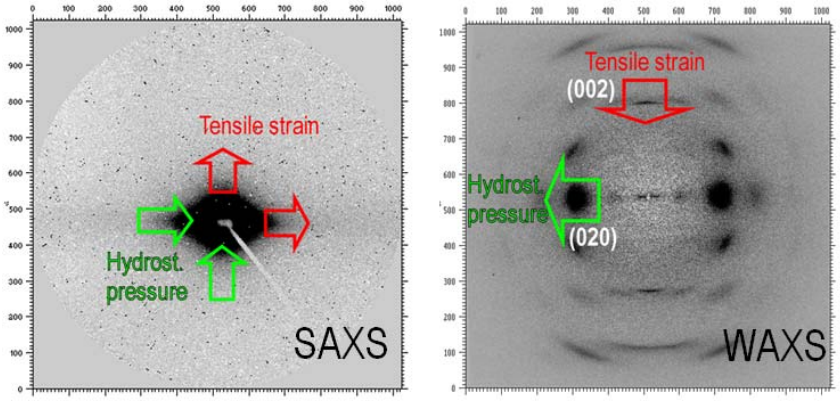

Fig. 3: Comparison of the effects of (hydrostatic) pressure and axisl (tensile) strain applied to silk fibers and the resulting changes in the SAXS and WAXS scattering patterns. **Left**: The red and green arrows indicate how the SAXS scattering pattern grows and shrinks due to tensile stress and hydrostatic pressure, respectively. **Right**: The red and green arrows indicate the shifts of the (002) and (020) reflections as the fiber is exposed to tensile stress and undirected hydrostatic pressure, respectively.

Further data evaluation is in progress. As due to time restrictions only two WAXS could be performed an experiment at the ESRF beamline ID13 is scheduled for December 2010 to validate the data presented here.

Influence of Alkyl Side Chain Length on the Orientation of Poly(3-alkylthiophene) of Molecules in Thin Films

Thankaraj Salammal Shabi, Souren Grigorian, Martin Brinkmann, Ullrich Pietsch, Nils Koenen, Ullrich Scherf

Conducting polymers are placing a significant role in the fabrication of lightweight, flexible electronic devices [1, 2] using low-cost of preparation techniques like spin-coating, printing, and drop casting etc. Especially, polythiophene based polymers play a vital role in the fabrication of organic field effect transistors (OFETs), organic solar cells, and organic light emitting diodes etc. Due to the importance of poly(3-alkylthiophene)s (P3ATs) in molecular electronics we have focused our attention to understand the influence of alkyl side chain length on the structural properties of thin films. Up to now it is accepted in the literatures that, the side group with C_6H_{12}+1 unit (hexyl) is the optimum length for the better performance of OFET and solar cells [3, 4].

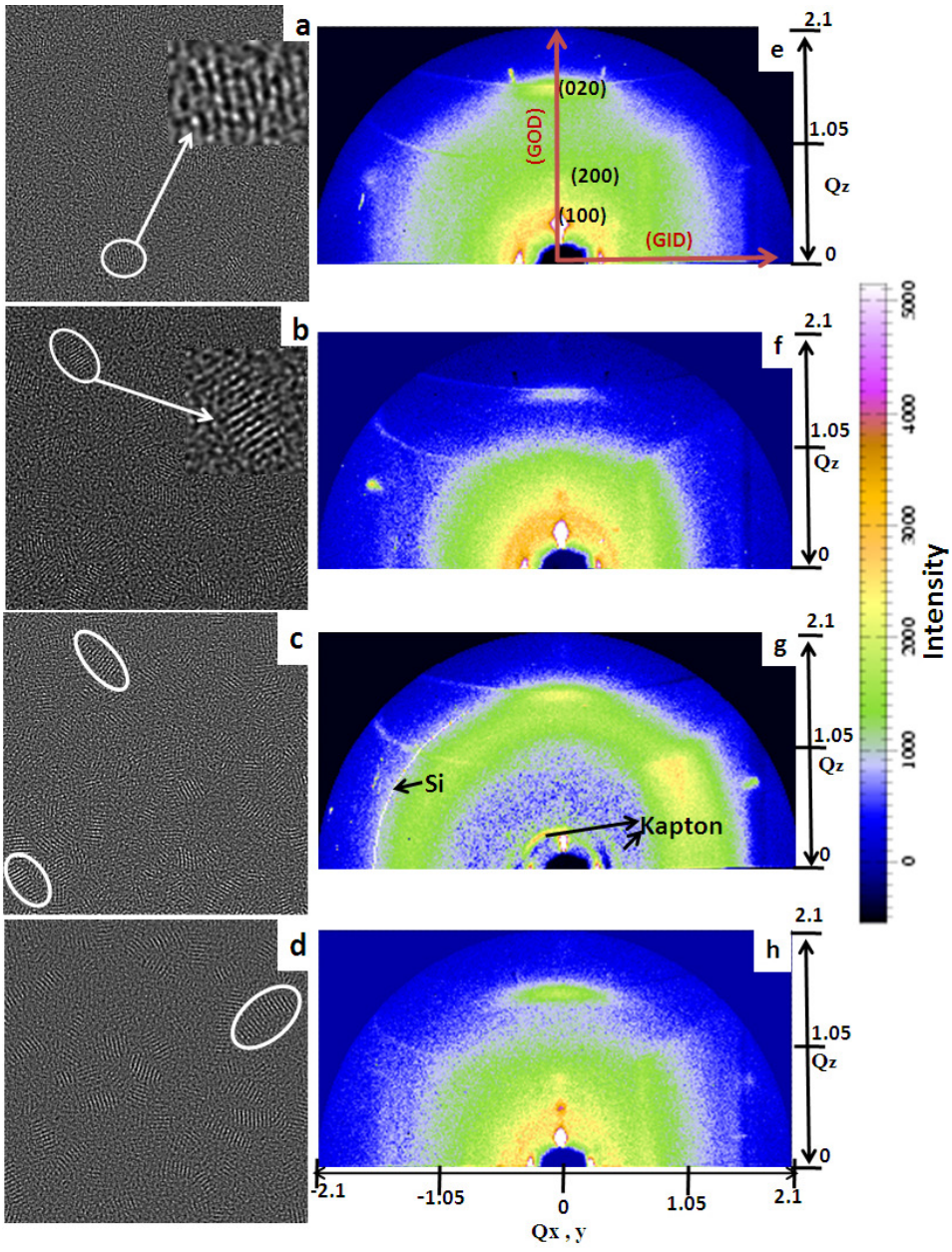

In order to verify this approach we have analyzed the structural properties for a series of P3AT polymers like poly(3-pentylthiophene) (P3PT), poly(3-hexylthiophene) (P3HT), poly(3-heptylthiophene) (P3HeptT), and poly(3-octylthiophene) (P3OT), respectively. The polymer thin films were prepared through spin coating and low temperature drop casting technique where the latter one is used to improve the ordering. The orientation of the crystallites was studied through high-resolution transmission electron microscopy (HRTEM) as well as non destructive x-ray and electron

Figure 1. HRTEM images of spin coated P3AT polymers of having area 150nm^2 (left column) and theirs corresponding 2D x-ray diffraction patterns (right column); P3PT (a and e), P3HT (b and f), P3HeptT (c and g), P3OT (d and h).

diffraction analysis. The P3AT thin films show both edge-, and face-on oriented crystallites considering the results of HRTEM and X-ray diffraction. The percentage of face-on oriented crystallites is increasing with increasing the length of alkyl side chains (Figure. 1left). This tendency was evaluated from the increase in intensities of (020) x-ray Bragg peak along the out-of-plane (q_z) direction (Figure 1right) measured at DELTA. In addition a reduction in the surface roughness was observed with increase of edge-on oriented crystallites which fairly coincides with the observation mentioned above. Thickness and roughness of the films were quantified by simulating the measured reflectivity profiles using Parratt32 software. The high degree of edge-on oriented crystallites has been obtained by drop casting them at -30°C. While comparing the series of investigated P3AT films, P3OT has maximum number of face-on oriented crystallites compared to the other polymers and it shows maximum amount of diffuse scattering as well. Both the findings can be explained by the increase in flexibility of alkyl side chains with increasing their lengths [5] which may induce torsion in the thiophene backbones [6].

References

(1) Wong, W. S.; and Salleo, A.; Flexible Electronics: Material and Applications, Springer 2009.

(2) Klauk, H. Organic electronics materials, manufacturing and applications,1st ed, WILEY-VCH Verlag GmbH & Co. KGaA, 2006.

(3) Friedel, B.; McNeill, C.R.; Greenham, N.C. Chem Mater 2010, 22, 3389 – 3398.

(4) Sauve, G.; Javier, A.E.; Zhang, R.; Liu, J.; Sydlik, A.; Kowalewski, T.; McCullough, R.D. J. Mater. Chem 2010, 20, 3195 – 3201.

(5) Prosa, T.J.; Winokur, M.J.; Moulton, J.; Smith, P.; Heeger, A.J. Macromolecules 1992, 25, 4364 – 4372.

(6) Xie, H.; O'Dwyer, S.; Corish, J.; Morton-Blake, D.A. Synthetic Metals 2001, 122, 287 – 296.

New beamline BL10

Konstantin Istomin[1], Anne Hüsecken[1], Ralph Wagner[2] and D.Lützenkirchen-Hecht[2]
[1]Universität Siegen [2]Universität Wuppertal

In cooperation with University of Wuppertal and Technical University of Dortmund, the solid state physics group of Siegen University is finishing the construction of the new beamline BL10 at DELTA Synchrotron in Dortmund. Beamline is devoted to materials science research with the focus on X-ray diffraction and absorption spectroscopy measurements. Possible experiments include:

1. Precise single crystal diffraction
2. Charge density studies
3. In situ fatigue studies in metals
4. Transmission and fluorescence EXAFS measurements
5. Reflection mode EXAFS, making use of the diffractometer

A schematic lay-out of the beamline in shown in Fig. 1a (optics part) and Fig.1b (experimental part).

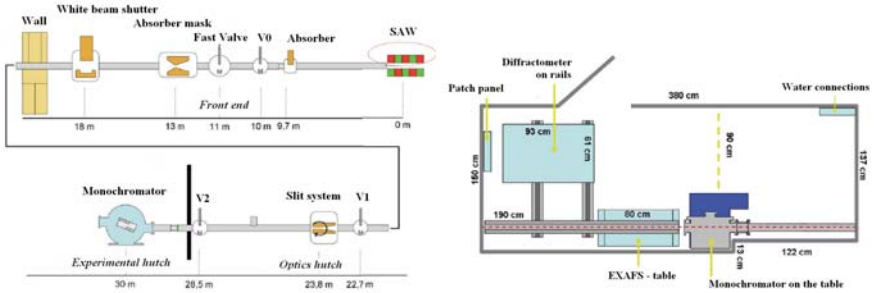

(a) BL10 Lay-out and main components (b) Experimental hutch (top-view).

After a delay related to the delivery of motor stages, the current status of the BL10 is as follow: all hardware has been delivered and already installed. All the vacuum parts have been assembled and tested: the entire beamline volume has been heated out and successfully evacuated down to 10^{-9}-10^{-10} mbar. The personal safety interlock system and the vacuum control system are ready for operation. The 4-circle Huber-diffractometer is installed at the experimental hutch, while a setup for absorption spectroscopy measurements is under construction by the University of Wuppertal. The channel-cut Si(111)-monochromator (Fig.2) has been tested in transmission EXAFS experiments at X-ray undulator beamline BW1

(HASYLAB/DESY). The measured EXAFS and XANES were in excellent agreement with reference measurements at other instruments (see Fig.3).

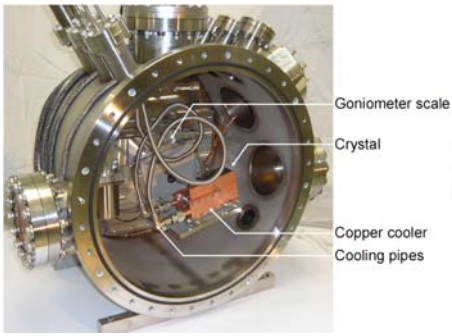

Fig. 2. Si (111) channel-cut monochromator

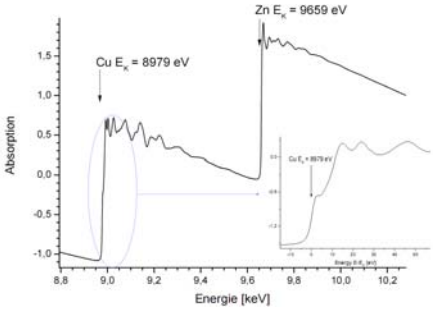

Fig. 3. K-Absorption edges of Copper and Zinc.

Current activities are focused on preparation of a vacuum test with the beam. Also the present beryllium window has to be replaced with a new water-cooled beryllium window. Depending on this, first beam in the experimental station is expected in the beginning of 2011. The beamline will be operating in ambient environment, however there is an opportunity for sample cooling in prospect. Control will be performed in standard SPEC shell. The expected parameters of the beamline are summarized in Table 1.

Table 1. Expected parameters of BL10.

Parameter	Expected value	Note
Energy range	4 – 16 keV	
Energy resolution	dE/E ~ 1.6 x 10^{-4}	
Beam size	3 x 10 mm^2 to 0.5 x 0.1 mm^2	depending on aperture
Photon Flux	5 x 10^9 Photons / s mm^2	

Investigation of the Mosaicity of real crystals

A.K. Hüsecken*,[a], O. Schmidt[a], and U. Pietsch[a]
[a] *Fakultät Physik, Universität Siegen, Walter-Flex-Str. 3, 57068 Siegen (Germany),*
*email: anne.huesecken@tu-dortmund.de

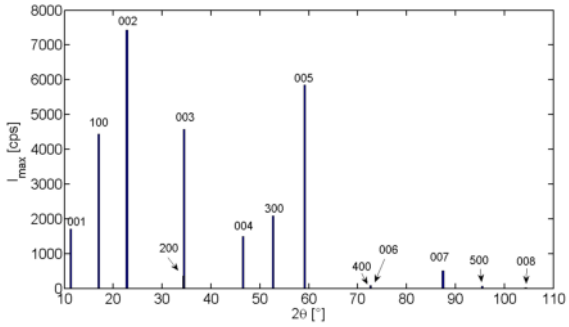

Figure 1: Measured Bragg reflections at the $Li_2SO_4 \cdot H_2O$ plate in Laue geometry.

Extinction is the weakening of the diffracted X-ray intensity due to multiple scattering in the crystal. Perfect crystals scatter according to the dynamical theory ($I \propto |F|$), but no real crystal is perfect. Ideal imperfect crystals, on the other hand, scatter according to the kinematical theory ($I \propto |F|^2$). In most cases, the measured intensities of real crystals are in between both cases and an extinction correction is needed to fulfil the kinematic approach.
Present approaches for describing extinction consider two major real structure effects: the mosaic block size and the orientation distribution of these mosaic blocks. The blocks may be not small enough to avoid multiple scattering or the orientation distribution is not sharp enough according to dynamic theory. However, most of experimentalists use the extinction as black box.

Present theories dealing with extinction correction start with a finite perfect crystal, then go to an ideal mosaic crystal and at last generalize the theory to a real crystal [1, 2, 4]. These approaches are based on a lot of approximations which are not verified by the experiment.

Our approach is to verify the validity of one of the other present extinction theories by independent diffraction experiments with high resolution. The probe system used in the measurements was $Li_2SO_4 \cdot H_2O$. It crystallizes in the space group symmetry $P2_1$. Several X-ray reflections were measured with a crystal plate in Laue geometry (shown in figure 1). The reflections 020 and 040 measured in the Bragg geometry are not shown, because they are so strong that they cannot displayed with the other ones together on same scale. The shape of each Bragg reflection was measured by ω- and ω-2θ-scans. The ω-scan is a rotation of the crystal by $\Delta\theta$, while the detector is fixed at 2θ and the ω-2θ-scan is a rotation of the crystal by $\Delta\theta$ and simultaneously a movement of the detector by $2\Delta\theta$. From the FWHMs of ω- and ω-2θ-scans of X-ray reflections measured very precisely one can determine the size and the misorientation of the mosaic blocks and also the lattice strain [3]. With these parameters one can experimentally derive the validity of approaches made by certain extinction theories [1, 2] extinction correction. Until now our measurements had been performed at the high resolution four circle diffractometer (Seifert XRD 3003 PTS-HR, $\lambda_{K_\alpha} = 1.541$Å) at the Universität Siegen, but it is planned to measure at BL10 at Delta. So a part of my work consists in building up the beamline BL10.

It is planned to compare the measured diffraction intensities from a plate with those of a sphere and to develop a better model for extinction effects based on the properties of the mosaic structure of real macroscopic crystals. Our aim is the development of a model that is well applicable for the data treatment in case of electron density determination in crystals especially containing heavy atoms like $LiSeO_4 \cdot H_2O$ and BiB_3O_6.

We would like to thank the NRW-Forschungsschule 'Forschung mit Synchrotronstrahlung in den Nano- und Biowissenschaften' for financial support.

References

[1] P.J. Becker and P. Coppens, *Acta Cryst.*. **A30**, 129 (1974).
[2] P. Suortti, *Acta Cryst.*. **A38**, 642 (1982).
[3] S. Wagner, Bachlor thesis, Universität Siegen (2009)
[4] W.H. Zachariasen, *Acta Cryst.*. **23**, 558 (1967).

First photoelectron spectroscopy studies of N-doped TiO_2

Tobias Lühr[1,2,*], Frank Schönbohm [1,2], Katharina Skaja [1,2], Sven Döring [1,2], Ulf Berges[1,2] , C. Westphal[1,2]

[1] Fakultät Physik - Universität Dortmund, Otto-Hahn-Str.4, D 44221 Dortmund, Germany
[2] DELTA - Universität Dortmund, Maria-Goeppert-Mayer-Str. 2, D 44227 Dortmund, Germany
[*] corresponding author: t.luehr@gmx.de

Presently, there is considerable interest in the reactivity of titanium oxide surfaces and titanium oxide doped thin layers. Scientifically, these systems are interesting for the general understanding of oxide surfaces, and recently these systems are promising candidates for the application in photoelectrical cells.

In photochemical cells, light absorption occurs within a space charge region of a semi-conductor, and the photon energy must be larger than the band gap. This process generates electron-hole pairs, which are separated within the space-charge region. The charge is transported to the electrodes where usually water is dissociated. At the anode water molecules are oxidized by holes, whereas at the cathode the water molecules are reduced by electrons. These redox-processes are studied since several years [1]. In many cases titanium oxide is chosen as semiconductor since it offers advantages in technological applications. However, titanium oxide has a bandgap of E_{gap}=3.2 eV which is far too much for the dissociative process with visible light [2]. Therefore, a tailor-cut variation of the band gap is presently obtained by proper dopants within the semiconductor bulk material and also within the surface region. Doping the titanium oxide and adjusting the band gap is performed since ∼10 years now, and the detailed understanding of structure and stoichiometry at the surface is completely unclear. Present dopants are nitrogen and iron. Also, only little is known about the driving electronic forces during the dissociation. For rather low nitrogen concentrations it was speculated that electronic states are concentrated at nitrogen atoms with an increase of the band gap for the titanium oxide species rutile. However, experimental results showed a decrease of the band gap, and no localized electronic hole states at nitrogen atoms in the lattice [3].

In order to investigate the photo activity of titanium oxide in the region of visible light anastas and rutile were doped with nitrogen. The photoactivity of the cell is usually probed by applying tri-methyl acetate acid (TMA), or in its adsorbed state on the TiO_2-surface with tri-methyl acetate. If the band gap is lowered due to a successful doping then an absorbed photon creates an electron-hole pair. In the following, the hole dissociates TMA forming CO_2 at the surface, which is an indicator for the photo activity rate of the system.

In this project the titanium oxide species rutile is investigated in detail, since it was shown that rutile has a strong dependence of its photo activity on the N-doping content. Presently, it is unknown why the photo activity dependence is occurring at rutile only, and why a N-content of approx. 2% in rutile shuts down its photo activity completely.

Fig. 1(a) compares two photo emission spectra of N-doped rutile recorded with excitation from a conventional AlK_α x-ray source. At a polar angle of θ=60° a high surface sensitivity is gained and therefore surface specific components as the C 1s signal rise due to carbon contamination at the surface. The two survey spectra clearly reflect the chemical composition of the sample by two prominent signals of oxygen and titanium. Also, at a binding energy of E_{bin} ∼ 400 eV the N 1s signal rises due to 2% nitrogen content in the sample. Figure 1(b) displays a survey spectrum recorded with an excitation energy of hν=650 eV. Clearly, due to the high flux at beamline 11, charging occurs and all photoemission lines are shifted by ∼ 100 eV. During the measurements it turned out that the strength of peak shift depends on the position where the photon beam hits the sample. In the next beamtime it is planned to go out of focus with the experimental set-up in order to reduce the photon flux per area.

A central question on the titanium oxide system is whether the sample is of crystalline structure

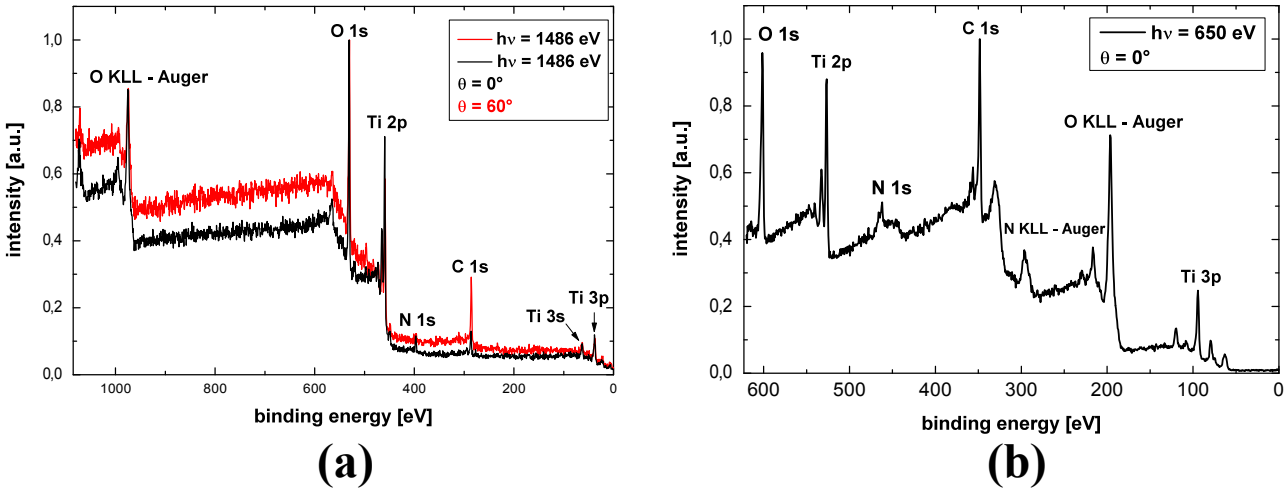

Figure 1: Survey scans (a) with an AlK_α x-ray source,(b) synchrotron light $h\nu = 650$ eV

within the surface area and at what sites the nitrogen atoms are located within the lattice. Therefore, a first photoelectron diffraction scan was recorded for grazing emission, in order to have a high surface sensitivity. Fig. 2 shows the photoelectron intensity as a function of azimuth angle, recorded at a polar angle of θ=70° with excitation from a conventional AlK_α x-ray source. Clearly, a very strong diffraction signature of around 40% is displayed. Therefore, the rutile crystal of titanium oxide has a crystalline structure within the surface region. In the next step, it is planned to record the diffraction features of the nitrogen signal with synchrotron radiation.

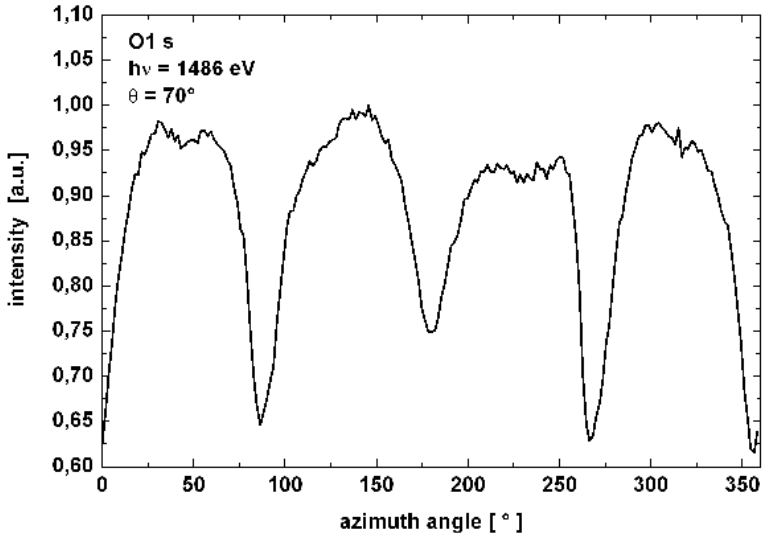

Figure 2: Azimuth scan of the O 1s signal at a polar angle of $\theta = 70°$

[1] M. Grätzel, Nature **414**, 338 (2001).

[2] R. Asahi, T. Morikawa, T. Ohwaki, K. Aoki, Y. Taga, Science **293**, 269 (2001).

[3] T. Ohsawa, I. Lyobinetsky, Y. Du, M.A. Henderson, V. Shutthanandan, S.A. Chambers, Phys. Rev. B **79**, 085401 (2009).

High-resolution XPS analysis of InAs quantum dots on GaAs(100)

M. W. Bruker[1,2,*], S. Döring[1,2], F. Schönbohm[1,2], D. Weier[1,2], U. Berges[1,2], A. Ludwig[3], A. D. Wieck[3], C. Westphal[1,2]

[1] Experimentelle Physik I - Technische Universität Dortmund, Otto-Hahn-Str. 4, D 44221 Dortmund
[2] DELTA - Technische Universität Dortmund, Maria-Goeppert-Mayer-Str. 2, D 44227 Dortmund
[3] Angewandte Festkörperphysik - Ruhr-Universität Bochum, Universitätsstr. 150, D 44780 Bochum
[*] corresponding author: max.bruker@tu-dortmund.de

In our experiments we analyzed a self-assembled InAs quantum dot system on a GaAs(100) substrate by means of X-ray photoelectron spectroscopy (XPS). Due to their geometry spatially constraining the wave functions of conductance electrons, quantum dots exhibit an electron density of states (DOS) different from that of bulk material. The electronic states of these systems are similar to those of a single atom, though by varying the size, a wide spectrum of binding energies (and thus, light absorption/emission lines) can be obtained. This makes quantum dots usable for a wide range of applications, ranging from LEDs to spintronics [1].

It has been reported that self-assembled quantum dots have a surface reconstruction accessible via XPS, though an exact spectral decomposition has not been found yet [2]. Using the XPS method, we have access to the electron core level DOS near the sample surface. Chemical shifts can be resolved, allowing for an investigation of the crystalline structure of the surface.

The samples were prepared using molecular beam epitaxy (MBE) at the Lehrstuhl für Angewandte Festkörperphysik, Ruhr-Universität Bochum. They were exposed to air during transportation, which demanded an in-situ fabrication of a protective coating, consisting of amorphous As. Thermal desorption of this coating in the XPS chamber was necessary in order to be able to observe the quantum dots directly at the sample surface, where the XPS method is very powerful.

The experiments were carried out at BL 11 at DELTA, using soft x-rays with an energy of 650 eV for survey scans and 90 eV for high-resolution core-level spectroscopy. A scan of the unmodified sample shows an As surface contaminated with O, C and S (Fig. 1).

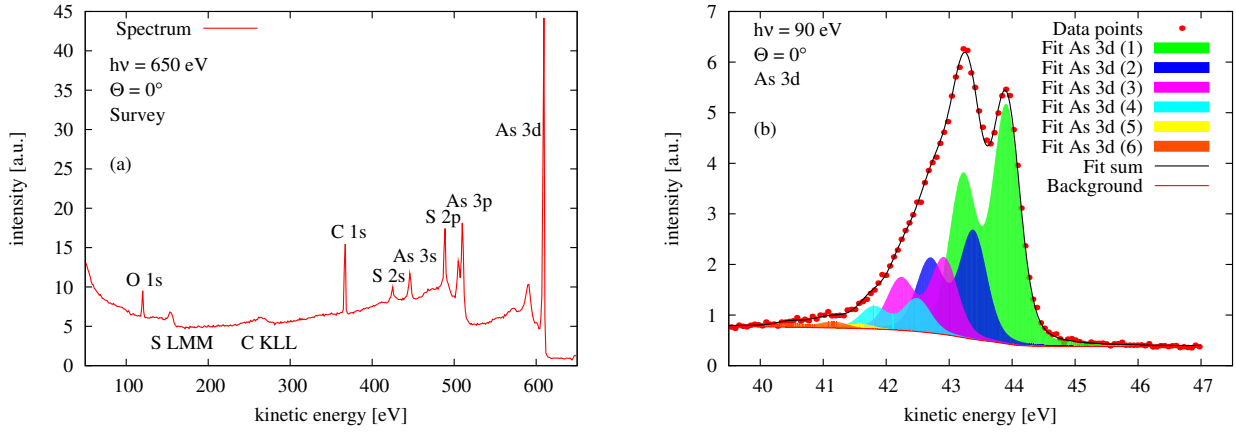

Figure 1: Spectra of the unmodified sample.
Survey scan (a), high-resolution scan of the As 3d peak (b).

Through analysis of an MBE-grown GaAs(100) sample, the preparation parameters for sample heating necessary for thermal desorption of the protective coating were carefully optimized. Applying these parameters, the QD samples were successfully decapped, yielding high-resolution As 3d, Ga 3d and In 4d core level spectra (Fig. 2).

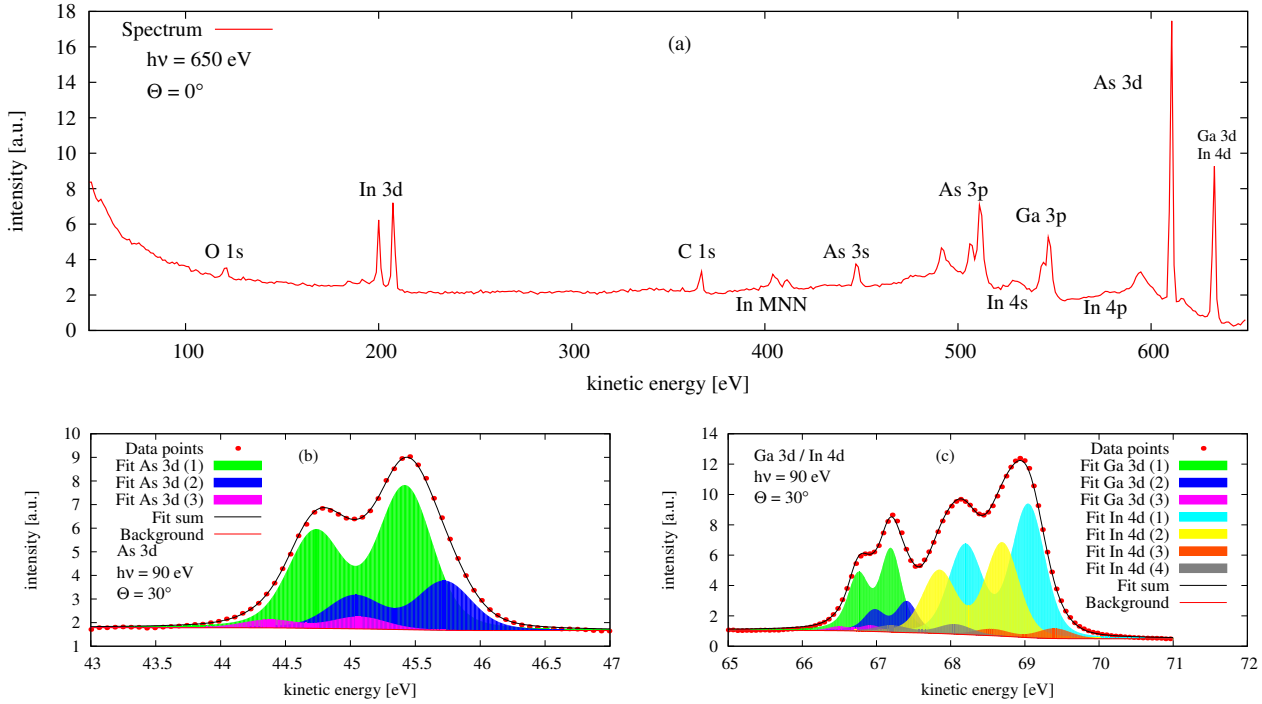

Figure 2: Spectra of the decapped QD sample.
Survey scan (a), high-resolution scans of As 3d (b) and Ga 3d / In 4d (c).

With an angle-resolved measurement, a decomposition of the spectra became possible. The In 4d peak exhibits four components belonging to the surface of the quantum dots and the wetting layer. A comparison of the GaAs sample and the QD sample with regard to their respective Ga 3d and As 3d components shows that fabrication of quantum dots using MBE changes the GaAs surface reconstruction underneath. Using the XPS data alone, a unique structural model for this could not be deduced. Therefore, we hope to clarify the structure in an extended investigation including photoelectron diffraction effects. In that future study, the results of the careful decomposition will serve as a starting point.

We would like to thank the DELTA machine group for providing synchrotron radiation and technical support. Furthermore, we thank the Lehrstuhl für Angewandte Festkörperphysik, Ruhr-Universität Bochum, for supplying the samples.

References

[1] M. A. Kastner, Artificial atoms, Phys. Today **46** (1), 24 (1993).

[2] C. McGinley et al., Evidence for surface reconstruction on InAs nanocrystals, Phys. Rev. B **65** (24), 245308 (2002).

PEEM at the TGM Beamline (BL 12) at DELTA: adaptation, modification, and first images

C. Keutner[1,2,*], U. Berges[1,2], C. Westphal[1,2]

[1] Experimentelle Physik I - Technische Universität Dortmund, Otto-Hahn-Str.4, D 44221 Dortmund
[2] DELTA - Technische Universität Dortmund, Maria-Goeppert-Mayer-Str. 2, D 44221 Dortmund
[*] corresponding author: christoph.keutner@tu-dortmund.de

(October 2010)

The first successful photoemission electron microscope (PEEM) images were recorded at BL 11 in the year 2009. Future PEEM experiments are planed at BL 12, since this beamline provides a photon energy of 5 to 200 eV with an overlap to laboratory photon sources. Thus, preparative work can be performed with conventional light sources followed by excitation with tunable synchrotron radiation. A further advantage of operating the PEEM at BL 12 is the possible future option of using circularly polarized light at this beamline. In the future, X-ray magnetic linear dichroism (XMLD) and also X-ray magnetic circular dichroism (XMCD) experiments are foreseen. Therefore it was necessary to adapt the PEEM set-up to BL 12.

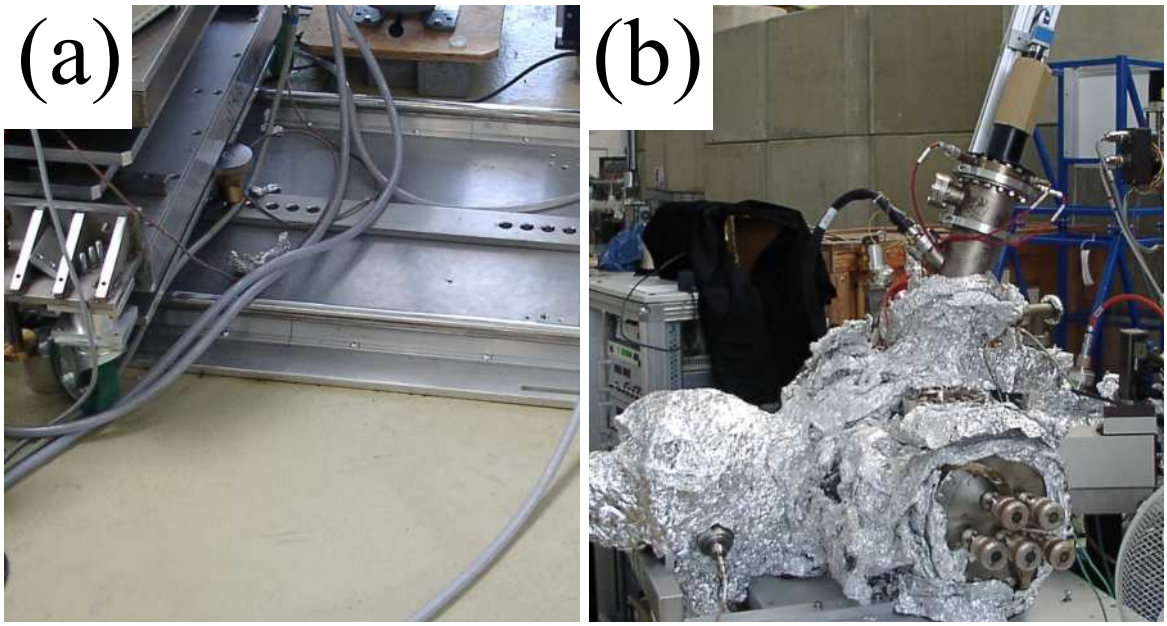

Figure 1: (a) The rail-system allowing a precise and reproducible mounting of the experiment. (b) CCD camera without cover box.

For mounting the PEEM at BL 12 it was necessary to add a carriage/railsystem to the PEEM set-up, as displayed in Figure 1. The carriage/rail-system allows an easy and reproducible change of endstations at the beamline. The carriage/railsystem consists of two rails on a massive metal plate and a carriage driving on them. A reproducible setting of the downstream position of the PEEM set-up is provided by a pin- and hole-mechanism as shown in Figure 1(a). A precise fine-tuning of the position of the chamber along the beam as well as transversal to the beam is provided by additional rack-wheels along the according directions. This feature enables also out-of-focus experiments, where the endstation chamber is moved under vacuum along the beam direction over a distance of about 600 mm.

The supportive frame of the PEEM chamber had to be adjusted to the beam-height at BL 12, which is 1067 mm above the DELTA-floor. With the new frame the PEEM can be

mounted on either the railsystem at BL 12 or on the identical system at BL 11.

During the first test experiments at BL 11 in the year 2009 it turned out that several components of the set-up needed to be replaced as soon as possible. Therefore, during the new mounting of the PEEM experiment at BL 12, the ion-pump and the turbo-molecular-pump were replaced. Also a residual gas analyser was added to the chamber in order to find small leaks and to improve the base pressure. Presently, a new CCD camera holder is under construction.

Parallel to the work on the mechanical parts of the experimental set-up first experiments with the Hg discharge lamp were performed. The major aim was to test the set-up and to check the mechanics of the fine adjustment of the sample manipulator. Figure 2 shows first PEEM images recorded with light-excitation from the Hg-lamp. At the time of recording it was not possible to move the sample-holder in order to select smaller test structures. However, the sharp contrast at the edges of the test structures indicates a possible higher spatial resolution. Presently, it is not possible to record PEEM images with synchrotron radiation because of deformations at the outlet-chamber in the beamline. In the coming winter shutdown of DELTA the replacement of the damaged outlet-chamber is scheduled which will bring BL 12 back to operation.

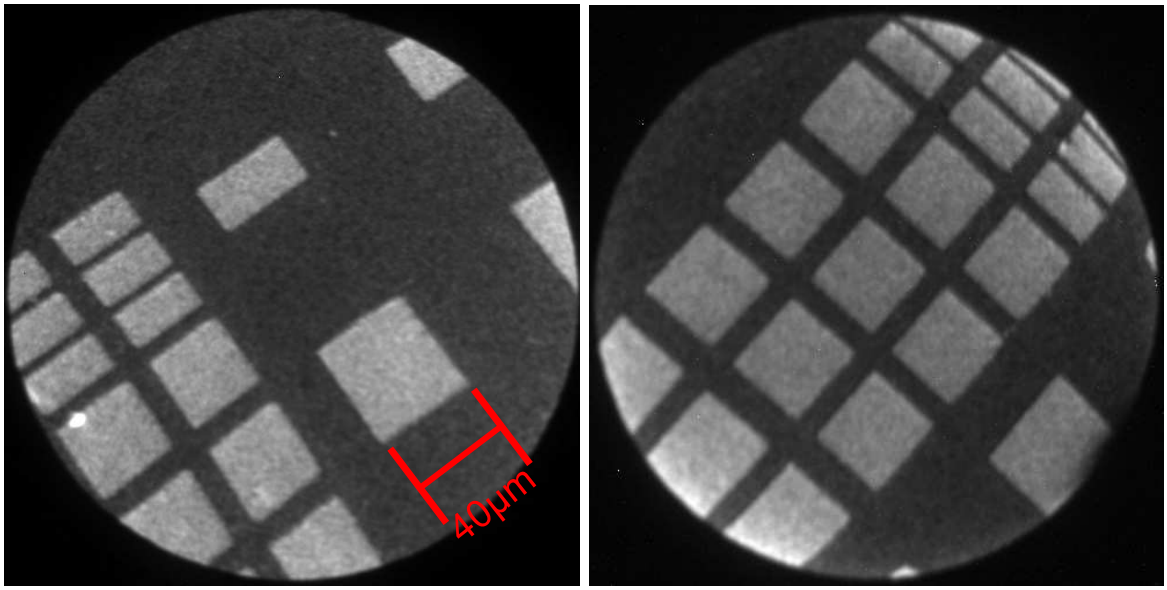

Figure 2: PEEM images of test structures recorded with the Hg discharge lamp at beamline 12. The image on the left shows a 20 µm x 40 µm rectangle and a 40 µm x 40 µm square in the center and the image on the right shows squares of 30 µm x 30 µm.

Acknowledgement

We would like to thank the DELTA-staff for their support.

Photoelectron spectroscopy (XPS) studies on the system titanium oxide on Si(100)

F. Schönbohm[1,2,*], D. Weier[1,2], U. Berges[1,2] C. Westphal[1,2]

[1] Experimentelle Physik 1 - TU Dortmund, Otto-Hahn-Str. 4, D 44221 Dortmund, Germany
[2] DELTA - TU Dortmund, Maria-Goeppert-Mayer-Str. 2, D 44227 Dortmund, Germany
[*] corresponding author: frank.schoenbohm@tu-dortmund.de

(October 2010)

In order to increase the energy efficiency which is reduced by tunneling leakage currents in semiconductor devices, the insulating SiO_2 layer has to be replaced. A thicker gate dielectric is necessary for a sufficient reduction of these leak currents but a thicker gate dielectric results in an decrease of the gate capacity. Therefore a successor of SiO_2 must have a significant higher dielectric constant k which compensates the loss in gate capacity for thick gate electrodes. As the dielectric constant of the replacement materials is higher than that of SiO_2, they are referred to as high-k materials. Presently, metal oxides as HfO_2, ZrO_2, and TiO_2 are discussed as the most promising candidates as possible substitutes for SiO_2. Titanium dioxide crystallizes in three crystal structures: rutile, anatase, and brookite. The formation of the crystal structures is temperature dependent. At a temperature of about 350°C to 400°C, anatase is formed, and in the range of 800°C to 1100°C, anatase is transformed to rutile [1]. It is known that TiO_2 shows an increasing dielectric constant with increasing amount of TiO_2 in the rutile phase [2]. Titanium dioxide is widely used as white pigment in wall paint and as anti-reflective coating for optical devices. Furthermore, TiO_2 is used for surface passivation, for catalysis, for oxygen sensors in lambda probes, and for solar cells. Since titanium dioxide is widely applied in many technical applications, we studied the structure of thin TiO_2 films on Si(100) and especially their thermal stability.

All measurements were performed at beamline 11 at DELTA. Substrate cleaning and TiO_2 film growth were performed in-situ in the ultra-high vacuum chamber at a base pressure of about $5 \cdot 10^{-11}$ mbar. After cleaning of the sample by annealing at 1050°C, a thin film of TiO_2 was grown on the clean Si(100) surface, prepared by electron beam evaporation. In order to investigate the thermal stability of the TiO_2 film, the sample was annealed stepwise to higher temperature, and XPS spectra of TiO_2 were taken after each annealing step as presented in Fig. 1. At 515°C, a new spectral component arises in the spectra, which is displayed at $E_{kin} \approx 65.6$ eV kinetic energy. However, both components are removed from the sample after an annealing step at 770°C. In order to determine the Si structure beneath the TiO_2, an XPD pattern was recorded of the Si signal (Fig. 2). A detailed analysis of the pattern and the structure analysis within a numerical calculation is still in progress.

[1] P. R. McCurdy, L. J. Sturgess, S. Kohli, and E. R. Fisher, Appl. Surf. Sci. 233, 69–79 (2004)

[2] Jin Young Kim, Dong-Wan Kim, Hyun Suk Jung and Kug Sun Hong, Jpn. J. Appl. Phys. 44, 6148–6151 (2005)

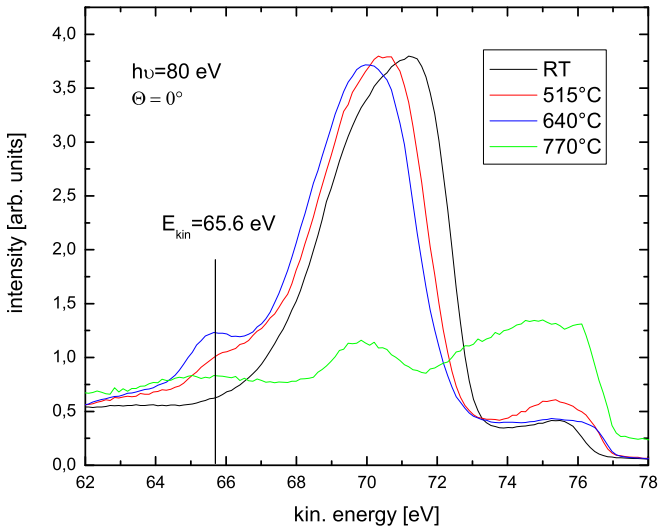

Figure 1: TiO_2 spectra after annealing at different temperatures. After annealing at 515°C, a new spectral component arises in the spectra, which is displayed at $E_{kin} \approx 65.6$ eV kinetic energy. The new component vanishes after an annealing at 770°C.

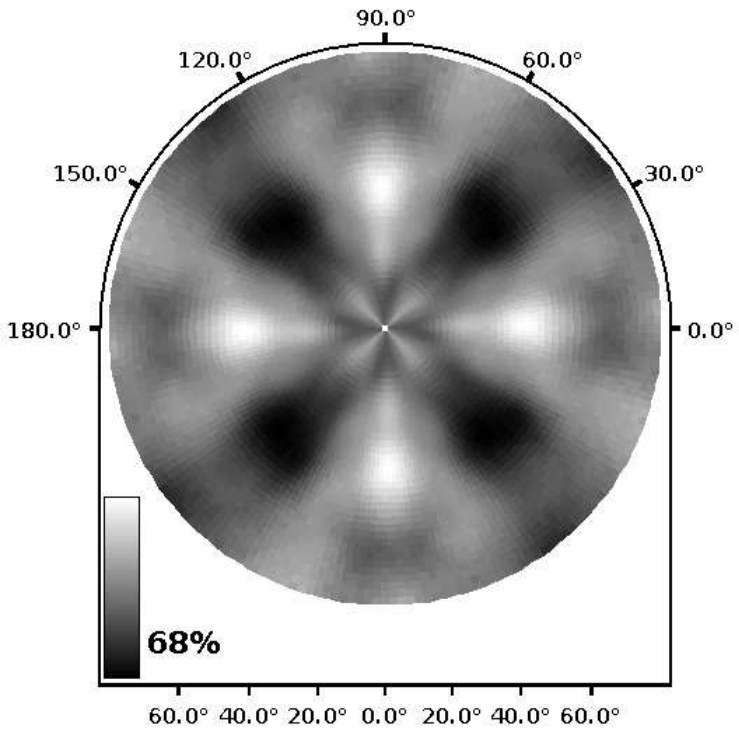

Figure 2: XPD pattern of the Si 2p intensity recorded at $E_{kin} \approx 57.5$ eV kinetic energy recorded after annealing at 915°C. A detailed structure determination of the sample surface is still in progress.

Chemical properties of the magnetic oxide $NiFe_2O_4$ on $SrTiO_2$

M. Müller[1], C. Caspers[1], S. Döring[2], U. Berges[2], C. Westphal[2], and C. M. Schneider[1]

[1]Institut für Festkörperforschung (IFF-9), Forschungszentrum Jülich, 52428 Jülich

[2]Experimentelle Physik 1, Technische Universität Dortmund

A main issue in the field of spin electronics is the generation, manipulation and detection of spin-polarized electron currents. An interesting approach to realize this goal is the filtering of electron spins in a magnetic tunnel barrier, i.e. a thin magnetic insulating film. Spinel ferrites with the formula $(Ni,Co)Fe_2O_4$ show a Curie temperature above room temperature, an insulating behavior and a large magnetic exchange splitting. In order to integrate them as spin filter tunnel barriers, however, the crystal and interfacial quality of a $(Ni,Co)Fe_2O_4$-based heterostructure must be very good. In particular, the magnetic and structural properties show a large relationship. Both a reduced dimensionality as well as structural disorder of the spinel lattice are expected to strongly influence the spin filter properties of $(Ni,Co)Fe_2O_4$.
In our work, we focused on the chemical and structural properties of 20nm thick $NiFe_2O_4$ films grown in $SrTiO_2$ substrates by means of Pulsed Laser Deposition (PLD). We conducted soft x-ray spectroscopy measurements at Beamline 11 in order to study the chemical state and stoichiometry of the $NiFe_2O_4$ spinel film. XPS is a useful tool to study the lattice site occupancy of the Fe^{2+}/Ni^{2+} cations. since the occupancy of tetrahedral and octahedral sites gives a detectable contribution of spectral weight. By fitting the respective core-levels of Ni 2p/3p and Fe 2p, we obtain a negligible amount of site disorder (tetrahedral, octahedral) and a good match of $NiFe_2O_4$ stoichiometry. This result is consistent with our magnetic and structural analysis of the films, as well as with the PLD preparation condictions.

Investigation of the the thermal stability of $HfO_2/Si_3N_4/Si$

K. Skaja[1,2,*], D. Weier[1,2], F. Schönbohm[1,2] , C. Westphal[1,2]

[1] Fakultät Physik - Universität Dortmund, Otto-Hahn-Str.4, D 44221 Dortmund, Germany
[2] DELTA - Universität Dortmund, Maria-Goeppert-Mayer-Str. 2, D 44227 Dortmund, Germany
[*] corresponding author: katharina.skaja@uni-dortmund.de

The development of new *high-k* gate dielectrics for future complementary metal-oxide semiconductor CMOS devices is crucial for achieving low leakage currents and small equivalent oxide thicknesses EOT [1]. The dielectric constant of HfO_2 is high, around 25 [1], but HfO_2 films grown on Si are thermally not stable. HfO/Si_xN_y films produced by incorporating nitrogen are thermally stable and have amorphous structures at high temperatures. Their dielectric constant is sensitive to the nitrogen concentration and varies from 14 to 24; the nitriding process can create conductive states caused by metallic Hf-N bonds. At present, all the features of these films prevent their application in device fabrication. One way to avoid silicide formation in the HfO_2 / Si system is growing HfO_2 on a buffer layer which is seperating the HfO_2 film from the Si bulk. For this task, the buffer layer should be amorphous, as thin as possible, uniform, and thermally stable. Si surfaces thermally nitrided in NH_3 atmosphere generate a Si_3N_4 buffer layer, however, the buffer layer also contains impurities such as hydrogen and oxygen. On Si(111) surfaces, periodically reconstructed silicon nitride buffer layers prepared in this manner were reported [2], whereas on Si(100) uniform silicon nitride layers were formed only for special processing parameters [2].

In this work an alternative preparation method for the nitride buffer layer was chosen. The ultrathin Si_3N_4 films were grown on atomically clean Si(2x1)-reconstructed surfaces where nitrogen plasma was provided from a special plasma source. The plasma source was mounted normal to the Si-surface, and the nitrogen plasma consisted of nitrogen ions. With this procedure it was possible to prepare Si_3N_4 buffer layers with different film thicknesses obtained for different plasma source operational parameters. In this study we will show data from an approx. 2.9 Å thick film. On top of the buffer layer HfO_2 was evaporated. The evaporation procedure was performed by using an electron beam evaporator. The film thickness of the HfO_2 layer was estimated to be 5 Å by comparing the intensity ratio of the Si 2p and Hf 4f signal within an ARXPS measurement.

Fig. 1 (a) shows survey spectra of the sample before and after the preparation procedure. It is clearly visible that the sample contains oxygen, nitrogen, and hafnium signals in addition to the silicon signals displayed in the spectrum of the clean sample. In Fig. 1 (b) a high resolution scan of the Si 2p signal before and after the first preparation step is shown. The large additional component at a kinetic energy of $E_{kin} \approx 73$ eV can be clearly attributed to the Si_3N_4 layer due to the chemical shift relative to the Si 2p bulk signal. The complete annihilation of the Si dimer components after adsorption indicates a closed Si_3N_4 layer at the surface. These spectroscopic findings were also checked by LEED, and the missing (2x1) reconstruction in the LEED pattern confirms the structural change at the Si-surface due to nitration.

In the next step the Si_3N_4 surface is considered as the substrate for HfO_2 evaporation and the following annealing procedure. Fig. 2 shows high resolution spectra of the Hf 4f signal, all recorded after evaporation and some subsequent annealing steps. Within the annealing procedure the sample was flash heated for 1 min. at different temperatures.

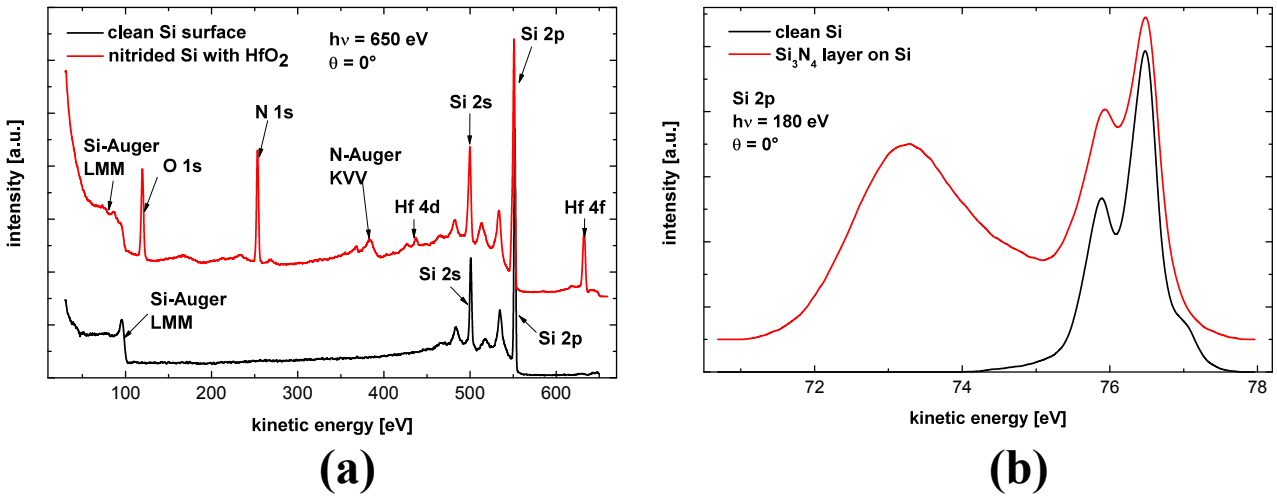

Figure 1: Survey scan before and after the preparation (a), and high resolution scan of the Si 2p signal(b)

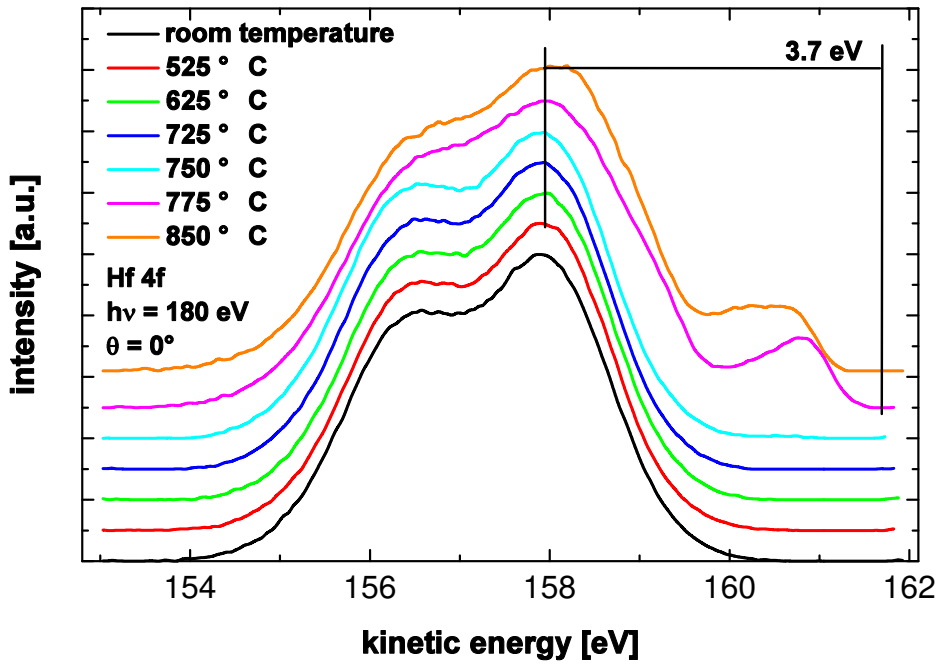

Figure 2: High resolution spectra of the Hf 4f signal directly after the evaporation and the following annealing steps.

In Fig. 2, the Hf 4f signal remains unchanged up to annealing temperatures of 750 °C which indicates a stable HfO_2 layer up to these temperatures. At higher temperatures an additional component at higher kinetic energies arrises. Thus, additionally to HfO_2, further bonds are formed which lead to a spectral signal at $E_{kin} \approx 161$ eV. For unbuffered HfO_2/Si

systems the transformation from HfO_2 to HfSi is well known [3,4]. In technological applications, HfSi formation is not wanted because of its conductive features which suppress the capacitive properties of the system. However, the chemical shift of the observed new component at E_{kin} $\approx$ 161 eV is much too low for being interpreted as a signal of HfSi. The chemical shift of a hafniumsilicide signal was reported to be approx. 3.7 eV to higher kinetic energies. In our analysis the component is shifted by approx. 2.9 eV only. Therefore, this component could be identified as a signal of $Hf_{x_1}Si_{x_2}O_{x_3}N_{x_4}$ instead of HfSi. $Hf_{x_1}Si_{x_2}O_{x_3}N_{x_4}$ provides capacitive properties as needed for new *high k* dielectrics in future metal-oxide semiconductor CMOS devices.

Fig. 2 shows that this component remains stable up to a temperature of 850 °C, which is a usual temperature during the present production process of complementary metal-oxide semiconductor CMOS devices [1]. Therefore, we could show that the buffer layer strongly increases the thermal stability of the system and this allows to reach sufficient temperatures.

In summary we successfully prepared well ordered and completely closed Si_3N_4 on silicon using a plasma source. Onto these buffer films HfO_2 was evaporated and the thermal stability of HfO_2 was increased to temperatures up to 850 °C. In future studies we will vary the film thickness of the Si_3N_4 film in order to find the minimal thickness which is necessary to increase the thermal stability of HfO_2 and we will investigate the stability of the $Hf_{x_1}Si_{x_2}O_{x_3}N_{x_4}$ component up to 1000 °C. Thus, the introduction of a $Hf_{x_1}Si_{x_2}O_{x_3}N_{x_4}$ buffer layer could be a successful candidate as a successor of the presently used SiO_2 films.

Aknowledgments

We thank the staff of DELTA for the support during beamtimes.

[1] G.D. Wilk, R.M. Wallace, and J.M. Anthony, J. Appl. Phys. **89**, 5243 (2001).

[2] X. Wang, G. Zhai, J. Yang, and N. Cue, Phys Rev. B **60**, R2146 (1999)

[3] C.R. Flüchter, A. de Siervo, D. Weier, M. Schürmann, A. Beimborn, S.Dreiner, M.F. Carazzolle, R. Landers, G.G. Kleiman, and C. Westphal, Surf. Sci. **602**, 3647 (2008).

[4] A. de Siervo, C.R. Flüchter, D. Weier, M. Schürmann, S. Dreiner, C.Westphal, M.F. Carazzolle, A. Pancotti, R. Landers, and G.G. Kleiman, Phys. Rev. B **74**, 075319 (2006).

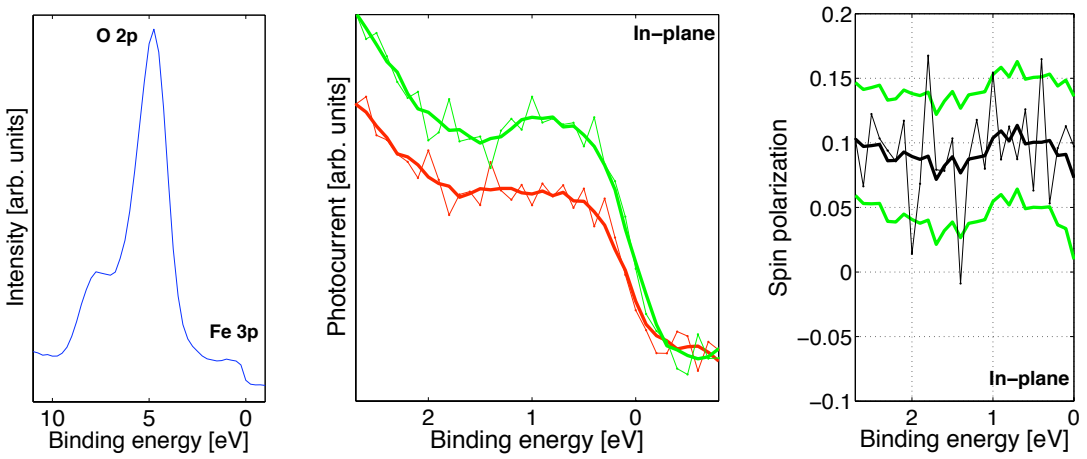

Figure 0.1: Data taken on 2 ML MgO/Fe/GaAs(001) at a photon energy of 64 eV, and an emission angle of 21°. (a) Spin-integrated photoemission spectrum (taken by the delay-line detector) (b) Spin-resolved photoemission spectra (taken by SPLEED detector), green line: majority spin, red line: minority spin. There is no sharp minority feature at the Fermi edge which could be referred to the predicted interface state. (c) Spin-polarization distribution: blue line; standard deviation: green lines

Spin- and angle-resolved PES on Fe/GaAs(001) and MgO/Fe/GaAs(001) epitaxial system

The electronic properties of Fe/GaAs(001) and MgO/Fe/GaAs(001) have been investigated at our beamline in the context of a Diploma thesis by Daniel Gottlob. The analysis is based on data obtained by spin-polarized photoemission at a photon energy of 64 eV on samples kept at room temperature. The electronic structure was probed in two different regions of the Brillouin zone (all results are referred to the Brillouin zone of bulk Fe), which have been chosen for reference (normal emission, Γ point) and the expectation of a surface state (21°) that has been seen on Fe/W(001) in a previous study [1]. This surface state is expected to turn into an interface state when the MgO capping is applied [2, 3]. The samples were prepared *in situ* by Ar^+ sputtering, annealing and molecular beam epitaxy. GaAs cleanliness and 4x6 surface reconstruction were confirmed by LEED and AES, which were also used to confirm the cleanliness of the Fe and MgO films and calibrate the deposition rates of the respective e-beam evaporators.
The reference measurements showed behavior known from previous studies (features at the same binding energies, spin polarization of 50% with a positive sign) [4, 5, 6]. The data taken from Fe/GaAs(001) (emission angle 21°) showed hints of the predicted surface state, while the measurements of MgO/Fe/GaAs(001) (emission angle 21°) showed no minority feature at the Fermi edge at all (see Fig. 0.1). This leads us to the conclusion that either the interface state does not form or As segregation prevents it. Measurements on samples cooled down to cryogenic temperatures might be mandatory since it was involved in the studies on Fe/W(001) [1]. To clarify the properties of the interface of MgO/Fe further research is needed.

Bibliography

[1] L. Plucinski, Y. Zhao, C. Schneider, B. Sinkovic, and E. Vescovo, *Surface electronic structure of ferromagnetic Fe(001)*, Physical Review B **80**, 184430 (2009).

[2] W. H. Butler, X.-G. Zhang, T. C. Schulthess, and J. MacLaren, *Spin-dependent tunneling conductance of Fe/MgO/Fe sandwiches*, Physical Review B **63** (2001).

[3] K. D. Belashchenko, J. Velev, and E. Y. Tsymbal, *Effect of interface states on spin-dependent tunneling in Fe/MgO/Fe tunnel junctions*, Physical Review B **72** (2005).

[4] F. Matthes, L.-N. Tong, and C. Schneider, *Spin-polarized photoemission spectroscopy of the MgO/Fe interface on GaAs(100)*, Journal of applied physics **95**, 7040 (2004).

[5] M. Müller, *Electronic Structure of Ferromagnet-Insulator Interfaces: Fe/MgO and Co/MgO*, Doktorarbeit, 2007.

[6] L. Plucinski, Y. Zhao, and B. Sinkovic, *MgO/Fe(100) interface: A study of the electronic structure*, Physical Review B **75**, 214411 (2007).